MULTISCALE MECHANICAL CHARACTERIZATION OF SOFT MATTER

NICHOLAS AGUNG KURNIAWAN

NATIONAL UNIVERSITY OF SINGAPORE

2011

MULTISCALE MECHANICAL CHARACTERIZATION OF SOFT MATTER

NICHOLAS AGUNG KURNIAWAN

(*B.Eng*.(*Hons*.), NUS)

A THESIS SUBMITTED

FOR THE DEGREE OF DOCTOR OF PHILOSOPHY

NATIONAL UNIVERSITY OF SINGAPORE

2011

Acknowledgments

The work presented in this thesis is the result of a number of collaborations. It has been an inspiring and wonderful experience to work with these lively scientists.

My first word of thanks must go to my supervisor, Prof. Raj Rajagopalan. The influence of his mentoring over my graduate course cannot be overstated. I admire his openness to letting students take responsibility for seeing their ideas through and his willingness to constantly create opportunities for his students. His enthusiasm, clarity of thought, tireless work ethic, and integrity serve as a constant reminder of what it takes to be a great scientist.

I am deeply indebted to my co-supervisor, Prof. Lim Chwee Teck, who helped shape the course of my project in the early stages of my research. His passion for interdisciplinary and collaborative research has positively infected how I think and approach science. I am equally grateful to my committee members, Prof. Yan Jie and Prof. Sow Chorng Haur, for their time and consideration. Their inputs and support have helped me through the important milestones of this work. I would also like to thank other scientists that have helped my project in one way or another, especially Prof. Too Heng-Phon and Prof. Johan van der Maarel for the fruitful discussions.

I feel fortunate to have worked closely with Sun Wei in the first stage of my work. Having mechanical engineering background like I do, she understood my early difficulties with cell cultures, biochemical protocols, and assays, and her patient guidance definitely made my path easier. Besides her knack for detailed intellectual discussions, her relentless fervor has been instrumental in my development as a researcher. The simulation work in this thesis is only possible through the help of Søren Enemark. Søren is highly skilled in algorithms and molecular dynamics simulations, and is a prolific yet practical thinker. His ability to methodically dissect the physics behind simulations has helped bring results into focus. More recently, I have had the pleasure to work with Kat Wong on the biological perspectives and applications of this work. Her youthful energy and exuberance, not to mention her flair to visually beautify things, made her really fun to work with. It was a real joy being around these people.

I am also thankful to the other members and former members of Prof. Raj's research group (Vigneshwar Ramakrishnan, Srivatsan Jagannathan, Li Jianguo, Dhawal Shah, Harve Karthik, Sivashankari Gnanasambandam, Reno Antony, Manju Garg, and Adam Bin Idu Jion) and Prof. Lim's lab (Tan Swee Jin, William Chung, Li Qingsen, Earnest Mendoz, Yuan Jian, Vedula Sri Ram Krishna, Li Ang, Lim Tong Seng, and many others) for creating not only an intellectually stimulating and research-conducive environment, but also a supportive and friendly atmosphere.

I would like to acknowledge NUS Graduate School for Integrative Sciences and Engineering (NGS) and the Global Enterprise for Micro-Mechanics and Molecular Medicine (GEM^4) for the financial support of my graduate education. In addition, my research efforts have been greatly aided by administrative and logistical supports from the NGS office (Irene Chuan, Rahayu Aziz, Vivien Li, Ivy Wee, and Neo Cheng Bee), ChBE office (Alyssa Tay and Ang Wee Siong), NanoBiomechanics lab (Hairul Nizam), and rheology lab (Jamie Siew).

Last, I would like to express my greatest gratitude to my family, especially my mother, Ratna Susanti, and my fiancé, I Fon Bambang, for their endless support and love throughout these years.

Publications

Published works:

Kurniawan, N. A., Lim, C. T, and Rajagopalan, R. (2010). Image correlation spectroscopy as a tool for microrheology of soft materials. Soft Matter, 6(15), 3499-3505.

Kurniawan, N. A. and Rajagopalan, R. (2011). Probe-independent image correlation spectroscopy. Langmuir 27(6), 2775-2782.

Submitted manuscript:

Kurniawan, N. A., Enemark, S., and Rajagopalan, R. The role of structure in the nonlinear mechanics of semiflexible polymer networks. (submitted)

Kurniawan, N. A., Wong, L. H, and Rajagopalan, R. Early stiffening and softening of collagen: interplay of deformation mechanisms in biopolymer networks. (submitted)

Manuscripts in preparation:

Kurniawan, N. A., Wong, L. H., Sun, W., Lim, C. T., Too, H.-P., and Rajagopalan, R. Strain-dependent viscoelasticity of collagen networks. (in preparation)

Table of Contents

Acknowledgments .... **i**

Publications .... **iv**

Table of Contents .... **v**

Summary .... **x**

List of Tables .... **xii**

List of Figures .... **xiii**

List of Symbols .... **xvi**

Chapter 1 : Introduction **1**

- 1.1 Soft matter 1
- 1.2 Scale-dependent mechanics of soft matter 3
- 1.3 Characterization techniques of soft matter 5
  - 1.3.1 Microscopy 5
  - 1.3.2 Rheology 7
  - 1.3.3 Scattering and spectroscopy techniques 9
  - 1.3.4 Computer simulations 10
- 1.4 Scope and Structure of the Thesis 11

Chapter 2 : Macromechanics of Collagen Networks **13**

- 2.1 Introduction 13
  - 2.1.1 Collagen 13

2.1.2 Bulk characterization of collagen networks 14

2.2 Materials and Methods 16

2.2.1 Collagen hydrogel preparation 16

2.2.2 Confocal reflection microscopy 17

2.2.3 Mechanical rheology 18

2.3 Results and Discussion 18

2.3.1 Collagen network microstructure 18

2.3.2 Rheology of collagen networks 21

2.3.3 Amplitude-dependent oscillatory shear measurement 26

2.3.4 Strain-dependent mechanics of collagen networks 31

2.3.5 Mechanics of collagen network rearrangements 37

2.4 Summary 42

Chapter 3 : Mechanics of Semiflexible Polymer Networks 43

3.1 Introduction 43

3.2 Methods 46

3.2.1 Network model 46

3.2.2 Network generation and deformation 49

3.3 Results and Discussion 51

3.3.1 Network structural parameters 52

3.3.2 Length-scale-dependent network mechanics at small strain 54

3.3.3 Nonlinear strain-dependent network mechanics 56

3.3.4 Network deformation mechanism 59

3.4 Conclusions 61

Chapter 4 : Microrheology of Collagen Networks 63

4.1 Introduction 63

4.2 Microrheology 64

4.3 Materials and Methods 68

4.3.1 Collagen hydrogel preparation with embedded beads 68

4.3.2 Imaging 69

4.3.3 Probe tracking 69

4.3.4 Extraction of microrheological information...71

4.4 Results and Discussion 71

4.4.1 Discrepancy with mechanical rheology results....................................71

4.4.2 Matrix heterogeneity 74

4.5 Discussion 78

Chapter 5 : Image Correlation Spectroscopy for Microrheology.........................81

5.1 Introduction 81

5.1.1 Problems with current microrheological techniques............................81

5.1.2 Image correlation spectroscopy..81

5.2 Materials and Methods 86

5.2.1 Sample preparation..86

5.2.2 Mechanical rheometry..87

5.2.3 Imaging 88

5.2.4 Data collection and analysis: ICS 88

5.2.5 Extraction of microrheological information: ICS-μR 90

5.3 Results 91

5.3.1 Extraction of MSD from image correlation data..................................92

5.3.2 ICS-μR for Newtonian fluids 96

5.3.3 ICS-μR for viscoelastic networks 98

5.4 Discussion 101

Chapter 6 : Probe-independent Image Correlation Spectroscopy 105

6.1 Introduction 105

6.2 Theory 106

6.2.1 Conventional ICS for point emitters 107

6.2.2 Probe-independent ICS 108

6.3 Materials and Methods 110

6.3.1 Computer simulations 110

6.3.2 Sample preparation and imaging..112

6.3.3 ICS analysis...113

6.4 Results 115

6.4.1 Probe-independent ICS on simulated images 115

6.4.2 Probe-independent ICS on confocal images 124

6.5 Discussion 127

Chapter 7 : Conclusions and Outlook 130

7.1 Summary 130

7.2 Future Directions...134

7.2.1 Characterization of evolving soft matter 134

7.2.2 The role of other structural variables on the mechanics of semiflexible polymer networks 135

7.2.3 Probe-material interaction 136

7.2.4 Probeless microrheology 138

Bibliography 141

Appendix A: Steps in ICS-µR 154

Summary

This thesis presents a phenomenological study of the mechanics of soft matter systems, particularly polymer networks. Due to the length- and time-scale dependence of the mechanical properties of these networks, it is necessary to utilize multiple characterization techniques. Using a combination of bulk mechanical rheology (MR), microscopy, particle tracking microrheology (PTM), image correlation spectroscopy (ICS), as well as numerical simulation, we investigate the interplay between the mechanics of polymer networks at different length and time scales.

In the first part of the thesis, we focus on studying the mechanics of collagen networks, a type of biopolymer network that significantly determines the mechanics of biological tissues. Collagen forms highly heterogeneous networks and exhibits strain-dependent mechanical behavior. We systematically dissect the roles of collagen concentration, fiber entanglement, and network connectivity in governing the mechanics at different length scales and strain levels. Based on the results obtained from MR, PTM, and computer simulations, we propose a deformation mechanism that can explain the full spectrum of collagen network mechanical response. Despite the valuable insights gained through the combination of techniques, this work underscores the importance of accounting for system heterogeneity and some of the limitations of existing mechanical characterization techniques.

In the second part of the thesis, we develop a novel microrheological technique based on ICS that we call ICS-μR. ICS is an emerging biophysical tool that allows quantitative measurements of the dynamics of imaged fluorescent molecules. We present a mathematical framework for extracting the microrheological information from the correlation data and further extend the capability of ICS to perform dynamic measurement in a probe-independent manner. We validate the method on both Newtonian and complex fluids (homogeneous polymer networks) with various viscoelastic properties. The potential of simultaneously obtaining spatiotemporal measurements and microrheological information from a single set of image data makes ICS-μR a prospective tool in many applications, biological or otherwise.

List of Tables

Table 1: List of independent variable parameters for simulating semiflexible polymer network model 49

List of Figures

Figure 2.1: Confocal reflection microscopy images of collagen networks. 19

Figure 2.2: Schematic of oscillatory rheology measurement..................................... 22

Figure 2.3: Typical stress-strain oscillatory response of viscoelastic material. 22

Figure 2.4: Frequency dependence of the shear moduli of collagen networks........... 24

Figure 2.5: The mechanics of collagen networks in response to oscillatory shear deformations. 25

Figure 2.6: Stress τ and shear moduli G' and $G"$ of collagen network under oscillatory shear with varying strain amplitude............................ 26

Figure 2.7: Lissajous plots generated from the stress-strain waveforms at different γ 27

Figure 2.8: Graphical description of the elasticity measures.................................... 29

Figure 2.9: Elastic moduli of collagen network as a function of strain amplitude γ_0. 30

Figure 2.10: Scaling of the nonlinearity parameters of collagen networks with collagen concentration c. 33

Figure 2.11: The influence of actin concentration c_A and cross-link density on the strain-stiffening behavior of cross-linked actin networks............. 36

Figure 2.12: Cyclic softening and reversibility of collagen networks. 38

Figure 2.13: Strain-dependent network stiffness is a transient phenomenon. 40

Figure 3.1: Strain stiffening properties of various biopolymer networks. 44

Figure 3.2: Summary of fiber model and interaction.. 48

Figure 3.3: Illustration of semiflexible polymer network model. 51

Figure 3.4: Typical overall response of cross-linked semiflexible polymer networks... 52

Figure 3.5: The relation of input δ_{cl} and Φ values to output R_{cl} of the network. 54

Figure 3.6: Influence of network structure on the network response at small strain. 55

Figure 3.7: Influence of network structure on the network response at intermediate and large strains. 58

Figure 3.8: Illustration of nonaffine deformation. 60

Figure 3.9: Quantification of network affinity and rearrangement at different

strain levels. 60

Figure 4.1: Workflow of particle tracking microrheology measurement.................... 68

Figure 4.2: Comparison between rheological and microrheological measurements of collagen networks for a concentration range of 1.5–3.5 mg/ml. 73

Figure 4.3: Typical distribution of probe MSD in a single sample of 1.5 mg/ml collagen network. 75

Figure 4.4: Typical distribution of the storage modulus $G'(\omega)$, as a function of frequency ω, for 1.5 mg/ml collagen network.................................. 76

Figure 4.5: Typical trajectories of probe particles in a single collagen network sample. 78

Figure 5.1: An overview of the various ICS techniques that have recently been developed for various purposes.. 83

Figure 5.2: Schematic illustration of the working principle of FCS and ICS............ 84

Figure 5.3: A schematic overview of ICS and its extension to microrheology, ICS-μR. 85

Figure 5.4: Illustration of the evolution of MSD with time...................................... 93

Figure 5.5: Illustration of the capability of our approach to reconstruct $\left\langle \Delta r^2(\tau) \right\rangle$ of reported experimental data.. 96

Figure 5.6: ICS-μR results for glycerol aqueous solutions with various concentrations. 98

Figure 5.7: MSD of 0.5 μm beads in PEO aqueous solutions with various concentrations obtained from ICS correlation functions. 99

Figure 5.8: Comparison between frequency-dependent linear viscoelastic moduli for PEO aqueous solutions of various concentrations as measured with ICS-μR and mechanical rheometer (MR). 101

Figure 6.1: Illustration of images generated by computer simulations for ICS with probes of different shapes and uniform fluorophore distribution within the probes. 117

Figure 6.2: The correlation functions $g(\tau)$ of images of different fluorescent bodies. 119

Figure 6.3: Typical normalized one-dimensional spatial correlation function $r(0,\eta,0)$ from simulated images of different geometries and sizes.. 120

Figure 6.4: Template analysis of images of different fluorescent bodies. 121

Figure 6.5: Comparison between standard analysis and template analysis

analyses for ICS. 123

Figure 6.6: Images of fluorescent microspheres of different sizes suspended in glycerol solutions and the corresponding templates used in ICS analysis. 125

Figure 6.7: Comparison between template and standard analyses for ICS measurements of the fluorescent images of microspheres with different diameters. 126

Figure A 1: A schematic overview of data analysis steps involved in ICS-μR. 154

Figure A 2: Comparison between the raw, unsmoothed $g(\tau)$ data obtained from Step B and the extracted $g(\tau)$ data obtained from Step E. 158

Figure A 3: Comparison between the $\left\langle \Delta r^2(\tau) \right\rangle$ data obtained from Step C and the extracted $\left\langle \Delta r^2(\tau) \right\rangle$ data obtained from Step E. 159

Figure A 4: Comparison between the 'raw' $G'(\omega)$ and $G''(\omega)$ data obtained from Steps C, D, and F and the extracted $G'(\omega)$ and $G''(\omega)$ data obtained from Steps E and F. 159

Figure A 5: Comparison between frequency-dependent linear viscoelastic moduli for PEO aqueous solutions of various concentrations as measured with ICS-μR and mechanical rheometer (MR). 160

List of Symbols

a	Radius of probe particles
α	Local power law exponent
α_0	Asymptotic local power law exponent in the short time limit
α_∞	Asymptotic local power law exponent in the long time limit
A	Nonaffinity parameter
A_f	Fiber cross-sectional area
c	Polymer concentration
$c*$	Overlap concentration
c_{cl}	Cross-link concentration
c_m	Monomer concentration
C	Fluorophore distribution
φ	Spatiotemporal correlation function of fluorophore distribution
γ	Shear strain
$\dot{\gamma}$	Strain rate
γ_0	Amplitude of sinusoidally varying shear strain
γ_c	Critical strain
γ_r	Rupture strain
Γ	Gamma function
χ	Transition rate between two asymptotic power law exponents
d	Fiber diameter
d_0	Experimental Gaussian width in standard analysis

d_f	Deconvoluted Gaussian width in template analysis
d_{xy}	Lateral cross-correlation radius
d_z	Axial cross-correlation radius
D	Diffusion coefficient
δ	Dirac delta function or phase angle
δ_0	Equilibrium cross-link distance
δ_{cl}	Distance for cross-link assignment
δ_w	Distance for wall bead assignment
$\delta\mathbf{u}_{cl}$	Cross-link displacement
$\delta\mathbf{u}_{cl}^{aff}$	Affine cross-link displacement
$\delta\gamma$	Strain increment
E	Young’s modulus
f_c	Euler buckling force
FCS	Fluorescence correlation spectroscopy
Φ	Volume fraction
g	Extracted temporal correlation function
g_0	Zero-lag correlation
$g_{s,\infty}$	Spatial offset for the correlation function
$g_{t,\infty}$	Temporal offset for the correlation function
G	Shear modulus
G'	Storage (elastic) modulus
G''	Loss (viscous) modulus

G^*	Complex shear modulus
$\tilde{G}$	Laplace transform of shear modulus
G_0	Shear modulus at the linear viscoelastic regime
G_L	Shear modulus beyond network nonlinear stiffening
G'_1	First-harmonic elastic modulus
G'_M	Tangent modulus at small strain
G'_L	Secant modulus at large strain
δi	Intensity fluctuation
i	Intensity
ICS	Image correlation spectroscopy
ICS-μR	Image correlation spectroscopy for microrheology
k_b	Bending constant
k_{cl}	Cross-link constant
k_i	Interaction constant
k_s	Stretching constant
k_B	Boltzmann constant
l	Length of rod-like fluorescent bodies
L	Fiber length
l_e	Entanglement length
l_m	Network mesh size
l_p	Persistence length
M_W	Molecular weight

MR	Mechanical rheology
n	System dimensionality
N_A	Avogadro’s constant
NA	Numerical aperture
ν	Viscosity
ν^*	Complex viscosity
P	Density distribution
ϕ	Spatiotemporal correlation function of density distribution
PSF	Point spread function
PTM	Particle tracking microrheology
ζ	Spatiotemporal correlation function of point spread function
r	Experimental spatiotemporal correlation function
$r(t)$	Particle position
R	Ratio between cross-linker concentration and polymer concentration
R_e	Number of entanglements per fiber
R_{cl}	Number of cross-links per fiber
$\left\langle \Delta r^2 \right\rangle$	Particle mean-squared displacement
S	Index of nonlinearity
σ	Intensity proportionality coefficient
t	Time
τ	Time lag or shear stress
τ_0	Amplitude of sinusoidally varying shear stress

τ_c	Critical stress
τ_r	Rupture stress
τ_D	Characteristic diffusion time
τ_{tr}	Transition time between two asymptotic power law exponents
T	Temperature
$\mathbf{u}$	Displacement vector
$\mathbf{u}^{aff}$	Affine displacement vector
U	Total energy
U_b	Bending energy
U_{cl}	Cross-link energy
U_i	Interaction energy
U_s	Stretching energy
V	Network rearrangement parameter
W	Simulation box size
ω	Frequency
x, y	Spatial (lateral) dimensions
ξ, η	Spatial lags corresponding to x, y
ξ_0, η_0	Location of Gaussian center
z	Spatial (axial) dimension

Chapter 1: Introduction

1.1 Soft matter

Soft matter, as its name suggests, is a class of materials that can be easily deformed, as a result of their unusual structural, mechanical, and chemical behaviors. The seemingly loose definition allows soft matter to encompass a wide range of systems of varying components, including colloidal dispersions, membranes, films, emulsions, surfactant assemblies, gels, liquid crystals, as well as synthetic and biological polymers. Integrating these materials together and naming and studying them under the single field of soft matter, however, is not just a matter of simplifying the nomenclature. Rather, it has been realized only in the past 10–20 years that many phenomena in these systems, which had previously been discovered and understood independently in each subfield, have the same underlying physical mechanisms [1]. This integration, together with the ever broader impact of understanding the properties of these systems in the society, has propelled the advancement of soft matter research in the recent years, especially with the blossoming of nanotechnology and biophysics of biological materials.

There are a number of common features among soft matter systems that distinguish them as a class of materials [2]. Chief among these are:

- The importance of the relation between structure and property at mesoscopic length scales. A soft matter system often self-organizes into characteristic physical structures much larger than its constituents at the atomic or molecular levels yet much smaller than the macroscopic scale of the material. The properties and interactions of these mesoscopic structures, in addition to the properties and interactions of the microscopic constituents, lead to many interesting behaviors at the larger length scales that are not easily predictable. Even more complexity arises when the spontaneous self-assembly takes place hierarchically, with multiple levels of supramolecular structures that interact with each other. This propensity of soft matter to self assemble into complex structure makes it form a major component of biological systems and technological applications.

- The importance of thermal energy. Typical structures in soft matter are small enough to undergo significant Brownian motion and fluctuation and for thermal energy to produce stochastic distortions in the structures. Such small energy scale needed to deform the structures is one of the origins of the macroscopic compliance characteristic of soft matter systems. As we shall discuss further, proper utilization of this information can in fact be useful in revealing the behavior of these materials in different length scales.

It is obvious that soft matter is characterized by complexity, both in structure and dynamics, which makes it difficult to derive quantitative theories for these materials. However, the apparent similarities in the behavior of soft matter systems call for more universal relationships [3]. This is the reason that scaling laws, which in essence evaluate how one variable depends on or vary with other quantities, have been central in studying soft matter systems. The concept of scaling was first introduced in the field of polymer physics by Pierre-Gilles de Gennes [4], and has since pervaded into various other fields in soft matter research and beyond. It is no wonder that de Gennes is now considered one of the founding fathers of soft matter [5]. He succinctly summarize the two outstanding features of soft matter in his Nobel Lecture: its *complexity* and *flexibility* [6].

Due to the various systems and applications that the term 'soft matter' covers, the study of soft matter has become a highly interdisciplinary subject, taking in aspects of physics, chemistry, materials science, and in specific cases also of biochemistry as well as chemical and mechanical engineering [3]. As a result, there are many directions from which one can approach soft matter systems. This thesis presents our contribution to the link between structure and mechanical behavior of soft matter systems at different length and time scales, with a particular application to polymer networks, using a combination of both established and newly developed mechanical characterization techniques.

1.2 Scale-dependent mechanics of soft matter

Traditional mechanics classify matters in two forms, solid and liquid. An ideal (Hookean) solid is characterized by perfectly elastic behavior: it deforms in proportion to the applied force and regains its original state when the force is removed. An ideal (Newtonian) liquid, on the other hand, is characterized by perfectly viscous behavior: it flows with a rate proportional to the applied force, where the constant of proportionality is the liquid viscosity. For shear deformation, these can be mathematically represented respectively as

$$\tau = G\gamma \qquad \text{(Hookean solid)} \tag{1.1}$$

and

$$\tau = \nu\dot{\gamma} \qquad \text{(Newtonian liquid),} \tag{1.2}$$

where τ is the shear stress, γ is the shear strain, $\dot{\gamma} \equiv d\gamma/dt$ is the strain rate, G is the shear modulus, and ν is the viscosity. Both shear modulus and viscosity are measures of the resistance of the material from being deformed, which are intrinsic properties of the material and are independent of system size. Eqs. (1.1) and (1.2) should ideally describe the full range of material response.

However, real materials, particularly soft matter, invariably behave in a way that combines the two idealized linear responses, leading to the term *viscoelasticity*. One hallmark of a viscoelastic material is that it responds to an applied stress in a time-dependent manner. At a long time scale, it may flow like a viscous fluid, but at a short time scale, it may behave like a typical solid, for example. As a consequence, proper mechanical characterization of viscoelastic materials often requires analyses over multiple time scales that are not necessary for conventional solids or liquids. In addition, in many soft matter systems, this time-dependent viscoelastic behavior is also dependent on material composition and microstructure as well as temperature, as we have mentioned earlier. This has two implications. First, the relatively large mesoscopic length scales relevant in the soft matter microstructure and the relatively small energy scale required to deform the material imply large structural relaxation times. Therefore, phenomena far from thermal equilibrium play a very important role [7]. Second, the possibility of having hierarchical structures in the soft matter requires careful examination of the mechanical behavior at different length scales to fully understand the material response. As an example, typical biological materials involve descriptions from length scales relevant to tissues ($\sim 10^{-3}$ m), cells ($\sim 10^{-5}$ m), biopolymer fibers ($\sim 10^{-7}$ m), macromolecules ($\sim 10^{-8}$ m), to atomic level ($\sim 10^{-10}$ m). In effect, the elastic and viscous 'constants', G and η, are no longer constants, but functions of time scale, length scale, and extent of deformation. All of this scale-dependent behavior of soft matter systems calls for multiple characterization approaches.

1.3 Characterization techniques of soft matter

In this section, we briefly survey the various characterization techniques for studying the structure and properties of soft matter. There are a large number of available techniques and many have been discussed and reviewed extensively elsewhere. Here, we only discuss typical applications of each technique, focusing on the type of measurements and the range of length and time scales that can be probed using the techniques. Some of these techniques will be used and discussed in more detail in the following chapters of this thesis.

1.3.1 Microscopy

When the relevant structural length scale of the material is on the order of micrometers, *optical microscopy* can be used to visualize the structures [8,9]. Birefringent structures, such as those formed by liquid crystals, can be identified using *polarized light microscopy* [10]. Large colloidal particles can be directly observed, for example using *difference interference contrast* (*DIC*) *microscopy* [11]. Many biophysical studies or those involving bio-inspired materials entail fluorescent labeling of the objects of interest, for which *fluorescent microscopy* is particularly useful [12]. The development of *confocal microscopy*, which allows thin, micrometer-level “optical slicing” through the material thickness, has also been instrumental in three-dimensional (3D) examinations of the structures, both in *fluorescent* or *reflection* mode [13].

Soft matter with structures of nanometer or sub-nanometer dimensions can be imaged using *electron microscopy* [14]. Electron microscopy can be broadly categorized into *scanning electron microscopy* (*SEM*) and *transmission electron microscopy* (*TEM*), with the main difference being SEM images the exterior of the object, while TEM involves sectioning of the bulk sample into nanometer-thick slices. Although electron microscopy has been successfully used to examine the microstructure of various soft matter systems, including biological materials, it is important to bear in mind that the sample has to be imaged in dry condition and often has to be stained or coated with heavy atoms to obtain sufficient electron density contrast in the imaged sample. These sample preparation steps can sometimes result in misleading structural artifacts. In addition, in contrast to optical microscopy, only static measurement can be done, as the sample has to be fixed.

Nanoscale surface structures can also be characterized using *scanning probe microscopy* (*SPM*) techniques [15], with *atomic force microscopy* (*AFM*) being one of the most commonly used [16]. AFM has been successfully used, either in the contact or tapping (non-contact) modes, to provide topological survey of material surfaces in high resolution. AFM can also be used in conjunction with *nanoindentation* techniques to measure the mechanical properties and hardness of the materials [17]. However, the basic principle of AFM makes it problematic when the material under examination is fairly soft.

1.3.2 Rheology

Rheology is the study of the deformation and flow of matter [18]. In a typical rheology experiment, a rheometer is used to apply a shear deformation to the sample and the viscoelastic response is measured. There are a number of types of measurements that can be performed to obtain the desired information on viscoelasticity [19]. In *stress relaxation* measurements, a strain is applied and held constant, while the decay of the resulting stress is monitored as a function of time. On the other hand, in *creep* measurements, a stress is applied and the increase in the resulting strain is monitored. The dependence of the material response on the strain magnitude and rate, which is often nonlinear in many soft matter systems, can likewise be directly measured. To more directly probe the time scale-dependent (or, equivalently, frequency-dependent) mechanical behavior of the material, dynamic mechanical testing can also be performed by applying *oscillatory* strain and monitoring the resulting stress waveform. The “elastic” and “viscous” contributions can then be analyzed separately by looking at the in-phase and out-of-phase response, respectively. The *time evolution* of the viscoelasticity, for example during phase transition or gelation events, can be directly observed by monitoring the response upon the application of small oscillatory strain over time. To interpret the rheological data obtained from these various protocols, a number of *constitutive relations*, such as the Maxwell model (for viscoelastic liquid) and Voigt model (for viscoelastic solid), have also been developed [20].

Shear deformation of the probed sample can be achieved using rheometers of various geometries. For example, the sample can be sheared between two horizontal *parallel plates*, where the strain varies with distance from the center of the plates, or between *a cone and a plate*, where the strain is constant throughout the sample. Liquid samples can also be measured using *Couette* geometry, where the sample is sheared between two vertical concentric cylinders, one of which is rotated while the other is fixed. Due to the size of the rheometer geometry, the sample volume is typically on the order of milliliters, and the probed length scale is in the micrometer or millimeter range.

There has been a recent upsurge in the demand for rheological measurements at smaller length scales, especially in the length scales relevant to biological cells, which are around a micrometer and smaller. To this end, *microrheology* has emerged as a branch of rheology that probes the rheology of materials at the length scales of the probe particles, typically micrometers [21]. In microrheology, the mechanical perturbation is applied to the sample through probe particles in the material either using external forces or by just relying on Brownian thermal noises native to the system. The probe particles could be physically introduced or indigenous.

1.3.3 Scattering and spectroscopy techniques

In scattering techniques, the sample is illuminated by beams and the intensity of the scattered light is used to analyze the sample properties [22]. Visible light is used in *static* (*SLS*) and *dynamic light scattering* (*DLS*) and the scattered light is analyzed as a function of scattering angle in SLS or correlated in time in DLS to estimate particle size or diffusion properties for particles with sizes comparable to light wavelength (~380–750 nm) [23]. Materials with smaller features require beams with shorter wavelengths, such as in *X-ray* and *neutron scattering* [24]. X-ray is scattered by electrons and the scattering angle varies with the structural spacing in the sample, leading to further categorization into *wide angle X-ray scattering* (*WAXS*) [25] and s*mall angle X-ray scattering* (*SAXS*) [26]. X-ray scattering has been particularly useful in providing information on the structure of nanometer-level crystalline polymers. The principle for neutron scattering is similar, but neutrons are scattered by atomic nuclei instead, which leads to the major use of *small angle neutron scattering* (*SANS*) in the field of polymer and soft matter physics [27].

At even smaller length scales, *nuclear magnetic resonance* (*NMR*) is useful in probing both the static order and the dynamic within materials, by carefully analyzing the motion of the magnetically excited nuclei [28]. NMR has been useful in providing information, for example, of the orientational ordering and dynamics of liquid crystals and hydrocarbon chains in micelles. *Infrared* (*IR*) *spectroscopy* and *Raman spectroscopy* can also be used to infer microstructural information at such small length scales, such as chain branching and orientation of polymer [29].

1.3.4 Computer simulations

The need for multiscale characterization of soft matter, together with the rapidly increasing power of computers, makes computer simulations a valuable tool in understanding soft matter. Modeling of soft matter systems can be done at multiple levels, from atomistic, molecular modeling in *Molecular* and *Brownian Dynamics* (*MD* and *BD* respectively) systems [30], all the way to bulk material modeling with constitutive relations in *finite element* (*FE*) *analysis* [31]. The propensity of soft matter systems to form hierarchical, mesoscopic structures also allows efficient *coarse-grained* modeling. One particular advantage of computer simulation is that the input parameters can be generated much more precisely and reliably compared to experiments, which in turn allows generic characterization and prediction of material behavior that are difficult to gain, if accessible at all, from experiments alone.

In summary, each experimental and computational characterization technique has its own strengths and weaknesses, as well as ranges of applicability. To study complex materials like soft matter, therefore, employing just one technique is often insufficient to completely understand the underlying principles of material behaviors. For example, interpretation of mechanical rheology data is sometimes difficult without concurrent *in situ* characterization of the material's microstructure. These difficulties have prompted a variety of schemes for combining the available techniques, for example in *rheo-optical measurements*, where the sample is deformed while the microstructural changes are monitored real-time using imaging or scattering techniques [32,33]. In this thesis, we employ similar multi-pronged approach to study the mechanical behavior of soft matter. The organization of this thesis is summarized in the next section.

1.4 Scope and Structure of the Thesis

In the first part of the thesis, we investigate the mechanical behavior of networks of collagen, the most abundant protein in mammals. Collagen fibrils form complex hierarchical structures with a great variety of properties, and collagen networks play an important role in determining the stiffness and force transmission in biological tissues. In Chapter 2, we study the microstructure and bulk mechanical properties of collagen networks using microscopy and mechanical rheology. We show that pure collagen networks do not exhibit the expected behavior of densely entangled fiber networks, but are instead better described by the cross-linked semiflexible polymer network model. We propose a deformation mechanism involving fiber rearrangement and dynamic bond binding that can explain the observed strain softening and strain stiffening of the network. In Chapter 3, we develop a discrete, 3D network model of realistic semiflexible fibers to represent typical biopolymer networks and numerically study the microscopic mechanical response. We find that two structural properties, namely, fiber entanglement and network connectivity, govern the full nonlinear response at different length scales and different strain levels. The model underscores the importance of taking into account fiber morphology and network heterogeneity. In Chapter 4, we employ particle tracking microrheology to experimentally investigate the microscale mechanical properties of collagen networks. We find that not only is the network mechanics length-scale dependent, but there is also a large variation in the stiffness due to network heterogeneity. We discuss several experimental limitations of the technique that warrant further investigations.

In the second part of the thesis, we develop a new microrheological technique based on image correlation spectroscopy (ICS). In Chapter 5, we propose and demonstrate the use of ICS as a novel tool for microrheological measurement of soft matter systems. We test the method on both Newtonian and complex fluids with different viscoelastic properties and compare the results with those obtained using mechanical rheology. In addition, we develop a special method for extracting the mean-squared displacement of the probe particles from the correlation data that can also be useful in other microrheological techniques. In Chapter 6, we present a mathematical formalism for ICS that allows dynamic measurement in a probe-independent manner. We test the method using both simulated and experimental confocal images. The possibility of simultaneously obtaining microstructural information, spatiotemporal biophysical information, and microrheological information from a single set of image data makes ICS a prospective tool for studying soft matter.

Chapter 2: Macromechanics of Collagen Networks

2.1 Introduction

2.1.1 Collagen

Collagen is the most abundant protein in mammals and the main constituent of human connective tissues [34]. It is estimated that more than 30% of total protein in human body is represented by collagen [35]. Collagen is a key structural and mechanical component in load-bearing tissues such as bones, tendons, ligaments, skin, and even muscle. Collagen is also believed to play many physiological functions other than mechanical due to its specific interactions with molecules and cells. Not surprisingly, mutations in collagen have been associated with various connective-tissue and bone disorders [36].

Being a key building material of human body, collagen possesses incredible versatility in determining the mechanical integrity of various human tissues. This versatility arises from its complex hierarchical structure, where adaptation is possible at every level, enabling a great variety of properties and functions [37]. Collagen consists of tropocollagen molecules with length ~ 280 nm and diameter ~ 1.5 nm, which form staggered arrays typically called fibrils with diameter of tens to hundreds nm, which in turn is the basic building block of collagen-rich tissues [38]. These fibrils assemble in different organizations and combine with different molecules and minerals into composite materials with a variety of complex structures and mechanical properties.

In vivo, collagen forms fiber networks with location-dependent microstructural features that provide complex 3D environments for cells.[1] Naturally, collagen networks provide excellent platforms as tissue and extracellular matrix equivalents for studies of cell behavior and applications in bioengineering. Indeed, collagen gels have increasingly been used as a biocompatible scaffold for artificial tissue growth [39,40], as well as cell motility [41] and even tumor invasion studies [42,43]. The mechanical properties of the extracellular matrix profoundly affect various cell functions, including differentiation and migration [44,45], while, conversely, cells can actively remodel their surrounding microenvironment through, for example, matrix deposition and degradation [46,47]. Given the vital role of collagen in tissue microstructure and elasticity, it is imperative that the mechanics of collagen networks be well understood.

2.1.2 Bulk characterization of collagen networks

Collagen, together with other biological fibrillar proteins such as cytoskeletal proteins, fibrin, and nucleic acids, belongs to a class of materials known as biopolymer [48]. One hallmark of biopolymer networks is their strain-dependent viscoelasticity. In particular, biological tissues, cells, as well as reconstituted biopolymer networks, including collagen networks, exhibit nonlinear network stiffening—the networks becomes harder to deform at large strains—that results in

---

[1] Fiber is sometimes defined as a collection of fibrils with certain directional correlation. However, in networks, it is often difficult to distinguish fibrils from fibers. In this thesis, we use the terms fiber and fibril loosely and interchangeably.

enhancement of network integrity at large strains [49,50]. It has been realized that this apparent universality of biopolymer network response has its roots in the fact that biopolymers also belong to the class of semiflexible polymers, so called because the structural length scales of the networks, such as the mesh size or the fiber contour length, are comparable to the length scale of the polymer semiflexibility, often quantified through the persistence length l_p [51]. Although the properties of individual semiflexible polymers [52-56] as well as the dynamics and mechanics of these polymers in solution [56-61] have been elucidated extensively both experimentally and theoretically, those of semiflexible polymer networks are not well understood. The origin of the strain stiffening phenomenon in these networks, including collagen, is therefore still unclear.

Under appropriate conditions, collagen is known to self-assemble *in vitro* to form percolated networks [62]. The self-assembly process is highly sensitive to polymerization conditions such as temperature, pH, and ionic strength, and results in heterogeneous networks with local variations of fiber topology and microarchitecture [63,64]. Moreover, the nature of this entropy-driven self-assembly and the underlying interfiber interactions are not well understood and are still being actively studied (see, *e.g.*, [65] and the references therein). Consequently, collagen networks have complex mechanical properties and the interpretation of experimental data for collagen networks is not straightforward. To tackle this problem, researchers have started to examine the relation between the microstructure of collagen networks and the corresponding mechanical properties by exploiting various non-invasive methods that allow visualization of collagen fibers during gelation as well as tensile testing [65-68].

In this chapter, we attempt a phenomenological investigation of the mechanics of collagen networks by systematically probing the viscoelasticity of collagen networks as a function of applied strain and collagen concentration. We use simple, continuous shear rheometry to measure the rheological properties of collagen networks reconstituted *in vitro* and show that, even without any addition of external cross-linkers, the mechanical behavior of collagen networks can be described well by a model based on cross-linked semiflexible networks. At higher levels of strain, however, only partial agreement with the theoretical predictions is found. In particular, the interplay of stress- and strain-triggered network softening and stiffening as well as rubber-like cyclic softening behavior are observed. We propose a model for the deformation mechanism based on the dynamics of cross-link bonds that can explain the behavior.

2.2 Materials and Methods

2.2.1 Collagen hydrogel preparation

Type I collagen extracted via acid-solubilization of rat-tail tendon, with a concentration of 9.03 mg/ml in 0.02 N acetic acid, was obtained from BD Biosciences (Bedford, MA). Depending on the desired final concentration (c = 1.5–7.5 mg/ml), appropriate amounts of the collagen stock solution were mixed on ice with 10% (v/v of the final solution) 10× phosphate-buffered saline (PBS), 1 N NaOH (predetermined to adjust the final solution pH to 7.4), and 1× Dulbecco's Modified Eagle's Medium (DMEM) (predetermined to achieve the desired total volume). All solutions were prepared and kept on ice prior to collagen gelation.

2.2.2 Confocal reflection microscopy

To visualize the microstructure of the formed collagen networks, confocal reflection microscopy (CRM) imaging was performed. CRM is widely used in polymer research and the manufacturing industry, and more recently also in cell biology, owing to the simplicity of obtaining images of unlabeled sample and the possibility of simultaneous cell imaging [43,46,69-71]. In CRM, a point laser is used to scan a sample and differences in contrast largely result from a different in refractive index between the medium and the scattering collagen fibrils. In 3D collagen networks, a penetration depth of 100–200 μm can be reached, although the signal-to-noise ratio and resolution decrease with depth.

Collagen networks were formed by loading 200 μl of prepared collagen solutions in the well of glass-bottom dishes (MatTek Corp., Ashland, MA) and incubating at 37°C for at least an hour to allow gelation. To mimic the condition in cell assays, the formed gels were hydrated by adding 2 ml phenol red-free DMEM (GIBCO/Invitrogen, Carlsbad, CA) containing 10% FBS and 1% penicillin/streptomycin. CRM images were recorded with an inverted confocal laser scanning microscope (Nikon TE2000) equipped with a 60×, NA = 1.49 oil objective. The samples were illuminated with continuous diode laser (Olympus) at 514 nm and the back-scattered light was collected. All images were collected at 37°C.

2.2.3 Mechanical rheology

Rheological measurements were conducted on a temperature-controlled AR-G2 rheometer (TA Instruments, New Castle, DE) in continuous shear mode. Parallel-plate geometry with a plate diameter of 40 mm was used in conjunction with a solvent trap to minimize evaporation. *In situ* polymerization of collagen network was done by applying 630 μl of the prepared collagen solution at desired concentration on the rheometer Peltier stage (pre-cooled at 5°C) and raising the temperature to 37°C. Preliminary oscillatory time-sweep tests confirm that the gelation plateau is reached within the first hour, and all further measurements were accordingly done after allowing 90 minutes of gelation. Different measurement protocols were used to probe the mechanical properties of collagen networks and will be discussed in detail separately.

2.3 Results and Discussion

2.3.1 Collagen network microstructure

The microstructure of biopolymer networks, including collagen, is expected to heavily affect the mechanical properties of the networks. For this reason, various imaging-based methods have been used to both qualitatively and quantitatively assess the microstructure of collagen networks. The most common methods include confocal fluorescence microscopy (CFM), multiphoton microscopy such as second harmonic generation (SHG) imaging, confocal reflectance microscopy (CRM), and electron microscopy. Typical CRM images of collagen networks of different concentrations (c = 1.5–7.5 mg/ml) are shown in Figure 2.1. It can be observed that, within this range of concentration, the collagen fiber density, topology, and spatial structure generally vary with concentration.

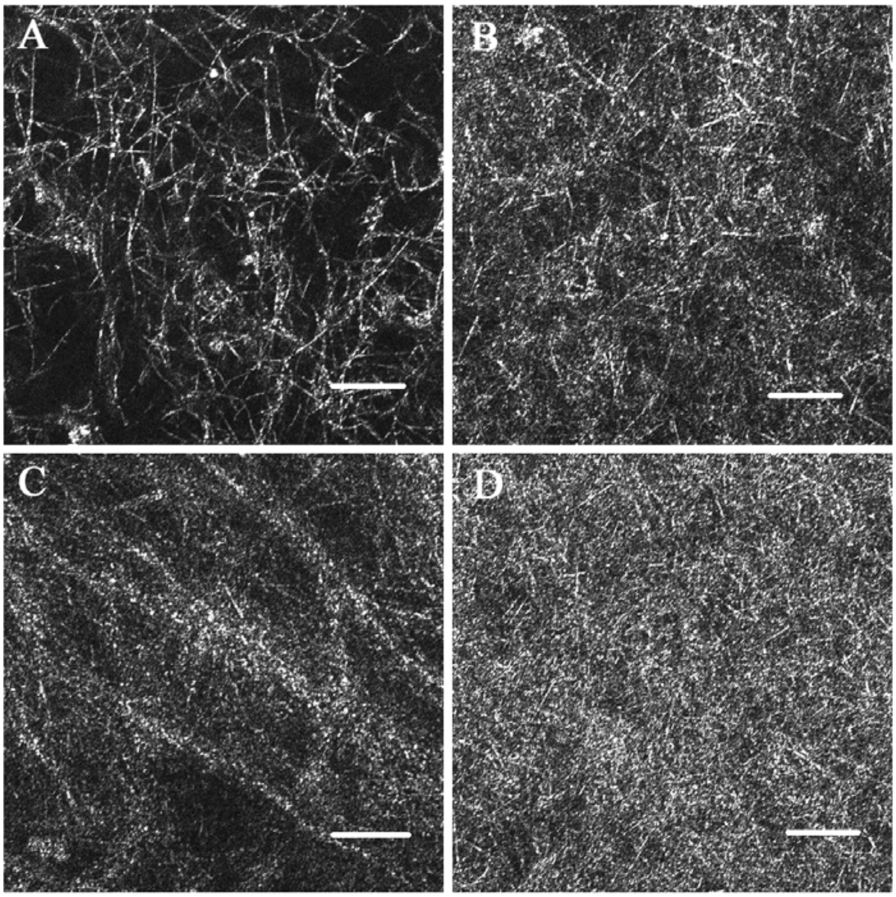

Figure 2.1: Confocal reflection microscopy images of collagen networks. The differences of microstructure of networks with different collagen concentration can be observed for c = 1.5 mg/ml (A), c = 3.5 mg/ml (B), c = 5.5 mg/ml (C), and c = 7.5 mg/ml (D). The scale bars represent 10 μm.

More quantitative analyses on images of the network microstructure obtained using the abovementioned imaging techniques have been conducted, such as extraction of fiber density and topology [65,72-74], orientation [68,75], mesh or pore size [73,76], and even for direct image-based prediction of the network mechanical properties [77,78] and strain transmission [66], with varying degree of success. However, there are several drawbacks of such image-based microstructural analysis of networks. First, imaging techniques can produce artifacts that need to be treated very carefully. High-quality visualization of labeled collagen fibers can be obtained using CFM, but the labeling procedure itself can modify the self-assembly of the network and, as a result, provide misleading information on the native state of network structure. CRM is very useful to provide structural information for unlabeled collagen networks, but has inferior signal-to-noise ratio compared to CFM to be used for quantitative structural analysis. In-plane and axial diffraction artifacts have been found to cause overestimation of fiber diameter and fiber density, respectively [79,80]. In addition, it has been found recently that fiber brightness becomes a function of fiber orientation in CRM, leaving fibers angled at more than ~ 50° from the imaging plane entirely undetected [75]. In general, optical microscopy also has spatial resolution limits that preclude visualization of features smaller than ~ 100–200 nm. Electron microscopy allows imaging with nanometer resolution, but the necessary sample preparation, such as sample dehydration, often directly alter the structural features [81]. Without careful examination, therefore, image-based analyses can result in misleading microstructural information.

Secondly, we find that image-based analyses are highly sensitive to user-defined post-processing parameters. For instance, estimation of network mesh size requires image thresholding to minimize the imaging noise [42,76]. However, slight changes in the threshold value (which are usually set manually or semi-manually based on the intensity of non-fibrous areas) can result in significant variation in the mesh size value. This problem is even more serious when the fibers are not easily distinguishable, as is the case for the higher range of c [*e.g.*, Figure 2.1, (C) and (D)]. Misleading information can also be obtained for low c, where only large fibers are visible and there is a perceived lack of interconnection between fibers.

In view of the problems associated with network structure estimation from images, we decided instead to study the mechanics of collagen networks directly using a mechanical rheometer, while independently examining the role of network structure at different length scales computationally, which will be discussed in Chapter 3.

2.3.2 Rheology of collagen networks

We polymerize type I collagen gels *in situ* between the parallel plates of a rheometer, where the neutralized precursor solutions form isotropic networks upon heating to 37°C. The typical mesh size, fiber length and diameter of collagen networks formed under these conditions have been estimated from confocal images and electron micrographs to be l_m ~ 1–30 μm, L ~ 6–8 μm and d ~ 30–130 nm respectively, albeit with considerable variation and heterogeneity within each sample [65,72,74]. The rheometer gap (h = 500 μm) was chosen such that h is much larger than any characteristic length scales of the samples to avoid any size effects [82]. The mechanics of the formed networks is measured by applying oscillatory strain $\gamma(t) = \gamma_0 \sin(\omega t)$, with variable frequency ω and amplitude γ_0, as schematically illustrated in Figure 2.2. For a Hookean solid, this leads to a stress in phase with the strain, while for a Newtonian liquid, the stress depends on the rate of strain $d\gamma/dt$, resulting in a phase shift of $\pi/2$ in the response. Generally, for viscoelastic materials, the resulting stress is described by $\tau(t)=\tau_0\sin(\omega t+\delta)$ with a phase shift δ, as illustrated in Figure 2.3. The material can then be characterized by the elastic modulus $G'=(\tau_0/\gamma_0)\cos\delta$ and the loss modulus $G''=(\tau_0/\gamma_0)\sin\delta$, measures of the stored and dissipated energy in the network, respectively. For brevity, hereafter we refer to γ (rather than γ_0) as the oscillatory strain amplitude, while $\gamma(t)$ represent the instantaneous shear strain.

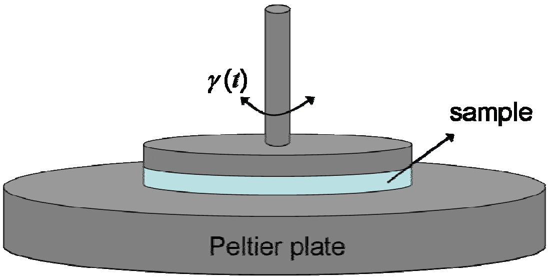

Figure 2.2: Schematic of oscillatory rheology measurement. The top plate is rotated sinusoidally based on $\gamma(t)$, while the temperature-controlled bottom plate is fixed.

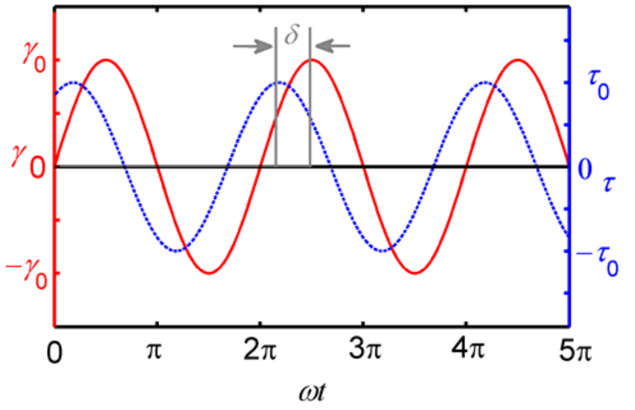

Figure 2.3: Typical stress-strain oscillatory response of viscoelastic material. The stress $\tau(t)$ (dashed line) and strain $\gamma(t)$ (solid line) signals are phase shifted by an angle δ.

Characterization of G' and G'' as a function of frequency ω at small strain amplitude (γ = 1%) shows that over the measured frequency range (ω = 0.1–100 rad/s), G' is ≈ 6-fold larger than G'', with G' values of 10–100 Pa, as shown by the solid symbols in Figure 2.4. This result signifies that collagen networks are soft, predominantly elastic gels, consistent with previous reports [65,83]. Moreover, both G' and G'' exhibit very weak frequency dependence, scaling as $G' \sim \omega^{0.08}$. Thus, in the time scales relevant to cellular dynamics (*i.e.*, on the order of seconds), therefore, collagen scaffolds are elastic with little time-scale dependence. The collagen concentration c modulates the stiffness of the networks without affecting their frequency dependence. Not surprisingly, higher c results in stiffer networks. For simplicity, we use the moduli at ω = 1 rad/s as the typical moduli values (*i.e.*, reference values) for the remainder of this chapter.

Physiologically, tissues and networks are exposed to large strains as a result of large-scale body movements and small-scale cell motility. Therefore, it is equally important to examine the mechanical behavior at large strains. To this end, we vary the shear strain amplitude γ in the rheological measurements. Figure 2.5 shows that the collagen networks exhibit highly strain-dependent mechanical response over almost four orders of magnitude of γ. The network stress τ increases roughly linearly with γ at small strain, in what is typically termed the "linear viscoelastic" regime. As γ is gradually increased, there is a critical strain γ_c beyond which the slope of the τ vs. γ curve increases noticably, thus indicating a nonlinear response. At very large strains, τ starts to dramatically drop, indicating network rupture. This nonlinear behavior is prevalent in, and consistent with the behavior of, a number of tissues and biopolymer networks.

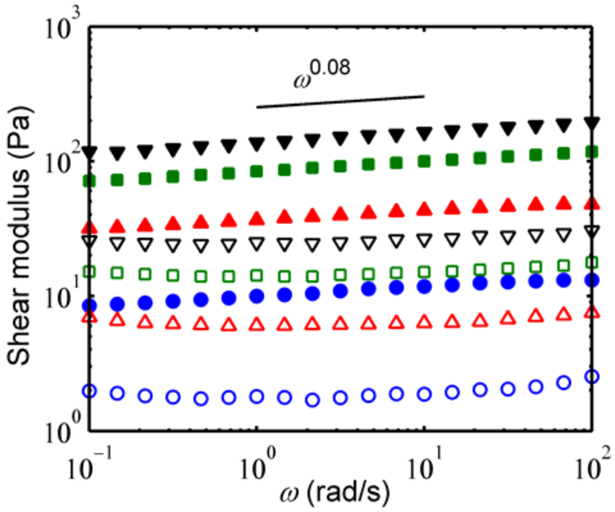

Figure 2.4: Frequency dependence of the shear moduli of collagen networks. The storage modulus $G'(\omega)$ (filled symbols) and the loss modulus $G''(\omega)$ (open symbols) are shown as a function of frequency ω for different collagen concentrations c = 1.5 mg/ml (circles), c = 3.5 mg/ml (upright triangles), c = 5.5 mg/ml (squares), and c = 7.5 mg/ml (inverted triangles). The frequency sweep measurements were performed in the frequency range of ω = 0.1–100 rad/s at 1% strain. Both G' and G'' have weak frequency dependence. A solid line of $\omega^{0.08}$ is displayed as a guide to the eye.

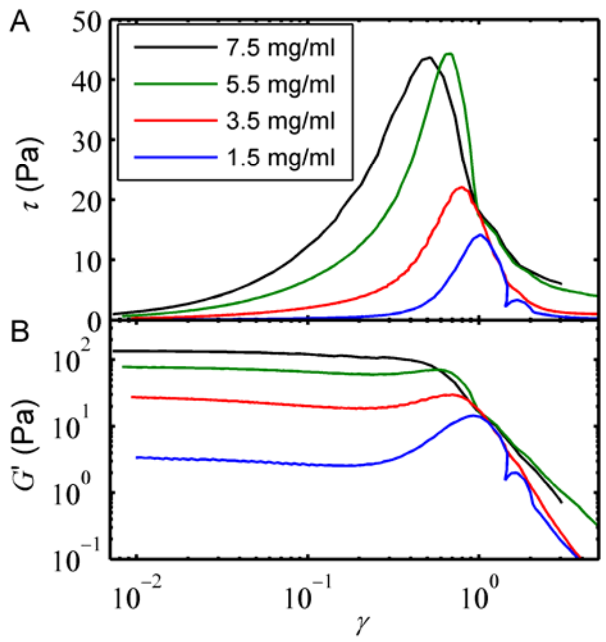

Figure 2.5: The mechanics of collagen networks in response to oscillatory shear deformations. The shear stress τ in (A) and the storage modulus G' in (B) are shown as a function of the strain amplitude γ for different collagen concentrations c = 1.5–7.5 mg/ml over almost four orders of magnitude of γ. Except for c = 7.5 mg/ml network, G' exhibits an increase with γ, indicating strain stiffening, before a drop at very large γ, indicating network rupture. All measurements are done at fixed frequency ω = 1 rad/s and temperature of 37°C. The data points are obtained with logarithmically increasing γ.

We plot the measured strain-dependent elastic modulus $G'(\gamma)$ in Figure 2.5(B). The corresponding viscous modulus $G''(\gamma)$ is always smaller than $G'(\gamma)$ for γ < 5 and is not shown. There are two interesting features that can be observed. First, at small γ < 25%, G' decreases with γ, indicating apparent network softening. To show an example of this effect more clearly, the data points for c = 3.5 mg/ml in Figure 2.5 are replotted in log-linear scale in Figure 2.6. Second, the network strain-stiffening beyond γ_c, as indicated by the increase of $G'(\gamma)$ with γ, becomes less pronounced as c increases and does not occur at all for the higher range of c tested (c = 7.5 mg/ml). The physical mechanism behind such a nonlinear mechanical behavior of collagen networks is still poorly understood. In the next two sections, we discuss in detail how the rheological properties of collagen networks can reveal the mechanics of network deformation.

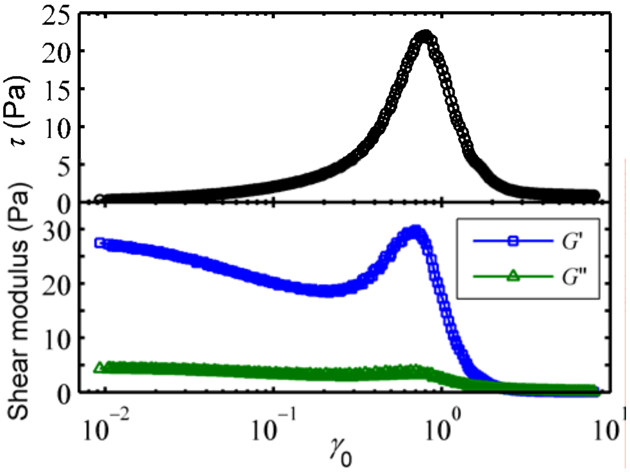

Figure 2.6: Stress τ and shear moduli G' and G'' of collagen network under oscillatory shear with varying strain amplitude 1% < γ < 800%. The network is polymerized at 3.5 mg/ml concentration and pH 7.4. The measurement is done at ω of 1 rad/s, 37°C, and logarithmically increasing γ.

2.3.3 Amplitude-dependent oscillatory shear measurement

Although the shear stiffening behavior is anticipated, the softening of biopolymer networks at small strains is unexpected and has been reported, to our knowledge, only in desmin and microtubule networks [84,85], without substantive explanation. To visualize the actual network response during the oscillatory testing, we generate the plots of instantaneous stresses $\tau(t)$ against strains $\gamma(t)$, often called Lissajous plot, for different strain amplitudes γ. For purely elastic materials (Hookean solid), the response is sinusoidal and in phase ($\delta = 0$) and the Lissajous plot collapses to a line with a slope of G', while for purely viscous materials

(Newtonian liquid), the response is sinusoidal and out of phase ($\delta = \pi/2$) and the Lissajous plot is a circle. Viscoelastic materials like biopolymer networks exhibit both elastic and viscous properties, and the Lissajous plot is expected to be a perfect ellipse, with G' as the slope of the semimajor axis. As shown in Figure 2.7, however, this ellipse assumption (and the underlying assumption of sinusoidal response) is only valid at small γ (γ < 5%), while oscillations with larger γ result in increasingly distorted response. Specifically, the slope of $\tau(t)$ vs. $\gamma(t)$ becomes larger at larger strains, implying network stiffening, even in the softening regime as initially remarked in Figure 2.6. This apparent contradiction is a result of the above assumption that the response waveform is strictly sinusoidal.

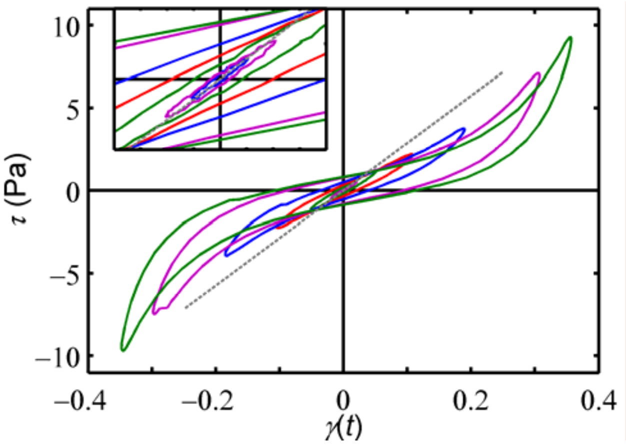

Figure 2.7: Lissajous plots generated from the stress-strain waveforms at different γ. The inset is a zoom in for $|\gamma(t)|$ < 4%, showing the ellipses as expected in the linear viscoelastic regime. For γ > 5%, the Lissajous plot becomes distorted, indicating nonlinear behavior. The dotted line is extrapolated from the semimajor axis of the innermost ellipse.

Different methods have been developed to deal with the nonsinusoidal nature of the stress waveform at large oscillation amplitude. One experimental option is to apply a steady prestress to the material, rather than applying a large-amplitude oscillation, and to measure the mechanical properties by monitoring the linear response upon the application of small, additional oscillation [86]. The measured modulus is called differential modulus, K, which is conceptually similar to taking the local slope of the stress. However, although this method can circumvent the problem with nonsinusoidal response at large deformation, it does not take into account the viscous relaxation and flow of the material upon application of prestress. Alternatively, the nonsinusoidal waveform can be analyzed in terms of Fourier transform rheology and decomposed into different harmonic contributions [87]. The sinusoidal approximation in typical rheology measurement can thus be viewed as only taking the first harmonic response, while the nonlinear distortions due to network stiffening arise from the higher harmonic contributions. The drawback of this method is that the higher harmonic coefficients do not necessarily admit clear physical interpretation of the mechanics of the probed material.

To address the issues associated with these methods, additional parameters that allow more direct interpretation of the nonlinear phenomena have been introduced [88]. Amongst these parameters, two moduli are particularly relevant in quantifying the elasticity of the material: the minimum-strain modulus $G'_M = \left(d\tau/d\gamma\right)\big|_{\gamma(t)=0}$ and the large-strain modulus $G'_L = \left(\tau/\gamma\right)\big|_{\gamma(t)=\pm\gamma}$. Specifically, G'_M is the tangent modulus at $\gamma(t)=0$, where the strain rate $\dot{\gamma}$ is at a local maximum, $d\dot{\gamma}/dt = 0$, and changes in τ are therefore related only to elasticity, while G'_L is the secant modulus at the maximum strain $\left|\gamma(t)\right| = \gamma$, where $\dot{\gamma} = 0$ and the residual stress in the sample results only from the elasticity of the material. These definitions can be easily visualized and compared to the standard first harmonic elastic modulus G'_1 using the Lissajous plot, as shown in Figure 2.8, and can be conveniently related to the higher harmonic coefficients [88]. At small strains, the Lissajous plot is elliptical, so both G'_M and G'_L converge to the linear elastic modulus, $G'_M = G'_L = G'_1 = G'$. At larger strains, a difference between G'_M and G'_L signifies a nonlinear elastic response. The deviation from the linear viscoelastic response can thus be quantified using an index of nonlinearity, $S \equiv \left(G'_L - G'_M\right)/G'_L$, where $S = 0$ indicates linear elastic response, while $S > 0$ and $S < 0$ correspond to intracycle strain stiffening and softening phenomena, respectively. The upper limit of S is unity and is achieved as $G'_L \gg G'_M$.

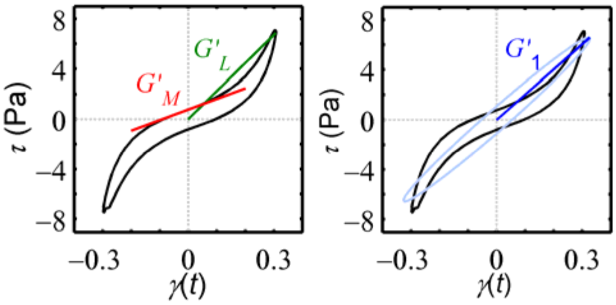

Figure 2.8: Graphical description of the elasticity measures. The left panel shows how G'_M and G'_L are obtained, while the right panel shows that the standard first-harmonic approximation assumes an ellipse response with the slope of the semimajor axis as G'_1.

The variations of the elastic moduli G'_M, G'_L, and G'_1 in collagen networks are plotted as functions of γ in Figure 2.9. All three moduli converge as expected in the linear regime and initially decrease with γ, indicating intercycle strain-softening as observed above. The first-harmonic elastic modulus G'_1 falls between the two other measures for all γ, suggesting that it acts as a first-order, average measure of elasticity. But while the small-strain elasticity G'_M continues to decrease at large γ, G'_1 and the large-strain elasticity G'_L start to increase around γ ~ 15% and γ ~ 25%, respectively, indicating strain-stiffening before network rupture. The divergence of these measures marks the onset of nonlinearity around γ ~ 5%, much earlier than the strains at which stiffening in both G'_1 and G'_L start to occur. This is confirmed when we plot S as a function of γ in Figure 2.9, which shows that S is initially close to zero, but that it gradually increases with γ, implying the increasing degree of intracycle strain-stiffening of the network. It is interesting to note that S never takes on negative values, within experimental error, meaning that no intracycle network softening is observed, although G'_1 reports initial (intercycle) softening before stiffening.

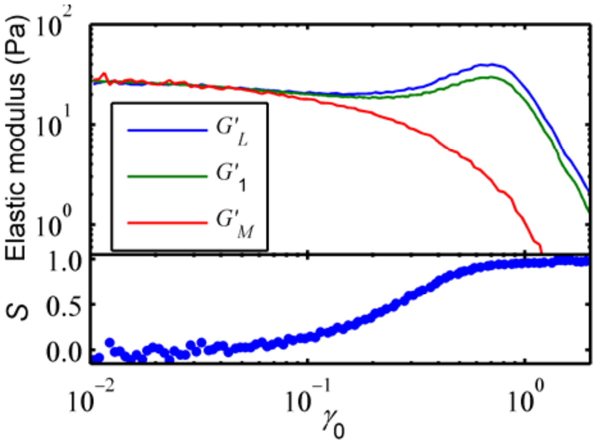

Figure 2.9: Elastic moduli of collagen network as a function of strain amplitude γ_0. G'_1 falls between G'_M and G'_L, suggesting that it is an average elasticity measure. The nonlinearity index S increases with γ_0 (intracycle strain stiffening), even when the elastic moduli decreases with γ_0 (intercycle network softening).

The framework used here provides a more complete and richer picture of the viscoelasticity of collagen networks that is inaccessible from the first-harmonic moduli alone. For example, while network softening at small strains followed by stiffening at larger strains is observed from standard interpretation of oscillatory rheology, a more detailed analysis on the stress-strain response in each deformation cycle reveals an early strain-stiffening of the network, even in the apparent (intercycle) softening region. Such analysis will augment the interpretation of rheological measurements on various materials, including biopolymer networks of cytoskeletal protein constituents and extracellular matrices. In the next section, we discuss how the rheological properties of collagen networks can be explained in relation to established theories on semiflexible polymer networks.

2.3.4 Strain-dependent mechanics of collagen networks

The semiflexible nature of a collagen fiber is reflected in the observation that its persistence length l_p is comparable to the fiber length L and network structural parameters such as l_m. Geometrical estimation of l_p based on imaged collagen fibers results in a l_p range of 6–20 μm [72,89]. Collagen gels have been argued to simply consist of uncross-linked, tightly entangled networks of semiflexible polymer chains [77]. The mechanics of such networks has been modeled by Morse [59,90], and the linear elastic modulus is predicted to follow $G' \sim c^{7/5} l_p^{-1/5}$. The bending stiffness of the fiber, and therefore l_p, is expected to increase with the fourth power of fiber diameter d [91], as has been verified experimentally for collagen [92]. In addition, we and others have previously established that, for collagen gels formed at

37°C, d does not vary with c [73,93]. Consequently, the Morse model predicts a scaling relation between G' and c with an exponent of 7/5. However, we find that, in the linear viscoelastic regime, the collagen network stiffness G' varies as $G' \sim c^{1.9}$ over the range c = 1.5–7.5 mg/ml, as shown in Figure 2.10(A). Similar scaling exponents have also been reported in the literature over smaller ranges of c [73,78]. The disagreement with the Morse model suggests that collagen networks cannot be described simply as entangled semiflexible networks.

The Morse model does not accommodate cross-links between fibers, but the mechanics of cross-linked semiflexible chain networks has been modeled by MacKintosh *et al.* [94]. By assuming affine network deformation, dense entanglements or cross-links, and $l_m \ll l_p$, this model predicts another scaling relation $G' \sim l_p^2 l_m^{-2} l_e^{-3}$, where l_e is the average distance between entanglements. The two microstructural parameters l_m and l_e depend on polymer concentration, and scale as $l_m \sim c^{-1/2}$ and $l_e \sim l_p^{1/5} c^{-2/5}$ for $l_m \ll l_p$ [52,94]. We thus obtain $G' \sim c^{11/5}$. The scaling exponent found for collagen networks is quite close to this predicted value. The agreement of the experimental results with the MacKintosh model but not with the Morse model suggests that collagen gels can be better described as cross-linked networks, even in the absence of externally introduced cross-linkers.

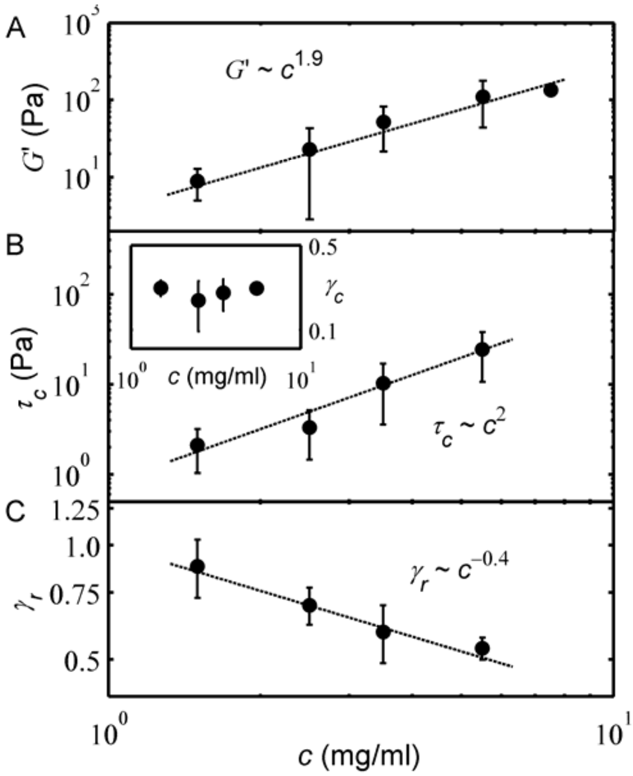

Figure 2.10: Scaling of the nonlinearity parameters of collagen networks with collagen concentration c. The linear viscoelastic storage modulus G' (A), critical stress τ_c (B), and rupture strain γ_r (C) all exhibit scaling relations with c (dashed lines) for a range of c = 1.5–7.5 mg/ml. In contrast, there is no observed correlation between the critical strain γ_c and c, as shown in the inset of (B). The modulus G' data is obtained at γ = 10%. At other strain amplitudes γ < 10%, the scaling $G' \sim c^{1.9}$ is unchanged. The critical stress and strain are assessed at the point where $G'(\gamma)$ starts to increase beyond the initial linear regime, while γ_r is evaluated where $G'(\gamma)$ is maximum before network rupture. There is no data point for τ_c, γ_c, and γ_r with c = 7.5 mg/ml networks, since no strain stiffening is observed and it is difficult to determine precisely the strain at which network rupture starts.

To examine the nature of these cross-links, we study the behavior of collagen networks beyond the linear regime. As the MacKintosh model also allows one to estimate the level of strain at which the network starts to exhibit nonlinearity, γ_c, given by $\gamma_c \sim l_e / l_p$, we use the scaling arguments used therein to obtain the result that $\gamma_c \sim c^{-2/5}$. The critical strain γ_c can be obtained experimentally from the stiffness-strain curves, such as those in Figure 2.5(B), from the values of γ at the start of strain-stiffening. However, we do not observe a good correlation between c and γ_c, as shown in the inset of Figure 2.10(B). On the other hand, one can also quantify the critical stress that marks the onset of nonlinear stiffening, τ_c. It has been theoretically shown that, for cross-linked semiflexible polymer networks, what controls the cross-over into the nonlinear entropic mechanics is the Euler buckling force $f_c \sim l_p l_c^{-2}$ [95]. For isotropic semiflexible networks, $l_c \sim \xi$ [96]. If the area occupied by each filament is ξ^2, then $\tau_c \sim c^2$. This scaling relation can be seen from our results [Figure 2.10(B)].

The finding that the onset of nonlinear behavior is governed by network stress τ_c, with the expected scaling behavior for cross-linked semiflexible networks, but not strain γ_c, can be attributed to the nature of the cross-links in collagen networks. The scaling relation between γ_c and c as predicted by the MacKintosh model is based on the assumptions of affine deformations and permanent cross-links. In uncross-linked collagen gels, however, any interaction between the fibers is likely to be relatively weak and transient. This is evident from the phase angle δ, characterizing the ratio between the two moduli ($\tan\delta = G''/G'$), which we find to be ~10° for the range of c tested here. The relatively large magnitude of δ reflects the existence of higher amounts of weak, non-covalent cross-links, which are likely to be in the form of hydrogen bonds as well as van der Waals interactions, in collagen networks compared to cross-linked hydrogels [97]. We hypothesize that during shear-straining at intermediate γ, the network rearrangement in the collagen gels involves, in addition to the expected fiber realignment, the breaking of bonds or fiber-fiber junctions and reformation of these bonds elsewhere, thereby leading to nonaffine deformation. This transient bond 'sliding' allows an extended level of strain before nonlinearity in the network response is reached. The dependence of critical stress τ_c on concentration remains as expected from the theory, indicating that once the network is sufficiently strained, it largely behaves like the cross-linked semiflexible polymer model.

To test this hypothesis, we quantify the network response beyond the critical region, specifically at the gel rupture point γ_r. In the cross-linked semiflexible network model, the critical strain γ_c marks the level of deformation required for the gel to start to engage the cross-links. For relatively weak cross-links, as we propose for collagen gels, network rupture is likely to be initiated by the breakage of inter-fiber junctions. Therefore, the concentration dependence of $\gamma_c \sim c^{-2/5}$ directly translates to γ_r. Indeed, we find that the strain at which the network ruptures scales with collagen concentration as $\gamma_r \sim c^{-0.4}$, as shown in Figure 2.10(C). This agreement with the predicted concentration dependence further reinforces our argument that, following non-affine network rearrangements at intermediate γ, the network deforms in a more affine manner according to the cross-linked semiflexible polymer model. Furthermore, the finding that the nonlinearity and network rupture are triggered by independent mechanisms, characterized by τ_c and γ_r, respectively, provides an explanation for the observation that some biopolymer networks exhibit strain-stiffening, while some others do not. Even a variation in the polymer and cross-linker concentration in the same biopolymer network can influence whether the network will strain stiffen, as shown in Figure 2.11.

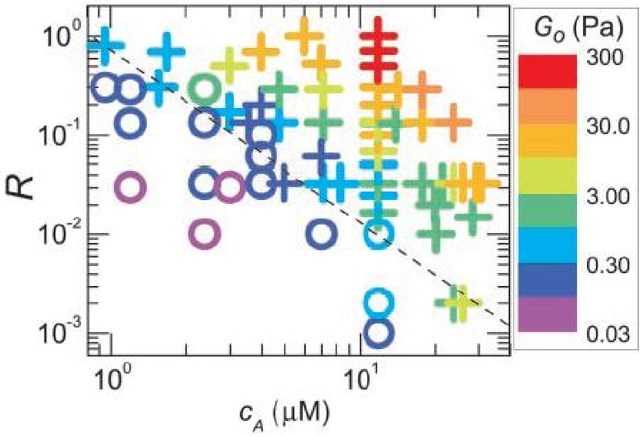

Figure 2.11: The influence of actin concentration c_A and cross-link density on the strain-stiffening behavior of cross-linked actin networks. R denotes the ratio between the cross-linker (scruin) concentration and c_A. The colors indicate the range of the small strain stiffness G_0, as shown in the legend. The symbols differentiate networks that stiffen (+) from those that do not (○). Adapted with permission from [98].

For collagen gels tested in this study, strain-stiffening is not always observed in the higher range of collagen concentrations tested; see the results for gels at c = 7.5 mg/ml. From a microstructural perspective, it is conceivable for a network to achieve γ_r earlier than τ_c, especially when the polymer concentration is very high or very low. To check whether the independent trigger mechanisms are responsible for this behavior, we extrapolate the scaling relation in Figure 2.10(B) for c = 7.5 mg/ml and estimate that τ_c ~ 45 Pa. Experimentally, the strain needed to reach this amount of stress is ~ 0.5, which is $\gtrsim \gamma_c \sim 0.45$ as extrapolated from Figure 2.10(C), confirming our speculation.

2.3.5 Mechanics of collagen network rearrangements

To further investigate the dynamics of the weak cross-links in collagen networks, next we look at the mechanics using modified shear measurement protocols. In particular, we vary γ cyclically, first within the linear viscoelastic regime, then up to network stiffening, according to the protocol illustrated in Figure 2.12(A). The network response exhibits cyclic softening, as shown in Figure 2.12(B), and is highly reminiscent of the classic Mullins effect [99] originally used to describe rubber-like materials. When the shear deformation does not exceed the critical transition to the network stiffening regime, the network can almost fully recover its mechanical behavior, as observed by comparing the paths in Steps 1 and 2 in Figure 2.12(B) and Figure 2.12(C). When the network is strained up to the point where stiffening already occurs, however, there are significant drops in both τ and G' in Step 4, as compared to those in Step 3. These drops suggest that the network has been irreversibly remodeled, possibly through rearrangement of fibers and alteration of cross-linking points, and the resulting network is more compliant to the larger applied level of strains. Interestingly, in both Steps 2 and 4, as γ is gradually decreased, G' increases in a fashion similar to how G' decreases with increasing γ in Steps 1 and 3. After the two cycles, the network exhibits the normal, expected behavior again when deformed to large strains, in Step 5.

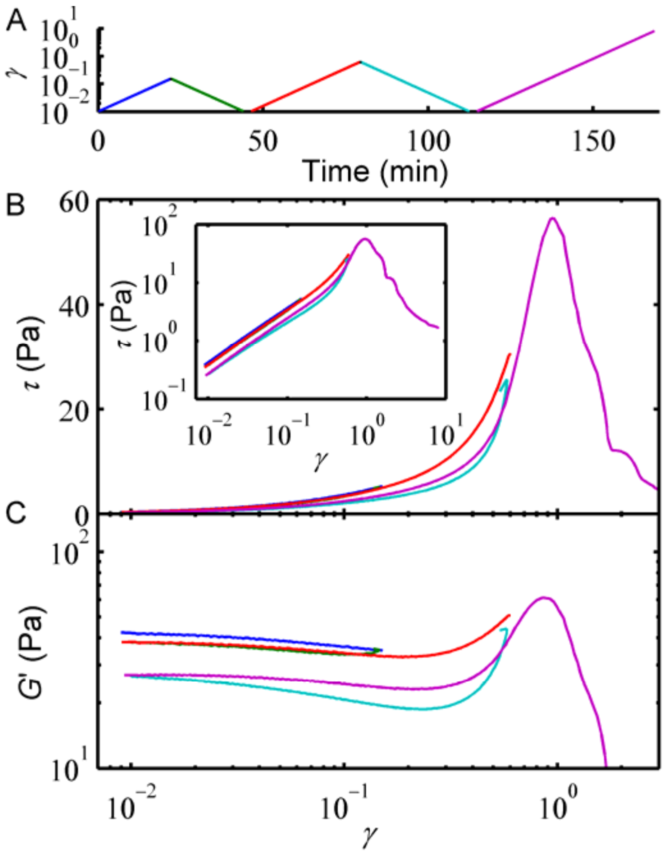

Figure 2.12: Cyclic softening and reversibility of collagen networks. Collagen network with c = 3.5 mg/ml is sheared following the protocol in (A). In the first cycle (Steps 1 and 2), γ is gradually varied between 1% and 15%, within the linear viscoelastic regime of the network. In the second cycle (Steps 3 and 4), γ is varied in the range of 1% and 60%, which includes network stiffening. In Step 5, γ is increased until beyond network rupture. The rate of strain increase and decrease is fixed in logarithmic scale. The network stress and stiffness are shown in (B) and (C) respectively. The stress τ is reminiscent of the classic Mullins effect for cyclic softening, and is shown in log scale in the inset of (B) to make the low strain response clearer. All measurements are done at fixed frequency ω = 1 rad/s.

To capture the transient effect of the network rearrangement during shear deformation, we also modify the protocol in Figure 2.12(A) and include two steps where γ is maintained at 7%, following the procedure in Figure 2.13(A). Indeed, the network response shows time dependence, as shown in Figure 2.13(B). Specifically, the evolution of $G'(t)$ shows the same power law behavior $G'(t) \sim t^{\alpha}$ with $\alpha \approx 0.025$, both when $G'(t)$ decreases with time in Step 2 and when it increases with time in Step 5. Interestingly, in Step 5, $G'(t)$ seems to approach the end point of $G'(t)$ in Step 2. This suggests dynamic processes taking place in the two steps that result in G' approaching a steady state value at a particular γ. It is worth noting that, since the scaling exponent α is very low, the time scales at which steady state is reached is likely to be minutes or hours, which is much larger than the time scales corresponding to the range of frequencies accessible in most rheological measurements, but is the time scales relevant for many biological processes, such as cell migration.

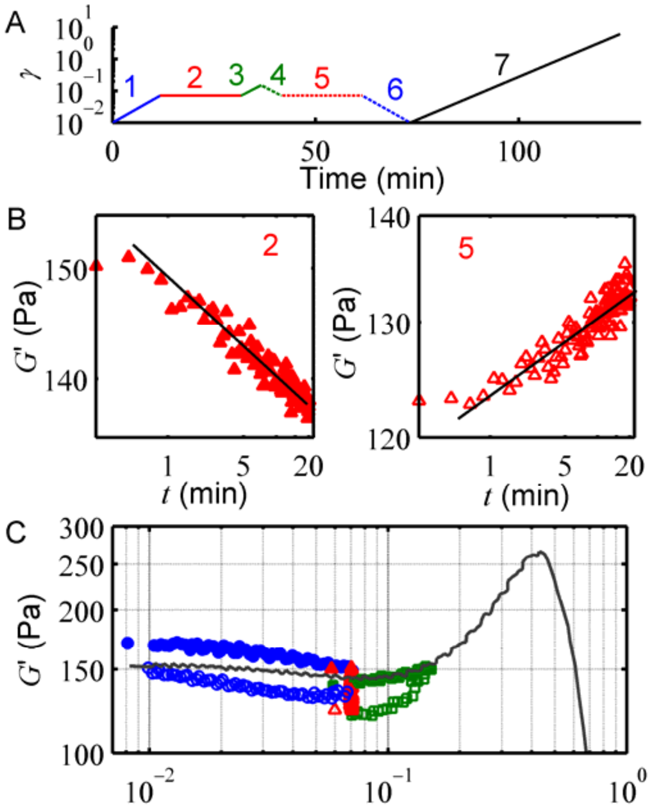

Figure 2.13: Strain-dependent network stiffness is a transient phenomenon. The cyclic shearing protocol in Figure 2.12 is extended for collagen network with $c = 3.5$ mg/ml at 37°C, as described in (A). Specifically, two additional Steps (2 and 5) are added, where the oscillation amplitude γ is then maintained at 7% for ~20 mins, while the stress relaxation is monitored. The resulting relaxation modulus $G'(t)$ for Steps 2 and 5 is plotted in log-log scale against time in (B). $G'(t)$ evolves as $\sim t^{0.025}$ in both the decrease in Step 2 and the increase in Step 5, as shown by the solid line. Equally interesting is the observation that the time-dependent $G'(t)$ value at the end of Step 5 is close to that at the end of Step 2, suggesting a dynamic process with an 'equilibrium' $G'(\gamma)$ value. The overall variation of network stiffness is shown in (C) (increasing γ: filled symbols, decreasing γ: open symbols). The full strain sweep measurement is then done in Step 7 on the same sample, where the result is similar to our previous observation in Figure 2.12.

Taken together, the persistent trend of network softening at small strains and the cyclic softening reported in Figure 2.12 show partial network reversibility, while the transient effect shown in Figure 2.13 reveals the time dependence of the network rearrangement. Network rearrangement in the form of fiber realignment, bending, and buckling has been observed to accompany network deformation [67,68,100,101]. This microstructural rearrangement inherently produces nonaffine deformations that can lead to the breakdown of the MacKintosh model's prediction as we saw earlier. It can also explain the partial reversibility of the network mechanics at small strains. However, it offers no explanations regarding both the agreement with the semiflexible network theory at large strains and the time dependence of the rearrangement. Our earlier argument that the existence of weak and dynamic cross-links can explain the former observation is in fact also applicable to explain the latter. This transient cross-link turnover causes plastic deformation that modifies local network architecture as the network deforms. The findings that the same scaling exponent is found in both Steps 2 and 5 and that there seems to be an equilibrium network state, as depicted in Figure 2.13, further reinforce the argument that global network rearrangements including cross-link turnover are responsible for the strain-dependent mechanical behavior observed in collagen networks.

2.4 Summary

In conclusion, we propose that the mechanics of uncross-linked collagen networks can be described by modeling the gel as a weakly cross-linked semiflexible polymer network. This is reflected in the three regimes of the strain-dependent viscoelasticity of collagen networks. At low strains, the network slightly weakens with increasing strain as a result of network rearrangements, which include cross-link turnover. The overall elasticity of the network in this regime is still largely reversible. As the network becomes more stressed, nonlinear stiffening starts to kick in when the critical stress τ_c is reached. At this intermediate strain level, the network irreversibly stiffens with increasing strain. The network ruptures when the strain reaches the rupture strain γ_r. The strain stiffening regime may not occur when γ_r is achieved earlier than τ_c, which may explain why strain stiffening is sometimes not observed in biopolymer networks. These results highlight the importance of short-scale network architecture in determining the overall mechanics of collagen networks, which will be discussed in further detail in Chapter 3 and Chapter 4.

Chapter 3: Mechanics of Semiflexible Polymer Networks

3.1 Introduction

The mechanical versatility of biological tissues and cells play a central role in various physiological and biological functions at different scales, from cellular level to organ level. The materials providing intra- and extra-cellular mechanical support for the cells are defined by cross-linked networks of semiflexible fibers. Inside the cell, a cytoskeletal network of intracellular proteins consisting of actin filaments, microtubules, intermediate filaments, and other proteins stabilizes cell structure, transmit environmental cues, both mechanical and chemical, and modulates numerous cell functions, such as cell morphology, division, motility, and even apoptosis [102-104]. Outside the cell, a network of proteins, with collagen as the primary backbone, forms the extracellular matrix, which can mediate mechanical signals to and from the cell. As discussed in Chapter 2, one of the hallmarks of these networks is their ability to stiffen at increasing strain, as depicted in Figure 3.1, thereby enhancing tissue integrity and producing the characteristic nonlinear stress-strain curve observed in soft tissues [49]. The origin of this nonlinearity is not fully understood, partly due to the complexity and the interconnectedness of the relevant physical features, which are not always resolvable experimentally. For this reason, theoretical and computational studies have been invaluable in providing insights on the structure-property relation of semiflexible networks [105].

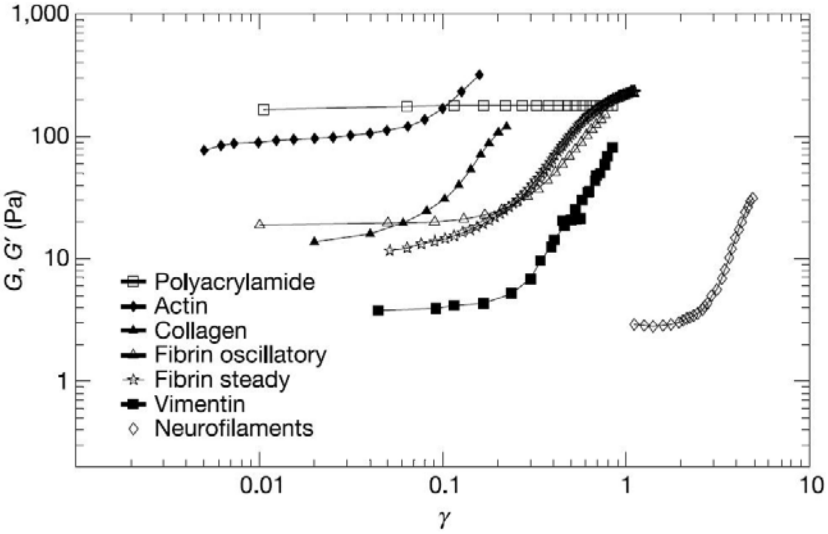

Figure 3.1: Strain stiffening properties of various biopolymer networks. Data shown are the storage modulus G' at ω = 10 rad/s, plotted as a function of shear strain γ, measured using oscillatory rheometry (*cf.* Chapter 2). Adapted with permission from [50], where the detailed measurement details can be found.

Theoretical studies have attempted to trace the nonlinear bulk elasticity to the nonlinear force-extension relation of single filaments by assuming affine network deformation [50,94]. In this case, entropy determines the network elasticity at small strains, while enthalpy plays an increasingly bigger role at larger strains. However, it has been argued that network rearrangement and a transition from bending-dominated to stretch-dominated deformation can cause nonlinearity in the network response even without appealing to the nonlinear force-extension relation of single chains [101,106,107]. Further, numerical studies on two-dimensional (2D) [51,107-110] and three-dimensional (3D) [106] random networks show evidence of nonaffine behavior. In particular, the degree of network affinity has been shown to be a function of strain [106,107] as well as characteristic length scales of the network, such as the average distance between cross-links l_c, fiber length L and persistence length l_p [109].

A key aspect of network mechanics that has not received attention is the length scale of material homogeneity. At the macroscopic level, where the assumption of homogeneity may not be too great an oversimplification, the network elasticity has been theoretically explained and predicted [50,94] as well as experimentally validated [98,111], typically in terms of polymer concentration c_m and cross-linker concentration c_{cl}. However, biological materials are invariably heterogeneous at small scales (*e.g.*, ~ μm, relevant to cells). Not surprisingly, therefore, it has been recently realized that specific network architectures, such as the number of filaments incident to a branch point [112,113] and the number of cross-links per filament [114], play an important role in governing elasticity, especially in 3D networks. Such quantitative analyses of network microstructure are hampered experimentally by a lack of understanding of how networks self-assemble and cross-link. This results in uncertainties on how macroscopic quantities, such as c_m and c_{cl}, translate to the actual network architecture at short length scales. Understanding network mechanics and architecture at such small scale is extremely important for cell studies, not only to give insights into the cytoskeletal mechanical behavior, but also because cells interact with the surrounding extracellular environment through small (micro- to nano-) scale interactions [115].

In view of these, it is crucial to base the analysis on a realistic model of semiflexible network for which the microstructure can be quantitatively parameterized. Therefore, we develop a model of discrete 3D semiflexible networks with tunable fiber dimensions and show that the nonlinear mechanics can be explained exclusively through structural features. Specifically, two parameters representing cross-link and fiber entanglement are shown to govern network stiffness at multiple strain levels and length scales relevant to the cell; thus nonlinearity is linked directly to structural features. In addition, our approach can accommodate the different deformation mechanisms and experimental findings available in the literature.

3.2 Methods

3.2.1 Network model

To model the fibers in the network, we modified the standard “shish-kebab model” typically used to represent coarse-grained polymer and worm-like chains [116]. Each fiber was discretized as an array of beads of diameter d, with neighboring beads situated at an equilibrium distance of $d/2$, rather than d, from each other. We find that this helps in simulating fiber-fiber interaction stably, especially at large strains. The total number of beads per fiber was therefore determined by the initial fiber contour length, L, as $2L/d-1$. The beads were connected by a harmonic stretching potential

$$U_s = \frac{1}{2}k_s\left(r-\frac{d}{2}\right)^2, \tag{3.1}$$

where r is the distance between beads, and the fiber semiflexibility was implemented using a harmonic bending potential

$$U_b = \frac{1}{2}k_b\left(\theta-\pi\right)^2. \tag{3.2}$$

The respective stretching constant k_s and bending constant k_b can be directly related to physically measurable quantities such as the fiber's Young's modulus E and persistence length l_p as

$$k_s = \frac{EA_f}{d}, \tag{3.3}$$

where A_f is the fiber cross-sectional area and

$$k_b = 0.31\left(\frac{2l_p}{d} - \frac{2}{3} - \frac{1}{3+9\left(16/\pi^2-1\right)\left(2l_p/d-1\right)}\right). \tag{3.4}$$

Eq. (3.4) is a modified approximation for the discrete worm-like chain model [117] that we have empirically tested independently. The harmonic functional form of U_s and U_b is deliberately chosen not only because of its simplicity, but also to make the results directly comparable to previous studies [106,107,109].

We also model two types of interactions between different fibers: entanglement and cross-link. The physical entanglement between non-penetrable fibers was modeled with a one-sided repulsive potential

$$U_i = \begin{cases} \frac{1}{2}k_i\left(d-r\right)^2, & r \le d \\ 0 & , r > d \end{cases} \tag{3.5}$$

where r is the distance between non-neighboring beads. The interaction constant k_i determines the fiber 'softness'. Although the functional form of U_i can in principle be extracted from experimental data (*e.g.*, from fiber indentation studies), we found that the choice of the function does not significantly affect the overall network response at physiological fiber volume fractions tested in this study. Here, we employ U_i simply to prevent fiber-fiber penetration. Cross-linking between different fibers was represented by a harmonic cross-link potential

$$U_{cl} = \frac{1}{2} k_{cl} \left(r - \delta_0 \right)^2 . \tag{3.6}$$

Cross-link length δ_0 and compliance k_{cl} can influence the nonlinear behavior of the network [86,98,118,119] and deserve a full exploration on their own. Here, we generically set $k_{cl} \equiv k_s$ and $r_0 \equiv d$ to simulate permanent, freely rotating, chemically strong cross-links.

We summarize the fiber model and interaction in Figure 3.2. The key parameters useful in repeating the simulations can be found in Table 1. The fiber model employed here mimics cylindrical topology while maintaining short-scale bending flexibility, without excessive computational burden. Moreover, the resulting network allows fairly smooth 3D steric entanglement, which cannot be simulated in 2D simulations.

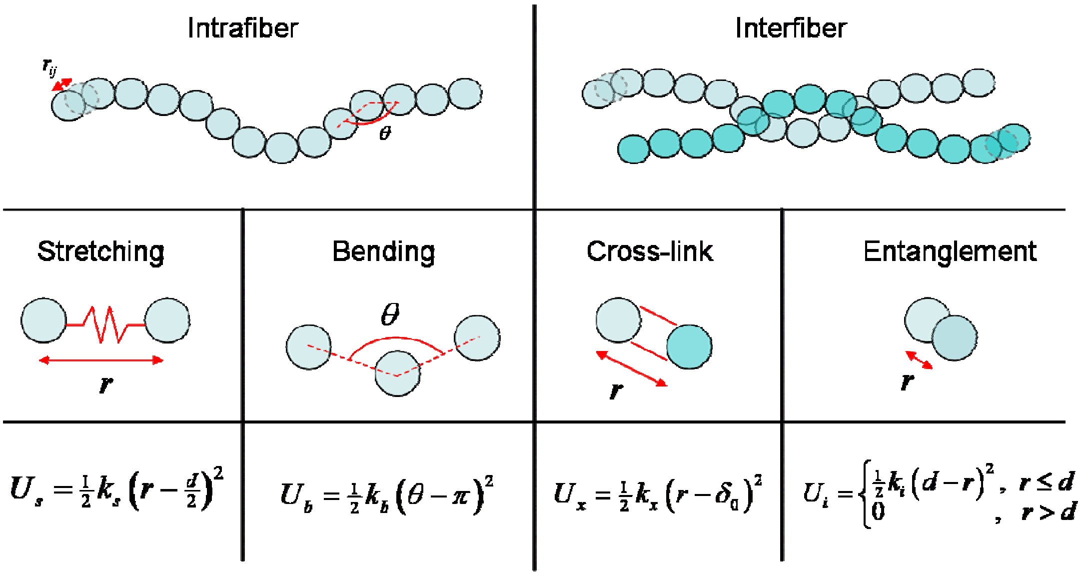

Figure 3.2: Summary of fiber model and interaction.

Table 1: List of independent variable parameters for simulating semiflexible polymer network model

Parameter	Value	Typical experimental value
L	5 μm	Actin, collagen ~ 2–8 μm.
d	0.25 μm	Collagen ~ 0.03–0.5 μm.
l_p	5 μm	Actin, collagen ~ 1–20 μm.
W	6–8 μm	Short length scale. MR $\gtrsim$ 250 μm.
δ_0	d	Depends on cross-linker properties.
δ_w	d	Depends on experimental setup.
δ_{cl}	0–1.5 d	Depends on polymer self-assembly.
E	50 MPa	Collagen ~ 50 MPa
k_i	k_s	Depends on fiber interaction properties.
k_{cl}	k_s	Depends on cross-linker properties.

3.2.2 Network generation and deformation

The networks were generated by initially placing N straight fibers with random position and orientation in a periodic cubic unit cell of size $W \times W \times W$, with N determined from the given polymer concentration c_m or volume fraction Φ. A snapshot of this initial state is shown in Figure 3.3(A). Fibers that traverse the top and bottom walls—walls parallel to the shear plane—were shifted down and up, respectively, to ensure that the walls are non-penetrable and make the networks simulate experimental conditions. Cross-links were assigned when two beads from different fibers were within a threshold distance δ_{cl}, as illustrated in Figure 3.3(B). To avoid double counting and keep the simulation stable, when there was more than one bead within δ_{cl} from another bead, only the pair with the shortest distance was assigned as cross-links. This procedure has an advantage over previous numerical studies [106,107,109], as cross-link density can be varied independently of c_m by varying δ_{cl}. Before any mechanical test were performed, these highly stressed networks were energy-minimized based on the total potential $U = U_s + U_b + U_{cl} + U_i$. While there may be some amount of mechanical prestress that remains even after this relaxation step, we expect the effect to be completely random and comparable to that in standard mechanical experiments [86]. The resulting network architecture, as shown in Figure 3.3(C), mimics *in vitro* self-assembled biopolymer gels [111] that have been used to explain cell mechanical properties [120].

To deform the networks realistically, we defined top and bottom wall beads as the beads located within δ_w from the top and bottom walls, respectively. During the network straining, the bottom wall beads were fixed and the top wall beads were moved according to the imposed shear strain γ. Only one bead per fiber was allowed to be assigned as wall bead. The force needed to keep the wall beads in place during the straining was then used to calculate the network stress τ. Figure 3.3(D) shows the network in Figure 3.3(C) under a strain of $\gamma = 0.5$, and a comparison reveals that a global network rearrangement has taken place through fiber reorientations and translocation, consistent with previous 2D as well as 3D studies [106,107].

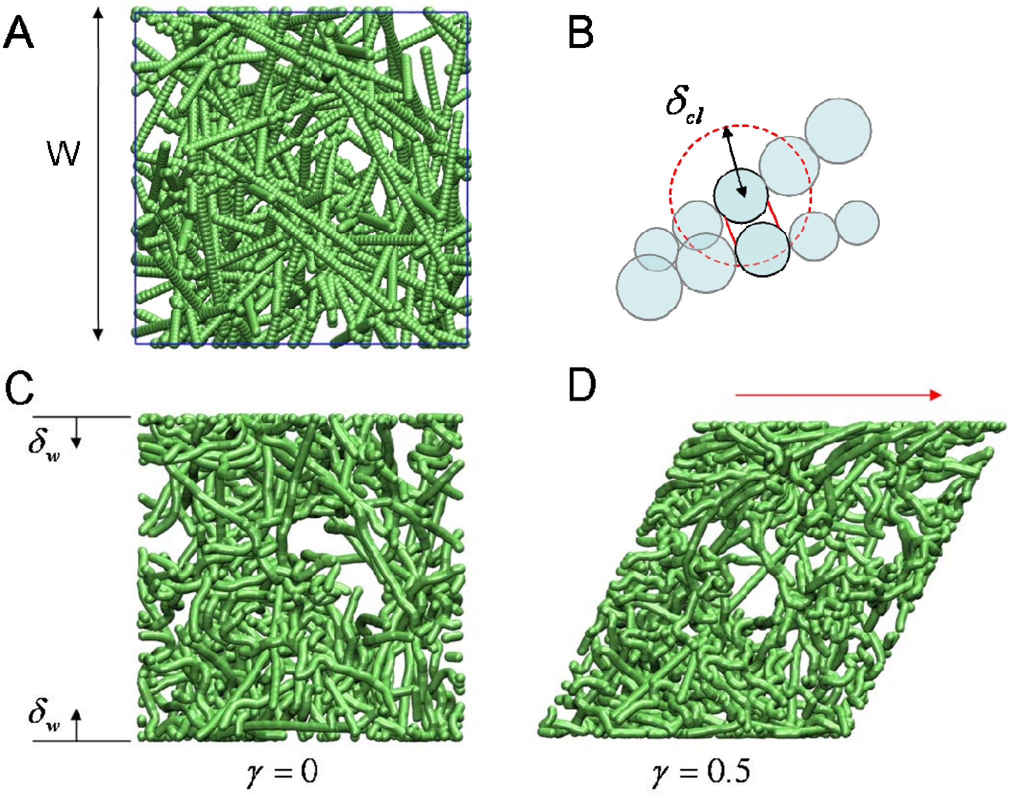

Figure 3.3: Illustration of semiflexible polymer network model. The network initially consists of straight rods with random positions and orientations (A). The beads making up the rods can be visualized. Cross-links are assigned when beads from different fibers are located within δ_{cl} from each other (B). The network is then energy-minimized based on the total potential U, resulting in relaxed network with local heterogeneities (C). The effective shapes of the cylindrical fibers are shown. During the shear deformation of the network, beads within δ_w from the bottom wall are fixed, while beads within δ_w from the top wall are moved according to the imposed shear strain γ. An example of strained network ($\gamma = 0.5$) is shown in (D). The arrow indicates the direction of shear strain application. The sample network shown here consists of fibers with aspect ratio $L/d = 20$, and is cross-linked with $\delta_{cl}/d = 0.7$.

3.3 Results and Discussion

We study the nonlinear stiffening of the networks by incrementally imposing the strain γ up to ~ 100%. Shear stress τ is obtained from the force needed to deform the network by γ. Figure 3.4 shows the complete stress-strain response for typical networks with different volume fractions Φ = 5.6%, 7.4%, and 9.3%. At small γ, the network responds linearly, with stiffness comparable to values measured for biopolymer networks [1,12]. As γ increases, the stiffness gradually increases, introducing nonlinearity in the response. In general, the overall response can be characterized by the small-strain stiffness $G_0 = \left[d\tau/d\gamma\right]\big|_{\gamma\to 0}$, the critical strain γ_c corresponding to the onset of nonlinearity, and the instantaneous large-strain modulus $G_L = \left[d\tau/d\gamma\right]\big|_{\gamma=3\gamma_c}$, as indicated in Figure 3.4. The choice of $\gamma = 3\gamma_c$ is arbitrary but guarantees that G_L is obtained well beyond the onset of stiffening. The response is highly sensitive to variations in the network physical properties, such as Φ and cross-link density (even for fixed Φ). In the following, we demonstrate how these variations can be described in terms of characteristic network structure parameters.

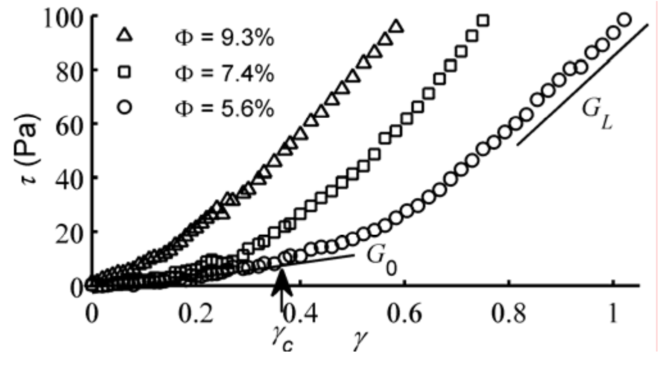

Figure 3.4: Typical overall response of cross-linked semiflexible polymer networks. Shear stress τ is shown as a function of shear strain γ for networks of different volume fractions (Δ, $\Phi = 9.3\%$; □, $\Phi = 7.4\%$; ○, $\Phi = 5.6\%$). Three distinct regimes can be observed: low network stiffness G_0 at small strains, high network stiffness G_L at large strains, and the nonlinear transition between the two strain regimes, starting at the critical strain γ_c.

3.3.1 Network structural parameters

The role of network structure on the elasticity has been extensively studied, both theoretically and experimentally, especially at small strains. As mentioned earlier in

Section 2.3, the small-strain stiffness G_0 is typically reported to vary as $G_0 \sim c_m^x R^y$, where $R = c_{cl}/c_m$ and the exponents x and y vary with biopolymer type as well as properties and strength of cross-linkers [94,101,111,119,121,122]. While c_m and R are convenient to measure experimentally and reflect the overall properties of the network, these are macroscopic quantities with no direct link to the actual network architecture. Therefore, without proper accounting for the exact mechanism of biopolymer self-assembly and cross-linking, these quantities can in fact provide misleading information at small length scales. To describe the actual network structure at short scales more faithfully, we directly quantify the network structure in terms of two parameters: the number of entanglements per fiber, R_e, and the number of cross-links per fiber, R_{cl}. The network connectivity parameter R_{cl} can be experimentally estimated [114] and, here, can be adjusted arbitrarily through δ_{cl} and Φ. Figure 3.5 shows the relation between the actual R_{cl} obtained from network generation and the input values of δ_{cl} and Φ, which is proportional to c_m. The relatively large variation of R_{cl}, as indicated by the error bars in Figure 3.5, underlines the effects and importance of accounting for local heterogeneity often encountered in biopolymer networks [18,19]. This realistic sample-to-sample variation makes it possible, for example, for a network of lower c_m to have larger degree of connectivity than one with higher c_m. On average, however, the network structural parameter R_{cl} can be finely tuned by the two physical input parameters, δ_{cl} and Φ, as seen in the inset of Figure 3.5.

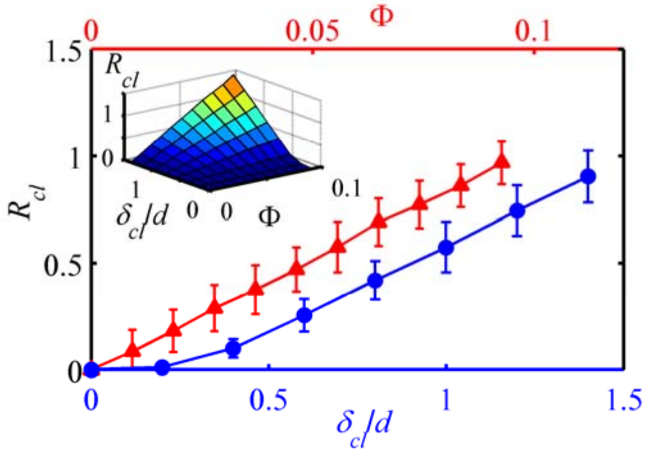

Figure 3.5: The relation of input δ_{cl} and Φ values to output R_{cl} of the network [●, $R_{cl}\left(\delta_{cl}/d\right)$ for fixed $\Phi = 5.6\%$; ▲, $R_{cl}\left(\Phi\right)$ for fixed $\delta_{cl} = d$]. The error bars are based on 200 different random network realizations. The mean of $R_{cl}\left(\Phi,\delta_{cl}\right)$ is shown in the inset.

3.3.2 Length-scale-dependent network mechanics at small strain

We start the analysis of network mechanics by looking at the network behavior at small γ. We find that all G_0's from networks generated with different Φ and δ_{cl} fall into a master relation $G_0 \sim R_{cl}^{0.8}$, as shown in Figure 3.6(a) (although the correlation coefficient R^2 is only 0.59). It is important to note that here we simply quantify the *resulting* network structure through R_{cl} without distinguishing the *cause*, which can jointly arise from fiber and cross-link densities. This contrasts previous predictions based on scaling arguments that have not, however, accounted for the exact mechanism of biopolymer self-assembly and cross-linking [94,98,111]. Therefore, our finding not only confirms the predicted role of macro-scale network connectivity [94], but also hints at a more universal mechanism of network deformation based principally on structural properties, which calls for deeper investigations on the nontrivial relation between the macroscopic inputs c_m and R and the actual network structure, as quantified through R_{cl} here.

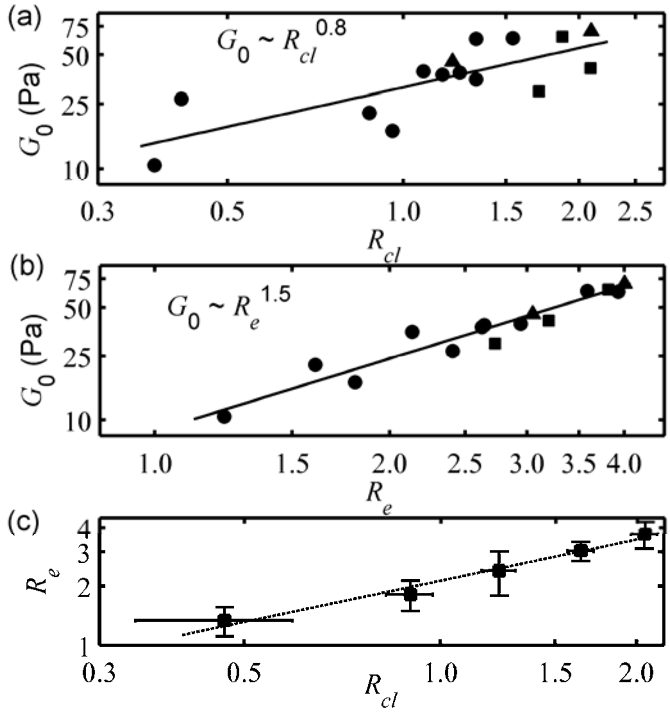

Figure 3.6: Influence of network structure on the network response at small strain. Small-strain stiffness G_0 is plotted in (a) against R_{cl} and in (b) against R_e. The data are obtained from networks with fixed fiber dimensions but various Φ (▲, $\Phi = 9.3\%$; ■, $\Phi = 7.4\%$; ●, $\Phi = 5.6\%$) and cross-link densities, $0.5 < \delta_{cl}/d < 1.5$, resulting in networks with varying connectivity. The relation between the averaged macroscopic quantity R_{cl} and the averaged microscopic quantity R_e is shown in (c). The dashed line is a guide for the eye.

The short-scale interaction between network fibers is characterized by entanglements, whose effect is subtler and weaker than cross-links [94]. To study this local steric interaction more closely, we also quantify the number of entanglements per fiber, R_e, for all the networks generated. Remarkably, G_0 shows excellent correlation with R_e, scaling as $G_0 \sim R_e^{1.5}$, as shown in Figure 3.6(b) (R^2 = 0.92). Physically, the strong correlation between G_0 and R_e implies that, for $\gamma \to 0$, entanglements play an important role in governing the stiffness at short length scales, inherently leading to nonaffine deformations, although it has been suggested that, at larger length scales, the macroscopic mechanics may be related simply to cross-link density, as discussed earlier. Using our approach, the relative dependence of structural heterogeneity on length scale can be examined by sampling a number of independently generated networks (*cf.* law of large numbers). Indeed, the *averaged* R_{cl} and R_e show a strong correlation [see Figure 3.6(c)]. This correlation suggests that network mechanics is described by two different structural parameters on different length scales: R_{cl} (cross-links) for systems of large sizes where structural heterogeneity is negligible and R_e (entanglements) for smaller systems where the local structural feature is vital to network deformation. As such, while macroscopic measurements provide overall, averaged properties, a more 'local', microscale measurement is needed for further insights into the network mechanics.

3.3.3 Nonlinear strain-dependent network mechanics

We now shift our focus to the network nonlinear behavior. The strain required to trigger stiffening, γ_c, is known to indicate the transition in the underlying mechanics, *e.g.*, bending- to stretch-dominated [51,68,94,123]. Our results on the role of network structure on γ_c show that $\gamma_c \sim R_{cl}^{-0.6}$, as shown in Figure 3.7 (which is reminiscent of a relation found previously for F-actin [111], albeit in terms of $R = c_{cl}/c_m$). This scaling relation and network visualization confirm a mechanism where the deformation starts to engage cross-links and involve individual fiber stretching, thus giving rise to nonlinearity in the response.[2] In fact, this mechanism provides an explanation for previous observations reporting a general transition from a bending-dominated regime at small γ to a more stretch-dominated regime at large γ [106,107]. Meanwhile, further analysis reveals that, as γ increases, the correlation between stiffness and R_e becomes increasingly poorer. Taken together, these suggest that the distinct deformation mechanisms at different strain levels are linked to the network structural parameters. At small γ, the response is governed by weak interactions (entanglements), which manifest in bending-dominated, nonaffine deformation, while at larger γ, the response is governed by strong interactions (cross-links), which manifest in an increasingly stretch-dominated, affine deformation.

---

[2] We note that, conventionally, power laws are obtained over several orders of magnitude of the independent variable. However, this is not always feasible in biological systems, in view of the restricted ranges of the parameters involved. This is reflected in the limitations imposed by the size of the system we consider here. Nevertheless, the physical insights obtained from the analysis remain valid.

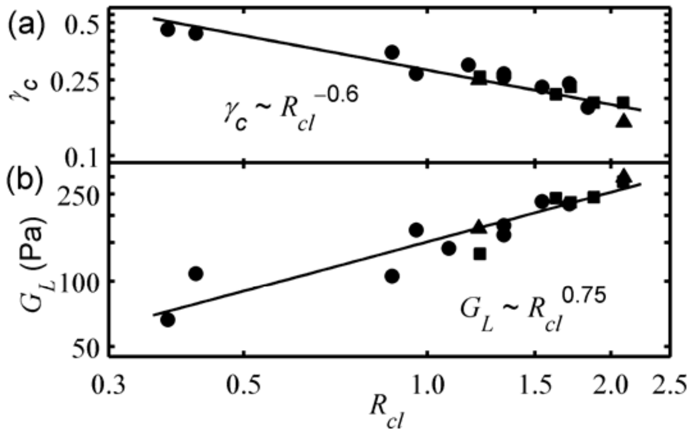

Figure 3.7: Influence of network structure on the network response at intermediate and large strains. Both the critical strain γ_c and the large-strain stiffness G_L, shown in (a) and (b) respectively, exhibit scaling relations with R_{cl} at all volume fractions tested (▲, $\Phi = 9.3\%$; ■, $\Phi = 7.4\%$; ●, $\Phi = 5.6\%$), demonstrating the importance of network structure parameters even beyond the linear elastic regime shown in Figure 3.6.

To test the above conclusively, we examine whether R_{cl} is important in determining the mechanics even at large strains $\gamma > \gamma_c$. We find that this is indeed the case, with $G_L \sim R_{cl}^{0.75}$, as shown in Figure 3.7. This dependence on R_{cl} provides direct evidence that, for $\gamma > \gamma_c$, the deformation is not just governed by the stretching of individual fibers, but is also determined by the response mediated through the cross-links. This finding therefore corroborates the argument that the nonlinear stiffening can be explained in terms of the continual network rearrangement, in addition to any nonlinear force-extension behavior of individual fibers [98,101,107]. In addition, in contrast to the response for small γ, where the cross-links dominate at large length scales as noted in Section 3.3.2, the response at large γ is determined by cross-links at large as well as short length scales. This suggests that heterogeneity plays increasingly smaller roles at larger γ, which may be responsible for the increasing network affinity.

3.3.4 Network deformation mechanism

As an independent measure of the network deformation mechanism, we also analyze the affinity of the network deformation. The affinity (or nonaffinity) of deformation is typically measured by looking at the difference in length, angle, or vector position between the observed deformation and that predicted for a purely affine deformation, as illustrated in Figure 3.8, and can be measured in a number of ways [124]. Here, we use the dimensionless nonaffinity parameter A, which is similarly used in a previous 3D network study [106], as defined by

$$A = \left\langle \frac{\left|\delta \mathbf{u}_{cl} - \delta \mathbf{u}_{cl}^{aff}\right|^2}{\left|\delta \mathbf{u}_{cl}^{aff}\right|^2} \right\rangle, \tag{3.7}$$

to monitor the deviation in the cross-link displacement $\delta \mathbf{u}_{cl}$ from the expected affine displacement $\delta \mathbf{u}_{cl}^{aff}$ upon an increment of strain $\delta\gamma$. A vanishing A value therefore implies completely affine deformation. Shown in Figure 3.9 is a typical evolution of A with γ for $\Phi = 5.6\%$. Consistent with reported data [106,107], the deformation is nonaffine ($A > 0$), but with an increasing degree of affinity ($A \to 0$) as γ increases, confirming our earlier remark.

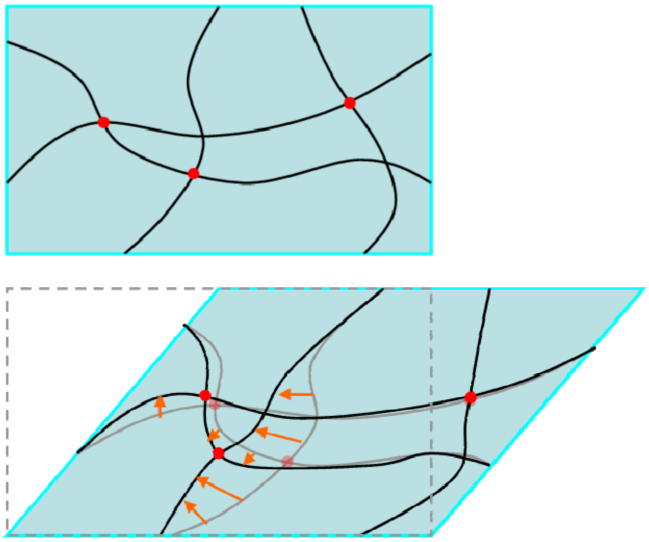

Figure 3.8: Illustration of nonaffine deformation. The initial configurations of the fibers are shown in the top panel, with the red dots indication the location of cross-links. After shear deformation, the final configurations of the fibers (black lines) and cross-link locations differ from the expected configurations were the deformation affine (gray lines and dots).

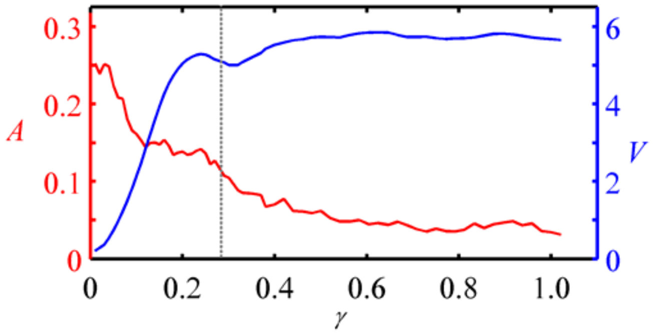

Figure 3.9: Quantification of network affinity and rearrangement at different strain levels. The dimensionless parameters for nonaffinity A, as defined in [106], and cumulative rearrangement V vary with γ. A measures the deviation of the actual position vector of the cross-links from the expected affine position upon strain increment $\delta\gamma$, while V monitors the absolute deviation from $\mathbf{u}^{aff}(\gamma)$ of all beads in the network up to γ. The vertical dashed line indicates γ_c.

We also directly quantify the extent of network rearrangement by tracking the trajectories of all the fiber beads during the straining and defining a network rearrangement parameter V as

$$V = \left\langle \frac{\left|\mathbf{u} - \mathbf{u}^{aff}\right|^2}{d^2} \right\rangle, \tag{3.8}$$

denoting the cumulative nonaffine rearrangement that has occurred. Figure 3.9 shows that the amount of rearrangement increases continually with γ, with a significant portion occurring even before the network stiffening, as signified by the steeper slope $dV/d\gamma$ at $\gamma \lesssim \gamma_c$.

3.4 Conclusions

In this chapter, we demonstrate that (i) structural properties, namely network connectivity and physical entanglements, lie at the heart of the nonlinear mechanics of 3D networks, (ii) the contributions from these two parameters define the dominant deformation mechanism, *e.g.*, affine vs. non-affine, and (iii) the crossover between the two is governed both by length scale of observation and strain level. For $\gamma < \gamma_c$ the overall deformation is dominated by short-scale fiber mechanics, and the network stiffness is governed by steric interaction at short length scales and by cross-links at larger length scales. But once the network is sufficiently strained, reorganization causes the effects of local heterogeneity to diminish and be replaced by a more homogeneous response. Biological networks may thus take advantage of the heterogeneity at small γ to accommodate various physiological functions with less hindrance, such as nutrient and molecule transport, while retaining the ability to accurately control large-strain responses through active cross-linkers for the benefit of network integrity [125].

The distinct deformation mechanisms at different length scales provided by the model employed here underscores the role of 3D steric interactions between fibers and may not be accessible through previous models. Our simple model also allows easy adaptation fashioned to diverse lines of exploration. For example, future work can be aimed to elucidate the individual roles of fiber properties (*e.g.*, d, L, l_p, and E) and cross-linker properties (*e.g.*, k_{cl} and δ_0), which will enable more quantitative comparison to other experimental and theoretical works [51,111,114,126]. These properties, or the distribution thereof [109,127,128], are likely to affect the structural network response by varying the length-scale difference between the heterogeneous and the homogeneous scales.

Chapter 4: Microrheology of Collagen Networks

4.1 Introduction

As established in Chapter 3, short-scale mechanics and material heterogeneity play a crucial role in the overall elasticity of semiflexible polymer networks, including collagen. A more detailed understanding of the network mechanics at short scale will therefore be valuable not only in interpreting physiological cell behavior, but also in igniting new design strategies for engineered (biocompatible) polymeric materials. Consequently, while macroscopic measurements, such as the rheological measurements we report in Chapter 2, provide overall, averaged properties of the material, a reliable microscale diagnostic technique is required and is important for probing network mechanics, especially in the contexts of cell mechanics and behavior.

In view of these, in this chapter we report and discuss the experimental results of mechanical characterization of the same soft matter system as in the previous chapters (collagen networks) at the microscale level, as measured using a microrheological technique, namely, particle tracking microrheology. We start by providing brief background information on microrheology in general and the particle tracking microrheology technique in particular. Subsequently, we discuss the implications of the results obtained and the limitations as well as technical problems that remain to be tackled, which serve as motivations for the new microrheological technique that we will present in Chapter 5 and Chapter 6.

4.2 Microrheology

Microrheology, a branch of rheology, has emerged as a class of mechanical characterization techniques that probe material response in the micrometer length scale with microliter sample volumes. The smaller length scales come about as a result of the ability to use smaller mechanical probes to deform the sample, usually in the form of microspheres. This is particularly advantageous when dealing with precious samples, like many biological samples. Typically, microrheology involves tracking the motion of embedded or endogenous particles as markers of sample response, from which the rheological information of the sample is inferred. Broadly, there are two classes of microrheological techniques: those involving active manipulation of probes by local application of stress (“active microrheology”) and those measuring passive probe motion due to thermal or Brownian fluctuations (“passive microrheology”).

In active microrheology, there are two general aspects that require careful attention. The first concerns the method used to actively impose probe motion. This can be done either nonintrusively, *e.g.*, using magnetic or optical tweezers, or by indenting the surface of the sample using atomic force microscopy [129-132]. The mechanical response of the sample can then be quantified from the actual probe displacement as monitored either visually through microscopy or indirectly through measurement of laser deflection. In contrast, in passive microrheology, there is no external field and probe motion is due only to thermal fluctuation. As a result, these fluctuations reflect the exact linear viscoelastic response parameters and their complete frequency dependence. Simple, single observation of these fluctuations can therefore provide rich information about the frequency-dependent mechanical properties of the sample. In practice, this can be done either by directly detecting the thermal motion of individual probes [133-135] or by observing the intensity fluctuation resulting from the multiple scattering of light by an ensemble of probes [136-138]. Extensive and comprehensive discussions on the underlying principles, current states of various microrheological techniques and applications can be found in recent reviews [21,139,140]. Next, we will briefly touch on one particular passive microrheological technique that we will use to characterize collagen networks, namely, particle tracking microrheology (PTM).

Passive microrheology techniques use the Brownian dynamics of embedded or endogenous particles, based purely on thermal energy, to measure the rheology and structure of a material. PTM techniques directly track the thermal movements of the probe particles to do so. The dynamics of particle motions are conveniently quantified in terms of the mean squared displacement (MSD) of individual probes:

$$\left\langle \Delta r^2(\tau) \right\rangle = \left\langle \left(r(t+\tau) - r(t) \right)^2 \right\rangle_t , \tag{4.1}$$

where $r(t)$ is the particle position[3], τ is the time lag, and $\langle \bullet \rangle_t$ indicates averaging over all time t. For microspheres of radius a diffusing in a purely viscous medium,

---

[3] Strictly speaking, particle position should be represented by the vector $\mathbf{r}$ and the MSD should likewise be $\left\langle \Delta \mathbf{r}^2(\tau) \right\rangle$. For simplicity, in this thesis, we assume that the vector position is understood.

the MSD varies linearly with τ and is related to the diffusion coefficient D through the diffusion equation

$$\left\langle \Delta r^2(\tau) \right\rangle = 2nD\tau , \tag{4.2}$$

where n denotes dimensionality. The medium viscosity ν can be obtained using the Stokes-Einstein equation

$$D = \frac{k_B T}{6\pi \nu a} . \tag{4.3}$$

In a viscoelastic medium, however, the particle MSD generally does not have simple linear relation with τ, due to the elastic contribution. A natural way to incorporate the elastic response in the above expressions is by generalizing the standard Stokes-Einstein equation [Eq. (4.3)] with the complex viscosity $\nu^* = \nu' + i\omega\nu''$. The complex shear modulus of the medium, $G^*(\omega) = G'(\omega) + iG''(\omega)$, is then related to ν^* as $G^*(\omega) = i\omega\nu^*(\omega)$.

The Generalized Stokes-Einstein Relation (GSER), relating the probe MSD to the shear modulus of the medium, has been derived to give

$$\left\langle \Delta r^2(\tau) \right\rangle = \frac{d k_B T}{3\pi a s \tilde{G}(s)} , \tag{4.4}$$

where $\tilde{G}(s)$ is the Laplace transform of $G(\omega)$ and s is the Laplace frequency [136]. An equivalent representation of the GSER in terms of the Fourier components can be readily obtained via analytic continuation $s = i\omega$. In practice, however, the discrete time-domain MSD has limited dynamic range, and numerical Laplace or Fourier transform can cause significant errors in the calculation of $G^*(\omega)$, especially near the frequency extremes. An alternative method based on the local power law expansion of $\left\langle \Delta r^2(\tau) \right\rangle$ has been developed to approximate the time-domain MSD and the transforms [141]. The local logarithmic slope of $\left\langle \Delta r^2(\tau) \right\rangle$ is calculated as

$$\alpha(\omega) = \left. \frac{d \ln \left\langle \Delta r^2(\tau) \right\rangle}{d \ln \tau} \right|_{\tau = 1/\omega} \tag{4.5}$$

and describes the local power law exponent of the MSD at $\tau = 1/\omega$. By expanding $\left\langle \Delta r^2(\tau) \right\rangle$ locally around the frequency of interest ω and retaining the leading terms, the GSER can be rewritten as

$$G(\omega) = \frac{n k_B T}{3\pi a \left\langle \Delta r^2(1/\omega) \right\rangle \Gamma\left[1 + \alpha(\omega)\right]}, \tag{4.6}$$

where Γ denotes gamma function and

$$\begin{aligned} G'(\omega) &= G(\omega)\cos\left(\pi\alpha(\omega)/2\right) \\ G''(\omega) &= G(\omega)\sin\left(\pi\alpha(\omega)/2\right). \end{aligned} \tag{4.7}$$

The approximation given by Eq. (4.6) gives minimal deviation from the exact result, with the error estimated to be less than 15% [141]. A second-order approximation has also been suggested in the literature that can improve the results when $\left\langle \Delta r^2(\tau) \right\rangle$ is sharply curved and, as a result, $\alpha(\omega)$ changes rapidly [142-144]. For systems investigated in this thesis, however, the second-order contribution was found to be negligible (data not shown) and, therefore, Eqs. (4.6) and (4.7) are sufficient to obtain microrheological information from the probe dynamics.

Figure 4.1 summarizes and schematically illustrates the steps involved in typical PTM data analysis.

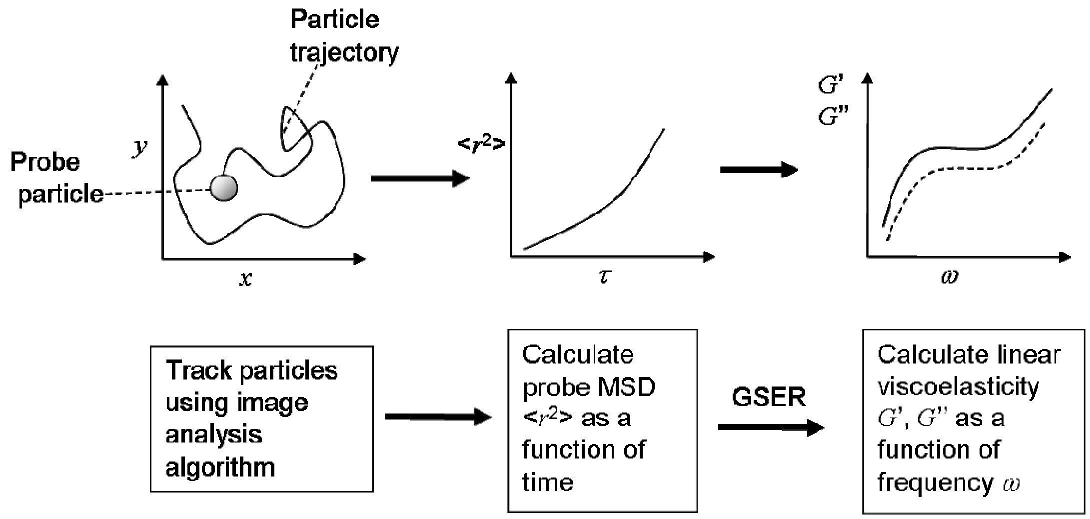

Figure 4.1: Workflow of particle tracking microrheology measurement.

4.3 Materials and Methods

4.3.1 Collagen hydrogel preparation with embedded beads

Collagen solutions were prepared as described in Section 2.2.1. Carboxylate-modified polystyrene fluorescent microspheres (580/605) with 0.5 or 1 µm diameter (Invitrogen, Carlsbad, CA) were used as the fluorescent markers. These beads have fairly robust fluorescence and do not bleach appreciably over the course of typical microrheological measurements (minutes). The bead stock solution was added to the collagen solutions on ice to obtain a final bead concentration of 0.02% by weight. To form the gels, 200 µl of these bead-collagen solutions were deposited in the well of glass-bottom dishes (MatTek Corp., Ashland, MA) and incubated at 37°C for at least 60 minutes to allow gelation. Following typical cell culture assays with collagen scaffolds, the formed gels were hydrated by adding ~2 ml phenol red-free DMEM (GIBCO/Invitrogen, Carlsbad, CA) containing 10% FBS and 1%

penicillin/streptomycin.

4.3.2 Imaging

Two imaging methods were used to track the probe motion. First, confocal time series images of fluorescent beads in collagen gels (focus on one optical slice, no z-stacking) were collected with confocal fluorescence microscopy on Nikon TE2000 inverted microscope using 60× magnification oil-imersion objective (NA = 1.49) at a pixel size of ~0.25 μm/pixel and a frequency of ~2 frames per second (fps). Excitation was provided with continuous diode laser (Olympus) tuned to 561 nm at 5 mW. Fluorescence emission was passed through a 605 ± 38 nm filter to limit stray light. Second, epi-fluorescence videos of beads in collagen gels were collected using high-speed Fastcam SA3 camera (Photron) with the same 60× oil-imersion objective at a magnification of ~0.25 μm/CCD pixel and a capture rate of 60-10,000 fps. No fundamental difference in the resulting probe motion was found between the two imaging methods, confirming the stability of our imaging setup and particle tracking algorithm. All measurements were conducted in a temperature-controlled microscope chamber at 37°C. Intensity, gains, and offsets were adjusted to maximize the signal-to-noise ratio and prevent intensity saturation that can compromise the accuracy of particle localization.

4.3.3 Probe tracking

After image acquisition, offline image processing to track the probes and the subsequent microrheological analysis were done in MATLAB (The MathWorks, Inc., Natick, MA).

The particle tracking algorithm used was based upon routines developed previously in IDL [145,146], with improvements implemented to reduce the adverse effects of fluorescence saturation, particle aggregation, and existence of debris, as well as to increase centroid calculation accuracy. Briefly, the algorithm starts by smoothing the spatial intensity in each frame using a band-pass filter and identifying rough, pixel-level positions of features of appropriate parameters based on the peaks of intensity in each frame. To refine the feature localization to subpixel accuracy, a mask of size 5 pixels or more was applied and the locations of each feature's centroid were calculated. For fluorescent images, the point spread function is approximated to be a Gaussian. As such, we alternatively employed a more accurate bead localization using two-dimensional Gaussian least squares fitting for the tracking [147]. A semi-automated subroutine was also written to eliminate undesired features, such as aggregated beads and debris. With this algorithm, a particle localization accuracy of at least ~ 0.1 pixel can be routinely achieved, and an independent calibration is reported in Section 4.4.1. Particle positions in each frame were then correlated with positions in later frames to produce trajectories of particle motion. In practice, for this step to be properly performed, the typical distance a particle moves between frames must be significantly smaller than the typical interparticle spacing. This requirement sets the practical upper limits for probe density and interframe time interval for a sample. Sample drift in the form of synchronized movement of the tracked probes was numerically removed by subtracting any non-random trajectory component.

4.3.4 Extraction of microrheological information

The MSD's of the probe particles were calculated from the trajectories using Eq. (4.1). The extraction of microrheological information from the probe MSD was done using the power-law approximation of the GSER as expressed in Eqs. (4.5), (4.6), and (4.7). Initially, the local-power-law exponent $\alpha(\omega)$ was numerically estimated from $\langle \Delta r^2(\tau) \rangle$. Briefly, for each data point in $\langle \Delta r^2(\tau) \rangle$, a second-order polynomial was fitted on the neighboring data points using a sliding Gaussian window and used to calculate the local zeroth- and first-order logarithmic derivative, corresponding to the smoothed $\langle \Delta r^2(\tau) \rangle$ and extracted $\alpha(\omega)$ data, respectively. The same algorithm can be easily employed to obtain the second-order derivative should a second-order GSER prove necessary [143]. Finally, the shear moduli were obtained from the $\langle \Delta r^2(\tau) \rangle$ and $\alpha(\omega)$ data using Eqs. (4.6) and (4.7). In contrast to the approximation described earlier [141], no algebraic approximation were used to represent the gamma function.

4.4 Results and Discussion

4.4.1 Discrepancy with mechanical rheology results

The upper limit of G' and G'' that can be measured using PTM is set by the accuracy of particle localization during the tracking, which is dependent on the quality and stability of the imaging setup as well as the tracking algorithm itself. A simple way to estimate the upper limit is by performing PTM on immobilized particles, where the MSD directly reflects the smallest particle displacements that can be reliably recorded. From such independent experiments, we find that, for our PTM setup, the highest MSD resolution is ~ 5×10^{-5} $\mu m^2/s$, corresponding to an upper limit for stiffness measurement of ~73 Pa. PTM measurements on materials with larger stiffness, therefore, may not yield reliable results.

In view of the expected stiffness of collagen networks, such as the measurements obtained using mechanical rheology [*e.g.*, Figure 2.10(A)], we performed PTM on collagen gels with a range of concentration of 1.5–3.5 mg/ml. For each sample, microrheological data were obtained from 2–3 sets of image sequence taken at different locations in the sample. From the tracked probe trajectories, the ensemble-averaged MSD was used to calculate the shear moduli $G'(\omega)$ and $G''(\omega)$. Within the range of frequency measured and collagen concentration tested, $G''(\omega)$ is roughly one order of magnitude smaller than $G'(\omega)$ (data not shown). This is indicative of the dominant elastic nature of collagen networks and is consistent with mechanical rheology (MR) results presented earlier in Section 2.3.2 . The elastic modulus G' is shown and contrasted with the corresponding MR results in Figure 4.2.

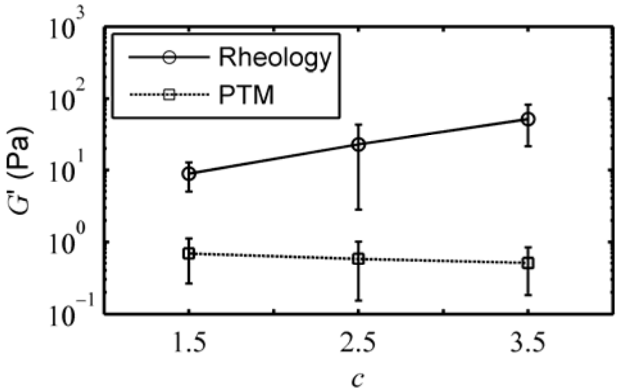

Figure 4.2: Comparison between rheological (circles) and microrheological (squares) measurements of collagen networks for a concentration range of 1.5–3.5 mg/ml. Error bars represent the standard deviations.

There are two prominent discrepancies between PTM and MR results. First, the G' of collagen networks with c = 1.5–3.5 mg/ml measured using PTM varies around 0.1–1 Pa, much smaller than the G' measured using MR (10–100 Pa). Second, in PTM, G' hardly varies with concentration, in direct contrast to MR results, where our earlier fit in Section 2.3.4 reports $G' \sim c^{1.9}$. Several possible reasons could be put forward to explain these discrepancies. First, the network formation during the gelation process is different in the two methods. In PTM the network is formed by depositing an aliquot of the precursor solution in a dish and incubating at 37°C, while in MR the network is formed *in situ* between the parallel plates of the rheometer. Consequently, the dimension, topology, hydration, and fractions of free and anchored surfaces of the network are different, all of which can give rise to differences in the network microstructural properties. Given the importance the actual network architecture and structure hold in determining the resulting network mechanics, as we have shown in Chapter 3, variation in the gelation process may be responsible for the observed discrepancies between PTM and MR.

Even differences in the measurement protocols and specifications of the rheometer can influence the measurement readings [82]. To verify that this is indeed the source of the discrepancies, it is necessary to be able to perform both measurements on the same samples. We were not able to test this, however, as the gels were extremely fragile and were easily damaged when transported between the two platforms of measurements.

4.4.2 Matrix heterogeneity

Another possible cause for the discrepancy with MR results is heterogeneity of the networks. As we have shown in Chapter 3, semiflexible polymer networks can behave differently at different length scales. The length scales probed using PTM is comparable to the probe size (~ μm). Therefore, in contrast to MR, where the measurable length scales are much larger (~ mm), PTM can capture mechanical heterogeneity within the network. To probe the heterogeneity of collagen networks, we next look at the MSD data of the individually tracked particles. Figure 4.3 shows the distribution of probe MSD at different locations within a single sample of 1.5 mg/ml collagen network. All individual MSD’s have very weak time-dependence, which corresponds well with the weak frequency-dependence of G' both in PTM and MR. Strikingly, however, the magnitude of MSD varies from 6×10^{-5} μm^2/s (close to the MSD resolution obtained from images of immobile particles) up to 2×10^{-2} μm^2/s. This observation implies that while some probe particles are virtually immobile within the network, some others can move with much less resistance from the surrounding matrix.

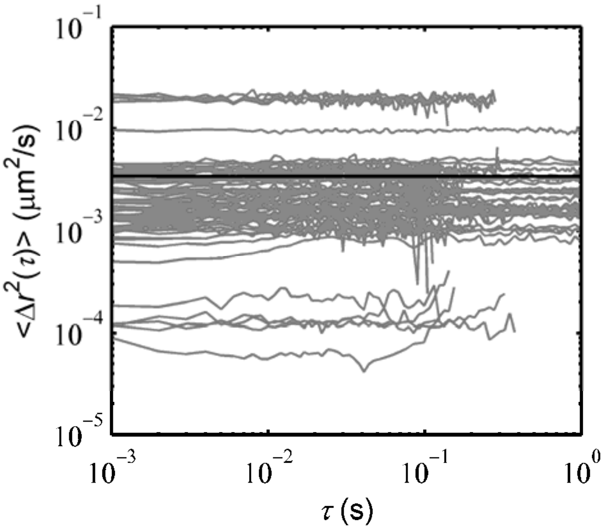

Figure 4.3: Typical distribution of probe MSD in a single sample of 1.5 mg/ml collagen network. The gray curves are the MSD of individual probes, calculated from the trajectories of the tracked probes. The solid line denotes the ensemble averaged MSD.

The local G' around each probe can in principle be calculated from the MSD of the individual trajectories using Eqs. (4.6) and (4.7). As shown in Figure 4.4, the local G' varies over almost three orders of magnitude from 0.03 to 30 Pa in the frequency range of 1–10^3 rad/s. Such a large variation reflects the degree of mechanical heterogeneity of collagen networks, even within the same sample. Similar extent of variation has also been reported in collagen network as measured using active laser-trap microrheometry technique [148]. This finding bears important implications for the interpretation of cell mechanobiology studies. So far, cell behavior as a function of bulk substrate stiffness in 3D matrices has always been studied with the assumption of homogeneous environment, such as through mechanical rheology measurements, and conclusions have been drawn based on the 'average' behavior of the cell populations. However, as we have shown here, the stiffness of the local environment in the immediate vicinity of the cells, which is likely what is actually sensed by the cells, rather than the bulk stiffness, varies significantly. It is therefore essential that cell behavior in response to substrate stiffness be interpreted in the context of the local environment, which can be measured using microrheological techniques.

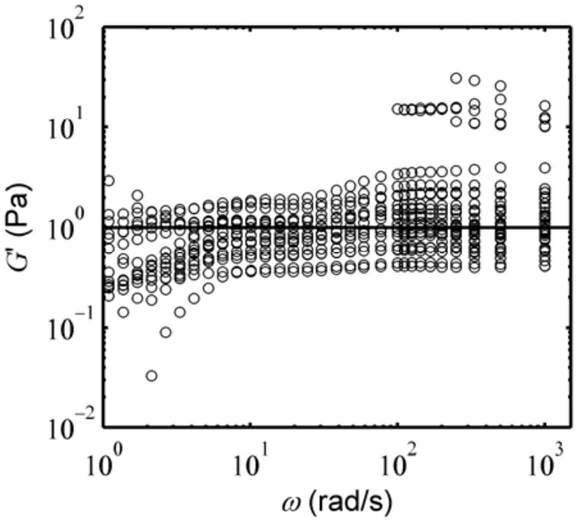

Figure 4.4: Typical distribution of the storage modulus $G'(\omega)$, as a function of frequency ω, for 1.5 mg/ml collagen network. The data points (circles) are obtained from individual probe trajectories at different probe locations in the same sample. The solid line denotes the G' at $\omega = 10^3$ rad/s calculated from the ensemble averaged MSD of the probes.

Although the origin of the observed heterogeneity is unclear, our computational studies in Chapter 3 suggest that it is likely linked to the local network connectivity and fiber entanglements, which are not straightforward to monitor experimentally. On the other hand, the effect of the local network architecture on the probe motion can be analyzed by observing the trajectories of the individual probes. We plot some representative trajectories in Figure 4.5 with the same scale for easy comparison. It can be seen that the amount of particle motion during the tracking vary from one particle to the next, as indicated by the variation of the size of the displacement trajectories. Furthermore, some trajectories seem to have preferential axes of motion as well as directional displacements. These qualitative observations strongly suggest heterogeneity and anisotropy of network mechanical properties at short length scales, arising from the physical restrictions imposed by the local, surrounding fibrous environment.

Multiple particle tracking microrheological methods, such as two-point microrheology [142], have been suggested to provide better comparison with bulk rheology for heterogeneous materials, including biopolymer networks [111]. However, in this method, the analysis is done on the relative motion of multiple probes, thus effectively increasing the length scales of the measurement and sacrificing the capability of obtaining local properties. In addition, in practice, significantly more probe statistics is needed and the analysis is more noise-prone compared to single particle tracking microrheology.

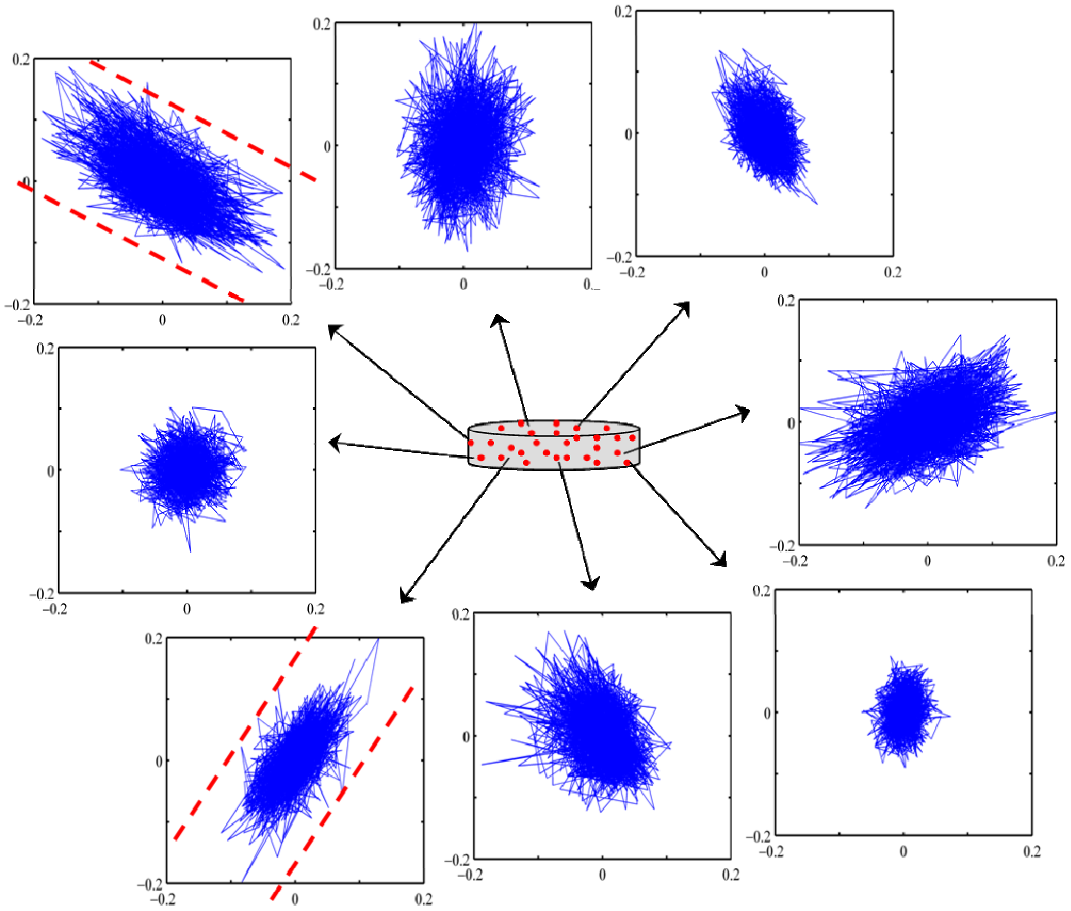

Figure 4.5: Typical trajectories of probe particles in a single collagen network sample. The trajectories are obtained by tracking the motion of multiple probes in a total duration of 2 seconds, starting from origin. The abscissa and ordinate are the *x* and *y* displacements in μm, respectively, in two-dimensional particle tracking. The parallel dashed lines are guides for the eye.

4.5 Discussion

Despite the importance of elucidating the origin and effect of material heterogeneity at short length scales, especially in the context of cell-matrix interactions, there remain outstanding questions that need to be solved. While microrheological techniques and structural imaging of the network can provide valuable qualitative information, as we have shown in this chapter, more quantitative analyses are hampered by experimental difficulties with associated with PTM, both technical and practical. These difficulties include:

1. It is not straightforward to determine whether the measured stiffness arises from the stiffness of the individual fibers or of the network. The network mesh size is of comparable size to the size of the probes. As a result, it is equally probable for a bead to be attached only to a single fiber as it is to be firmly enclosed in a cage of fibers, bearing in mind the heterogeneity of fiber distribution and connectivity in the network.
2. The typically used probes in PTM are inert and do not bind specifically to the surrounding fibers. This makes it possible for the beads to slip through the network or undergo effectively unrestricted, although confined, Brownian motion inside the naturally formed ‘cages’ in the network. On one hand, one can utilize these events, for example, to obtain a size estimate of the microstructural pores in the network [111,149]. On the other hand, however, these invalidate the calculation of the material moduli [150]. In addition, the assumption used in GSER that the probes be in continuum with the surrounding medium can be violated.
3. On the more practical side, the beads used for tracking often aggregate in the formed collagen networks. This not only causes problems in the image post-processing step, but also degrades the calculation statistics and the spatial resolution of the *local* microrheological properties, due to the increased spacing between analyzable probes.

To tackle these problems, one can either probe deeper into the more technical aspects of PTM or develop new techniques that can solve or circumvent some of the problems associated with PTM. For the former, we propose future studies that can help further improve the applicability of PTM in soft matter systems, including biological networks, in Section 7.2. For the latter, we propose a new microrheological technique based on image correlation spectroscopy and demonstrate its use in several soft matter systems in Chapter 5 and Chapter 6.

Chapter 5: Image Correlation Spectroscopy for Microrheology

5.1 Introduction

5.1.1 Problems with current microrheological techniques

As we have discussed in Section 4.5, current microrheological techniques, such as particle tracking microrheology, still have some limitations that need further investigations. On closer inspection, many of the problems associated with PTM have to do with the probe introduction and probe-material interaction. Therefore, one should be able to circumvent many of these problems if indigenous particles are used as microrheological probes. In fact, doing so works well with the approach used in various experiments, biological or otherwise, where imaging of labeled or unlabeled native particles is routinely done to gain other types of information. To this end, we present in this chapter how microrheological information can be obtained through image correlation spectroscopy, a very versatile technique whose applications have so far been limited to the biophysical field.

5.1.2 Image correlation spectroscopy

Image correlation spectroscopy (ICS) is a family of techniques that has evolved to be powerful tools to obtain spatiotemporal biophysical information from images. In ICS, the fluctuation of imaged fluorescent entities across space and time are systemically analyzed and used to infer the desired quantities. ICS has been successfully used, under different names [151-155], to measure spatial and dynamic processes taking place in biological settings, including receptor distribution on cell membrane, diffusion coefficient of molecules on membrane, and protein flow and interaction in living cells. The key principle and simplicity of ICS allows it, however, to be easily extended to areas beyond biophysical sciences, such as studies of diffusion phenomena in colloids and microemulsions, polymer or surfactant films and membranes, etc. Specific technical advances in ICS and their corresponding terminologies and applications in the biological context have been reviewed extensively in [156], but the full potential of the techniques is yet to be realized. Figure 5.1 summarizes some of the practical uses of ICS that have been developed in the last few years.

ICS was originally introduced as an extension of another technique, fluorescence correlation spectroscopy (FCS). FCS, like ICS, is also a versatile technique that allows quantification of the dynamics of fluorescent molecules based on the fluctuation of fluorescent intensity within the observation volume [157], as schematically illustrated in Figure 5.2. Many of the mathematical developments in ICS, including the functional forms required to analyze correlation functions, have been derived from the FCS formulations. As an imaging analog of FCS, ICS uses fluorescence microscopy imaging to sample spatial intensity fluctuations as well as temporal fluctuations. This inherent parallel sampling not only results in better averaging in ICS for slow transport dynamics compared to FCS [152], but also allows high-throughput quantification of spatial information such as number densities or cluster aggregation states [151,158].

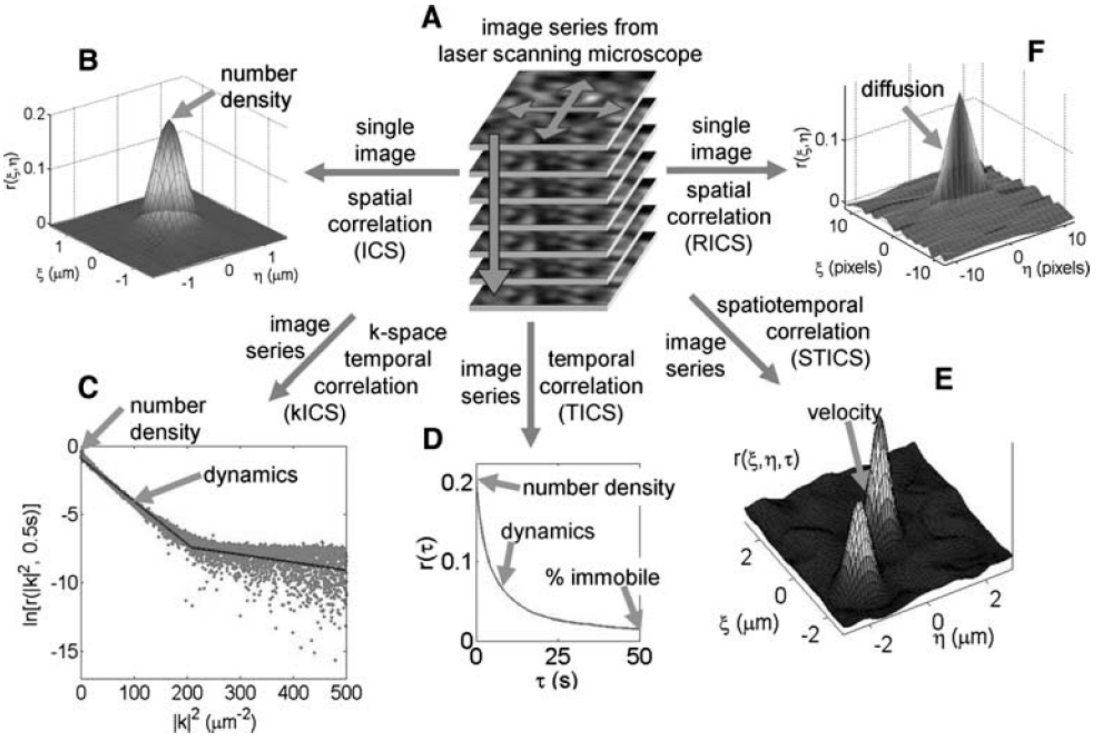

Figure 5.1: An overview of the various ICS techniques that have recently been developed for various purposes. The raw data in ICS is image time series that are typically acquired using fluorescence microscopy (A). Spatial ICS analysis on an image can provide information on the number density and aggregation state of the imaged particles (B). The images can also be analyzed temporally using k-space ICS (C) or temporal ICS (D) to measure the dynamics (*e.g.*, diffusion and flow) of particles and quantify the immobile fraction of the population. Simultaneous spatial and temporal analyses are done in spatiotemporal ICS (E) to precisely measure the direction and magnitude of concerted flow in the sample, in addition to the diffusive motion. Raster ICS (F) utilizes the different fast and slow components of the laser raster scan inherent in confocal laser scanning microscopy to measure fast transport dynamics in time scales shorter than typical image capture rate. Adapted with permission from [156].

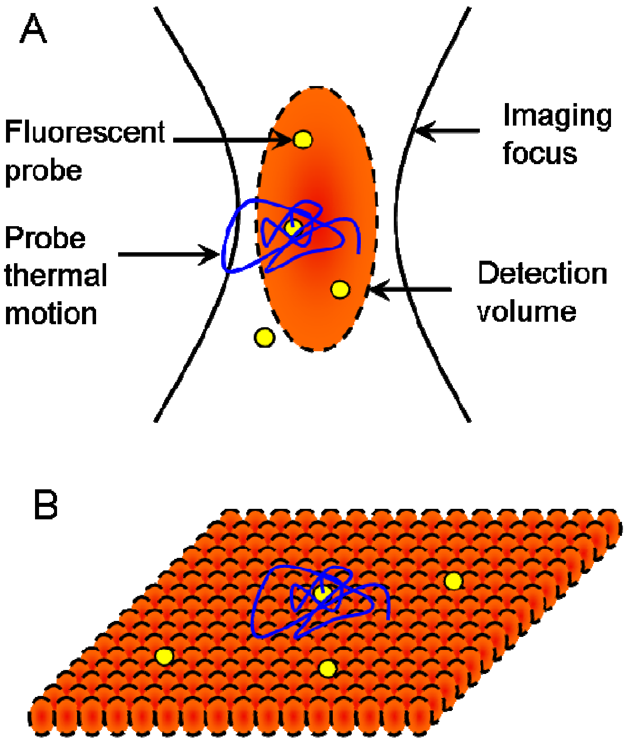

Figure 5.2: Schematic illustration of the working principle of FCS and ICS. In FCS (A), the motion of the fluorescent probes are detected for a small (picoliter) detection volume. In ICS (B), the same detection is done in parallel over the entire image.

There are a number of assumptions and approximations in ICS, however, which have so far limited the potential of ICS for use in various interesting applications. One assumptions in performing temporal measurements of ICS is that the material property of interest is stationary in the measured time frame (*i.e.*, it does not have time-scale dependence). For example, the measured diffusion coefficient is taken to be essentially an 'effective' diffusion coefficient, based on the assumption that a single power-law dependence describes the image correlation function measured. In many systems, however, the behaviors of materials of interest are characterized by phenomena with multiple temporal and/or spatial scales. In particular, complex materials and viscoelastic networks such as polymers and biological materials exhibit both elastic and viscous behaviors over wide frequency and spatial ranges, as well-known in the field of rheology of complex fluids and soft matter. In this chapter, we explore the possibility of obtaining microrheological measurements (*cf.* Section 4.2) using ICS. The objective is to fully utilize and extend the imaging-based approach used to obtain spatiotemporal information in ICS to concurrently obtain valuable microrheological information in ICS-Microrheology (ICS-μR). How ICS-μR relates to and extends the original capabilities of ICS is illustrated in Figure 5.3.

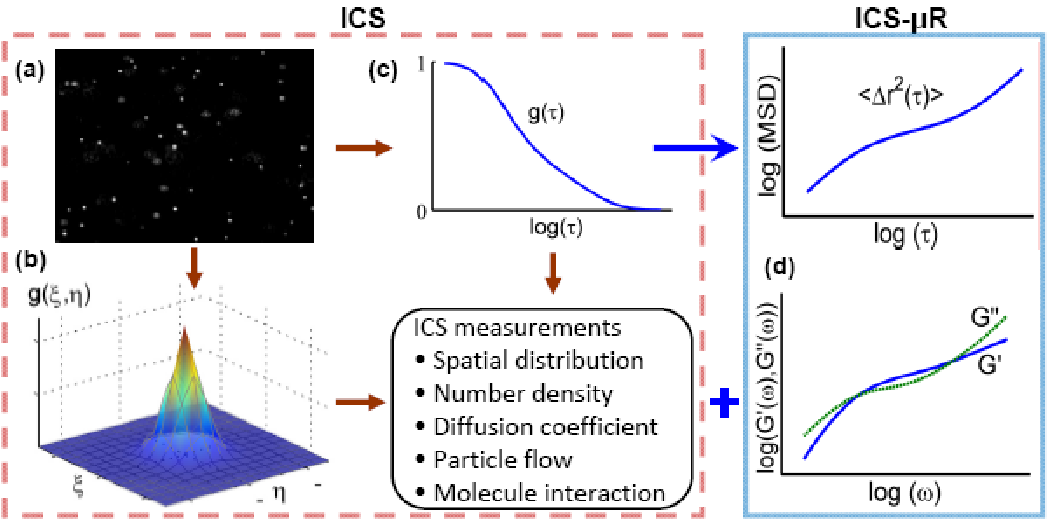

Figure 5.3: A schematic overview of ICS and its extension to microrheology, ICS-μR. A sequence of images (a) is correlated spatially (b) and temporally (c) in ICS. Functional spatial and temporal fitting to these correlation data allow one to quantify various spatiotemporal phenomena characteristic of the system studied, as listed in the box below (c). The present work (d) shows how such image data can be further interrogated to gain microrheological information in ICS-μR.

In the following sections, we first briefly describe the experimental procedures and data collection for ICS-μR. Then, we discuss our approach to extract mean-squared displacements (MSD) of the probe particles from the image correlation data using a new model we introduce here for the power-law exponent of the MSD.

We show that this technique works very well for a wide range of soft matter, from colloids of hard or soft particles to polymer solutions and networks. Following this, we demonstrate the ability of ICS-μR to provide rheological information by measurements of simple (Newtonian) as well as complex fluids.

5.2 Materials and Methods

In the series of experiments reported here, we have used aqueous solutions of glycerol at different concentrations as reference Newtonian fluids, as the viscosities of glycerol solutions in water are well-known and have been reported previously [159]. As model viscoelastic fluids, we choose aqueous solutions of poly(ethylene oxide) (PEO) of molecular weight M_W = 10^6 g/mol. To achieve different viscoelastic properties, measurements were done at different PEO concentrations above the overlap concentration c^* [defined below; see Eq. (5.1)]. Commercial fluorescent microspheres were used as probe particles, and the MSD of the particles were extracted from the analysis of the ICS data using a special procedure that will be described later in Sections 5.2.5 and 5.3.1. The rheological properties were then calculated from these MSD data using the generalized Stokes–Einstein equation [141]. The microrheological measurement results are compared with the results obtained from conventional rheological experiments.

5.2.1 Sample preparation

PEO-water solutions were prepared by dissolving PEO with a molecular weight of M_W = 10^6 g/mol (Sigma Aldrich) in water to final concentrations c of 1, 2, and

3% by weight. The overlap concentration of PEO solution can be estimated using [160]

$$c^* = \frac{M_W}{\frac{4}{3}\pi R_g^3 N_A}, \tag{5.1}$$

where N_A is Avogadro's constant and the radius of gyration is estimated from [161]

$$R_g = 0.0215 M_W^{0.58} \text{ nm}. \tag{5.2}$$

We have chosen c such that $c \gg c^*$ ~ 0.15% to guarantee a clear viscoelastic response. To ensure complete dissolution, PEO solutions were kept in an incubator at 37°C for at least 10 days with regular gentle shaking. Carboxylate-modified polystyrene fluorescent microspheres (580/605) with 0.5 μm diameter (Invitrogen, Carlsbad, CA) were used as the fluorescent markers. The bead stock solution was added to the glycerol or polymer solutions to obtain a final bead concentration of 0.02% by weight. The mesh size of the PEO solutions can be estimated from [161]

$$l_m = R_g \left(c^*/c\right)^{0.75}. \tag{5.3}$$

For 1, 2, and 3% PEO solutions used in this study, the mesh sizes are estimated to be 6.3, 8.6, and 14.5 nm, respectively. These are significantly smaller than the size of our probe particles, so that that ICS-μR measures the rheological response and properties of the polymer network (rather than those of the solvent).

5.2.2 Mechanical rheometry

For comparison, the viscoelastic moduli of the PEO solutions were also measured using an AR-G2 rheometer (TA Instruments, New Castle, DE) using dynamic shear mode, parallel-plate geometry, and a humidity chamber to minimize evaporation. The rheometer plate diameter was 60 mm, and the gap between the plates was 0.25 mm. Strain sweep tests were conducted to determine the linear viscoelastic regime of the solutions. Subsequently, all frequency sweep tests were done under 5–10% strain, sufficiently low to ensure linear response. The measurements were repeated several times to check their reproducibility. All measurements were done at 25°C.

5.2.3 Imaging

Epifluorescence video images of the probe particles were collected at 25°C using a Nikon TE2000 inverted microscope with 60× oil-immersion objective (NA = 1.49) at a capture rate of 1,000–10,000 frames per second with a high-speed Fastcam SA3 camera (Photron). Image sequences of less than one-minute long were obtained with 256×256 or 512×512 pixels. Data for each sample was obtained from 3–5 such image sequences. Fluorescence emission was passed through a 605 ± 38 nm filter to limit stray light. Image size and capture rate were not found to have significant effect on the ICS results, and photobleaching was not observed in the duration of imaging used in this work.

5.2.4 Data collection and analysis: ICS

In this section, we briefly outline the steps involved in the standard ICS measurements and analysis, which supply the data for ICS-μR described in the next subsection. More detailed information with a schematic of the data treatment is available in Appendix A.

The raw data obtained in ICS is a sequence of images which represent the image intensity $i(x,y,t)$ in space (*i.e.*, x and y) and time t. The normalized intensity correlation function is calculated as a function of the spatial lag, ξ and η, as well as lag time, τ, by

$$r(\xi,\eta,\tau)=\left\langle \delta i(x,y,t)\,\delta i(x+\xi,y+\eta,t+\tau)\right\rangle_{x,y,t}, \tag{5.4}$$

where $\langle\bullet\rangle_{x,y,t}$ indicates averaging over all x, y, and t, and

$$\delta i(x,y,t)=\left(i(x,y,t)-\left\langle i(t)\right\rangle_{x,y}\right)\Big/\left\langle i(t)\right\rangle_{x,y}. \tag{5.5}$$

The normalization in Eq. (5.5) by the average intensity $\langle i(t)\rangle_{x,y}$ over the entire image at any given instant follows common practice and is done to avoid changes in the intensity variation $\delta i(x,y,t)$ for spurious reasons unrelated to motions of the probe. In addition, the normalization allows direct comparison between samples and extraction of parameters from the correlation amplitude. To minimize computation time, $r(\xi,\eta,\tau)$ is calculated using the Fourier method [162]. As typical in ICS analysis [152,162], for each time lag τ, the spatial correlation function is taken to be a Gaussian of the form:

$$r(\xi,\eta)=g\times\exp\left(-\frac{(\xi-\xi_0)^2+(\eta-\eta_0)^2}{d_0^2}\right)+g_{s,\infty}, \tag{5.6}$$

where g, ξ_0, η_0, d_0, and $g_{s,\infty}$ have the following physical significance. Of these, $g=g(\tau)$ is the time-correlation function of the image fluctuation (arising from the Brownian motion of the probe particles) needed for extracting microrheological information. The quantities ξ_0 and η_0 account for any "collective flow" in the image sequence which may arise, for example, due to an inclined microscope stage. (The "collective flow" represents any (real or apparent) collective motion of the probe particles that may exist in addition to the Brownian motion we seek in the images.) The dc component $g_{s,\infty}$ is included to account for non-zero correlation value at large correlation distances, and d_0 represents the width of the Gaussian.

5.2.5 Extraction of microrheological information: ICS-μR

The key information needed from the standard ICS measurements described above is the MSD of the probe particles in the sample, $\left\langle \Delta r^2(\tau) \right\rangle$, which is related to $g(\tau)$ by

$$g(\tau) = g_0 \left(1 + \frac{2\left\langle \Delta r^2(\tau)\right\rangle}{3d_{xy}^2}\right)^{-1} \left(1 + \frac{2\left\langle \Delta r^2(\tau)\right\rangle}{3d_z^2}\right)^{-1/2}, \tag{5.7}$$

where g_0 is the magnitude of $g(\tau)$ at zero time lag. The lateral cross-correlation radius d_{xy} is essentially the lateral e^{-2} radius of the imaging focus determined from Eq. (5.6) by $d_{xy} = d_0(\tau)\big|_{\tau=0}$, which we found to be 0.33 ± 0.03 μm. The axial cross-correlation radius d_z (the axial e^{-2} radius of the imaging focus) was experimentally estimated to be 1.85 ± 0.02 μm from reference measurements using fluids with known viscosities (*e.g.*, water), for which the probe diffusion coefficients are known.

The MSD data can now be converted to viscoelastic moduli using the generalized Stokes-Einstein equation (see Section 4.2). In particular, Eqs. (4.5), (4.6), and (4.7) are used to gives the frequency-dependent storage modulus, $G'(\omega)$, and loss modulus, $G''(\omega)$. However, as noted earlier, we use an alternative method to extract the viscoelastic moduli from $g(\tau)$ obtained from ICS measurements, in order to minimize the propagation of experimental and data processing errors and to increase the accuracy of the extracted moduli. That is, we do not sequentially obtain the MSD from the time-correlation function using Eq. (5.7) and then determine the logarithmic derivative from Eq. (4.5) for subsequent substitution in Eqs. (4.6) and (4.7) for the moduli. The method we use is described in Section 5.3.1.

5.3 Results

In what follows, we examine and demonstrate the utility of ICS-μR for extracting rheological information using two different classes of fluids representing two limiting cases, namely, a series of Newtonian fluids with significantly different viscosities and polymer solutions with distinct viscoelastic behaviors. The Newtonian fluids are used to confirm unambiguously that the two-dimensional Gaussian function used [*i.e.*, Eq. (5.6)] is sufficient to represent spatial image correlation in our imaging experiments as well as to check the accuracy of the measured viscosities. The polymer solutions are used to test how ICS-μR can be used to identify viscoelastic material behavior.

We begin the discussions with the preliminary step we use to obtain MSD data for the probe particles from the temporal image correlation function $g(\tau)$ obtained from ICS. In principle, $\left\langle \Delta r^2(\tau) \right\rangle$ can be obtained directly from $g(\tau)$ using Eq. (5.7). However, in order to minimize the propagation of experimental error and to obtain reliable microrheological result over as large a τ range as possible, we use a data analysis procedure which allows one to obtain $\left\langle \Delta r^2(\tau) \right\rangle$ and $\alpha(\tau)$ simultaneously. Note that robust values of both $\left\langle \Delta r^2(\tau) \right\rangle$ and $\alpha(\tau)$ are required for calculating the viscoelastic moduli (Eqs. (4.6) and (4.7)). The procedure we use is capable of representing the power-law behavior as well as the transition regime between the low-ω and high-ω regimes of a large variety of soft materials, as will be demonstrated below.

5.3.1 Extraction of MSD from image correlation data

While the use of Eq. (5.6) in ICS helps take care of the noise and drift in the image sequence, it inevitably leads to some 'noise' in $g(\tau)$ due to the intrinsic inaccuracies in data reduction. Direct MSD calculation from this noisy $g(\tau)$ data using Eq. (5.7) would therefore result in MSD data of at least equal level of noise. Obtaining $\alpha(\tau)$ from the resulting MSD adds to the potential propagation of errors. Moreover, prior to the present work, $\alpha(\tau)$ has been usually estimated algebraically from $\langle \Delta r^2(\tau) \rangle$ in the literature, for example using the Gaussian sliding-window approach [143]. This estimation is error-prone and sometimes yields unphysical behaviour both in $\alpha(\tau)$ and the resulting viscoelastic moduli, especially at the ends of the frequency range, thus forcing data truncations [163].

One of the reasons for using the local logarithmic derivative of $\langle \Delta r^2(\tau) \rangle$ for calculating the viscoelastic moduli from diffusive displacements of probe particles is that a wide range of material behaviors over observable frequency range can be described by power laws. In particular, the viscoelastic behavior of many materials including polymer solutions, colloids, and even biological cells follows power laws at the high and low frequency ranges with smooth transition in between [143,164,165], as schematically illustrated in Figure 5.4. Although the underlying phenomena or reasons behind such a "universal" power-law behavior are not completely understood

[139], the possibility of making use of such behaviors is indeed attractive. In this section, we describe a novel MSD extraction method, which eliminates the necessity for calculating $\langle \Delta r^2(\tau) \rangle$ and $\alpha(\tau)$ independently over the entire frequency range and carrying over and compounding the data analysis errors in so doing; in particular, the method reduces the data analysis to finding a robust function for $\alpha(\tau)$ (and hence implicitly for $\langle \Delta r^2(\tau) \rangle$) directly from $g(\tau)$, *i.e.*, from Eq. (5.7).

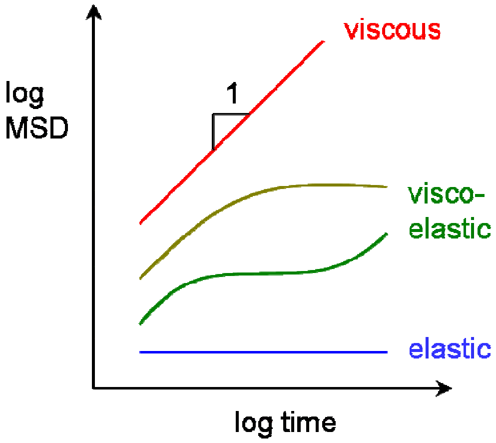

Figure 5.4: Illustration of the evolution of MSD with time.

Considering the prevalence of power laws to describe material behavior, we represent α using a function of the form

$$\alpha(\tau) = \tfrac{1}{2}(\alpha_\infty + \alpha_0) + \tfrac{1}{2}(\alpha_\infty - \alpha_0) \times \mathrm{erf}\left[\chi\left(\ln\left(\tau/\tau_{tr}\right)\right)\right], \tag{5.8}$$

where erf is the error function and the coefficients are related to the asymptotic limits and the transition between the asymptotic limits, as described below. Eq. (5.8) admits two asymptotic power-law behaviors for $\langle \Delta r^2(\tau) \rangle$ with arbitrary exponents (dictated by the experimental data), α_0 at the $\tau \to 0$ limit and α_∞ at the $\tau \to \infty$ limit, and allows a smooth transition between the asymptotes. This function is used to reconstruct $\left\langle \Delta r^2(\tau) \right\rangle$ and $g(\tau)$ from Eq. (5.7), and the time-correlation function thus obtained can be fit to the experimentally obtained data from ICS to determine the coefficients. The parameters τ_{tr} and χ represent where and how fast, respectively, the transition between the two asymptotes occurs. Once the parameters in Eq. (5.8) are obtained from the experimental data, the resulting $\alpha(\tau)$ and $\left\langle \Delta r^2(\tau) \right\rangle$ can be used to calculate shear moduli from Eqs. (4.6) and (4.7) directly.

The main advantage of the approach described above is that in the end one has both $\left\langle \Delta r^2(\tau) \right\rangle$ and $\alpha(\tau)$ that (a) represent the raw $g(\tau)$ data more accurately than sequential data reduction would allow and (b) are physically realistic. The improvement in the quality of the results gained from employing this procedure is further illustrated in Appendix A, where we compare the results obtained from our method with those obtained from the sequential analysis used in the literature. The functional form described in Eq. (5.8) is very robust and can be used for a wide variety of soft materials. In the case of $\alpha_0 = \alpha_\infty$, for example, the material will follow a single power law. In addition, physical limitations can be imposed on these parameters through appropriate constraints, such as $0 \le \{\alpha_0, \alpha_\infty\} \le 1$ for non-superdiffusive events. Importantly, the coefficients in Eq. (5.8) allow one to directly quantify the power laws and the transitions between power laws even at the terminal regimes, a clear advantage over other algorithms [166]. Finally, we note that the error function erf can only have one inflection point, and, therefore, Eq. (5.8) describes a transition between two asymptotic limits. However, a combination of error functions can be used to represent $\alpha(\tau)$ that has two or more inflection points, as we show in the illustrative cases below.

In order to check how well this procedure can reproduce different types of power-law transition behavior, we have examined a number of representative experimental data reported in the literature for a wide range of soft materials. These data cover quasi-hard-sphere dispersions [165], deformable emulsions [138], polymer solutions [143], associative networks [167], as well as cell nuclei [164], and correspond to different types of transitions between low frequency and high frequency asymptotic regimes. Some of these are reproduced in Figure 5.5. Such an examination shows that Eq. (5.8) is quite versatile and can represent the behavior of a variety of soft materials ranging from hard-sphere fluids and fluids of soft deformable "particles" to solutions of polymer coils and networks. Essentially, any functional form that fits the data will provide equally good results. We chose the erf function model due to its simplicity and its ability to accommodate the asymptotic power-law limits. Despite the possibility that the mechanics of some materials may not be fully described by this simple semiempirical model, we found that this model is sufficient for our purposes in this study as well as many reported in the literature (as illustrated in Figure 5.5).

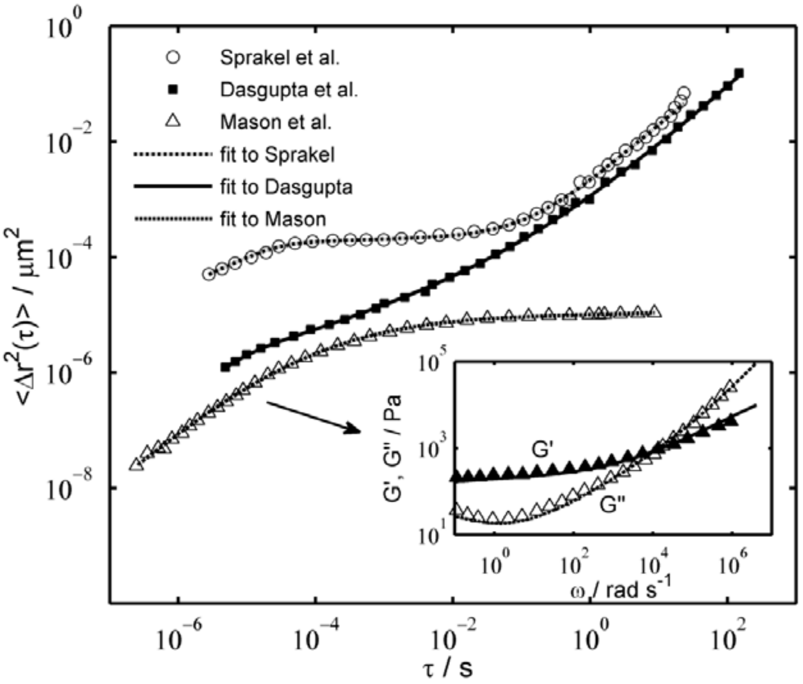

Figure 5.5: Illustration of the capability of our approach to reconstruct $\left\langle \Delta r^2(\tau) \right\rangle$ of reported experimental data. The Gaussian error model [Eq. (5.8)] is able to capture the behavior of the experimental MSD data of silica particles in associative network reported by Sprakel *et al.* [167], polystyrene beads in PEO solutions reported by Dasgupta *et al.* [143], and concentrated emulsion reported by Mason *et al.* [138]. The inset provides one sample comparison between our method, *i.e.*, the viscoelastic moduli calculated from the best fit $\left\langle \Delta r^2(\tau) \right\rangle$ (shown as lines), and the data reported by Mason *et al.* (symbols) based on numerical Laplace transformation. Note that our approach is able to provide reliable viscoelastic information over a larger range in the high frequency limit, where noise may otherwise force data truncation.

5.3.2 ICS-μR for Newtonian fluids

In performing image correlation, one effectively performs spatial convolution of the configurations of the probe particles as well as a convolution of the spatial distribution of fluorescent molecules in the probes.[4] We take this spatial correlation function to be described by a two-dimensional Gaussian function [Eq. (5.6)]. Such Gaussian approximation function may not always be appropriate, for example when

---

[4] This will be discussed in greater detail in Section 6.2. By carefully analyzing the spatial correlation function, one can employ ICS in a probe-independent manner, as demonstrated in Chapter 6.

the probe particle is significantly larger than the imaging PSF. It is necessary, therefore, to ensure that the above Gaussian approximation works in the experiments. To test this, we did ICS-μR measurements with aqueous solutions of glycerol, for which the viscosities are known.

The raw temporal correlation data and the corresponding extracted $g\left(\tau\right)$, based on Eq. (5.8), of glycerol solutions at different concentrations are shown in Figure 5.6(a), while the extracted $\left\langle \Delta r^2\left(\tau\right)\right\rangle$ are shown in Figure 5.6(b). The glycerol concentrations were chosen such that they cover a large range of viscosities (~1–1,000 cp). As expected for Newtonian fluids, the extracted $\left\langle \Delta r^2\left(\tau\right)\right\rangle$'s follow single power-law functions with a slope of unity in all cases. To further check the accuracy of $\left\langle \Delta r^2\left(\tau\right)\right\rangle$, we calculated the diffusion coefficients of the probe particles from these extracted $\left\langle \Delta r^2\left(\tau\right)\right\rangle$ (or, equivalently, the viscosities of the solutions) and found the resulting values to be very close to the expected values (within 5%) over several orders of magnitudes of sample viscosities, as shown in the inset of Figure 5.6(b). This excellent agreement between the measured results and the actual values suggests that the Gaussian PSF in Eq. (5.6) is a sufficiently accurate representation of the spatial correlation of our bead images. Consequently, effects of particle size or distribution of fluorescent molecules within the probe particles, if any, are already accounted for by Eq. (5.6) and has no impact on the extraction of $\left\langle \Delta r^2\left(\tau\right)\right\rangle$ in our experiments.

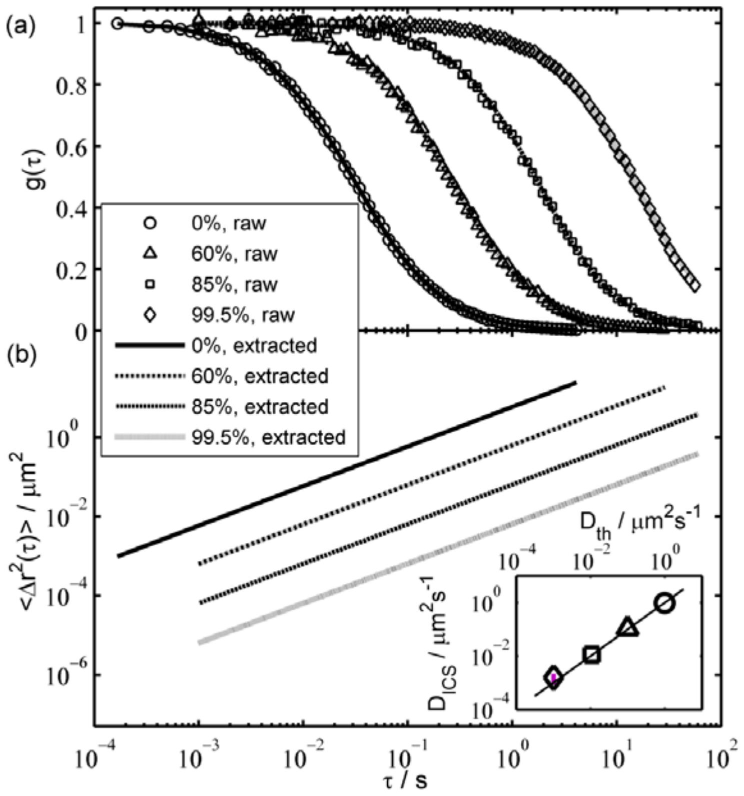

Figure 5.6: ICS-μR results for glycerol aqueous solutions with various concentrations. The raw correlation data (open symbols, panel (a)) are used to extract $\left\langle \Delta r^2(\tau) \right\rangle$ (lines, panel (b)) based on data analysis using Eq. (10). The correlation data have been normalized against the intercept values at zero time-lag for easy evaluation. The inset shows comparison between theoretical diffusion coefficient D_{th} (obtained from Stokes-Einstein equation $D_{th} = k_B T / 6\pi \nu a$, using viscosity values ν measured previously [159]) and measured diffusion coefficient D_{ICS} (obtained by fitting extracted MSD data to $\left\langle \Delta r^2(\tau) \right\rangle = 6 D_{ICS} \tau$). Experimental errors are about the sizes of the symbols or smaller. The solid line represents slope of unity.

5.3.3 ICS-μR for viscoelastic networks

As a demonstration of an application of our ICS-μR method, we made image correlation measurements of probe particles in aqueous solutions of PEO. From the temporal correlation data of PEO solutions with different PEO concentration c, we extracted $\left\langle \Delta r^2(\tau) \right\rangle$, shown in Figure 5.7. The MSD data show the expected monotonic decrease with increasing c, indicating an increase in the complex shear modulus of the samples. For the range of c tested, at small τ, $\left\langle \Delta r^2(\tau) \right\rangle$ has a logarithmic slope α of less than unity, indicating a partial elastic response, and α gradually approaches unity at larger τ, indicating a transition to viscous behaviour, as illustrated in the inset of Figure 5.7. The use of Eq. (5.8) enables us to clearly observe the transition of α in the power laws, including the incomplete transitions to asymptotic power laws at the high-frequency end, which may not be as readily detected otherwise. Further analysis on the parameter χ in Eq. (5.8) reveals that χ, a measure of the rate of transition of the power laws, increases with c as 0.38 ± 0.17 for 1% PEO, 0.53 ± 0.11 for 2% PEO, and 0.66 ± 0.07 for 3% PEO. Although the elastic-to-viscous transition for PEO has been described previously [143,168], this increase of χ with c has not been studied, and its origin is yet unclear.

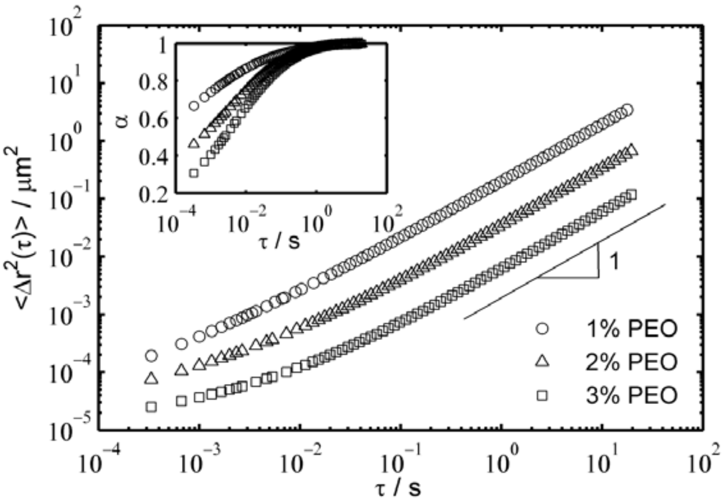

Figure 5.7: MSD of 0.5 μm beads in PEO aqueous solutions with various concentrations obtained from ICS correlation functions. The black line indicates the linear time dependence with a slope of unity expected for pure diffusion. The inset shows the change of $\alpha(\tau)$ over the full time range.

From these $\langle \Delta r^2(\tau) \rangle$ and $\alpha(\tau)$ data, $G'(\omega)$ and $G''(\omega)$ were calculated using Eqs. (4.6) and (4.7). Figure 5.8 shows a comparison between the moduli obtained from ICS-μR and mechanical rheology (MR) measurements for our PEO solutions. We observe a good agreement between the two methods. In particular, we successfully capture the frequency dependence of the moduli, such as the power laws and crossover frequencies, over the measurable time-scale and viscosity range. At low ω, $G"(\omega)$ dominates and rises with a slope of nearly unity. This diffusive behavior reflects the relaxation of polymer chains due to reptation. For larger ω, the cross-over between the two moduli is observed for 2% and 3% PEO and is correctly predicted by ICS-μR. As expected, the cross-over frequency, as indicated by arrows in Figure 5.8, increases with decreasing c. Taken together, these results confirm that our semiempirical representation [Eq. (5.8)] for $\alpha(\tau)$ works well for the materials tested in this work.

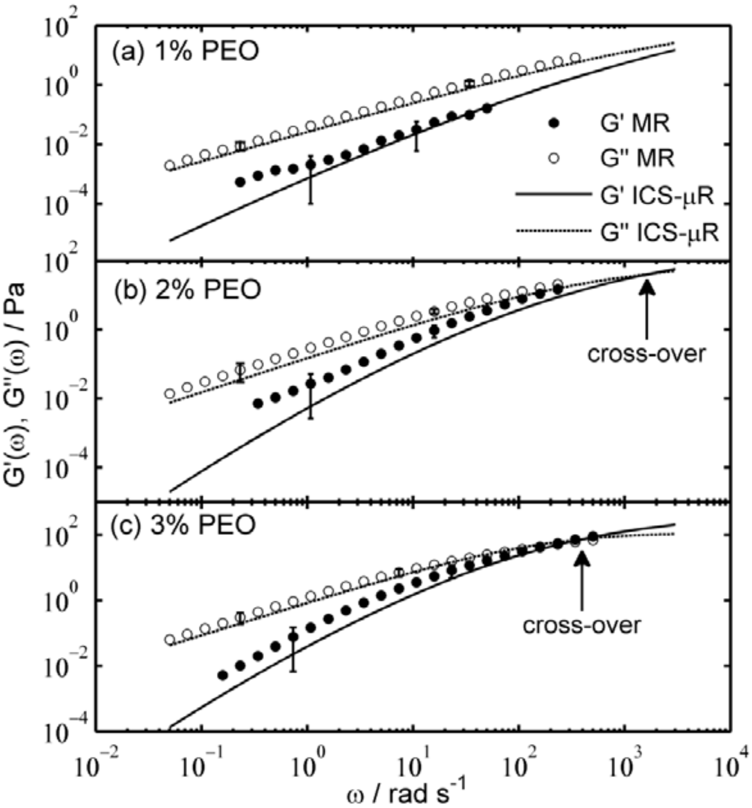

Figure 5.8: Comparison between frequency-dependent linear viscoelastic moduli for PEO aqueous solutions of various concentrations as measured with ICS-μR and mechanical rheometer (MR). ICS-μR results were obtained from $\left\langle \Delta r^2(\tau) \right\rangle$ of 0.5 μm beads in the solutions. The error bars signify the extent of experimental error in the mechanical rheology measurement. For clarity, only representative error bars in high and low frequency regions are shown here.

5.4 Discussion

With ICS-μR and our special data analysis procedure, we were able to detect $\left\langle \Delta r^2(\tau) \right\rangle$ from around 10^{-5} μm^2 to values above 10 μm^2 (*cf.* Figure 5.7). This corresponds to measurable moduli in the range of 10^{-4}–10^{2} Pa. Like any imaging-based technique, the temporal resolution of ICS-μR is limited by capability of the camera used and the signal strength. These typically limit the measureable frequency range to about 10^{-2}–10^{4} rad/s. In terms of probe particle, probes with sizes less than PSF size can be used, although in practice one might also have to consider signal intensity and sample mesh size when very small particles are used. We further discuss the effect of probe size and shape and how to reliably obtain ICS measurements for arbitrary probes in Chapter 6. The $\left\langle \Delta r^2(\tau) \right\rangle$ range for ICS-μR, as shown in Figure 5.7, can be potentially larger than that for standard single-particle tracking microrheology (PTM) [169]. One of the advantages of PTM is its ability to extract information from each individual particle, thus allowing analyses of single particle trajectories as well as correlated motions, which may reveal further information on heterogeneous materials [142] (although, as we also note in Section 7.2.3, any single-particle analysis must be treated with caution, especially in relation to how well the chosen particle couples with the medium or network whose viscoelastic properties are of interest [170,171]). While ICS-μR represents an effectively averaged measurement from the imaged field of view, fine-grained image segmentation with low probe concentrations can allow one to perform single-particle analysis as well. Alternatively, ICS-μR also holds the potential of performing location-dependent microrheological measurements for heterogeneous materials, through collection of image data at different locations in the sample. These approaches hold the potential of providing a spatial rheological map over the imaged sample. Moreover, PTM requires the tracers to be individually distinguishable in the images, and the probe concentration must be sufficiently low such that probe displacement is significantly smaller than average bead-to-bead distances. These are not necessary conditions in ICS-μR. In addition, owing to its better spatial and temporal averaging, ICS-μR is less noise-sensitive than PTM, thus greatly reducing the post-processing of data and computational costs.

Non-imaging-based methods do not have limitations on spatial resolution associated with images. Laser particle tracking techniques achieve better spatial resolution (MSD of ~10^{-6} μm^2 can be achieved), but are not suitable for studying long-time dynamics [172,173]. Light scattering techniques like diffusing wave spectrometry (DWS) have the advantage of larger frequency range, capable of reaching ~10^5 rad/s [138]. However, very high probe concentrations are needed to achieve multiple scattering and the maximum measurable $\left\langle \Delta r^2(\tau) \right\rangle$ is comparatively low [143]. A major upside of imaging-based methods is that no specialized equipment other than a microscope is generally needed. This is clearly favorable, especially for studying biological materials, where microscopy is extensively used. Moreover, in many cases, it is desirable to study material properties in conjunction with its microstructure (*cf.* Section 2.3.1), which usually requires imaging modalities [174]. The minute amount of sample required for measurement (20–30 μl in this study) also makes ICS-μR suitable for measuring materials that are difficult to obtain in large quantities.

In summary, we have introduced ICS-μR for microrheological measurements of complex fluids as an extension of the standard ICS. The measured $\left\langle \Delta r^2(\tau) \right\rangle$ and viscoelastic moduli for glycerol and PEO aqueous solutions are in excellent agreement with results obtained from mechanical rheology and other reported measurements. In extracting $\left\langle \Delta r^2(\tau) \right\rangle$ for ICS-μR, we utilize a semiempirical representation based on the error function to represent the local power-law exponent

$\alpha(\tau)$. This approach proves to be versatile and is able to model particle dynamics measured in ICS-μR as well as in other techniques previously reported in the literature. The usefulness of the above-mentioned representation for $\alpha(\tau)$ is evident when a simple quantification of transient power law and its rate of change are required. The type of analysis proposed here may provide new insights on the power-law behavior of materials. We emphasize, however, that the choice of using the representation we use here and other possible choices are not necessarily critical or essential for the basic concept behind ICS-μR. We use our proposed data analysis approach here simply to take advantage of what has been known previously concerning power-law-based mechanical relaxation of materials and to minimize the propagation of the experimental noise in the data. As an imaging-based technique, ICS-μR has the potential for probing not only time-scale-dependent and length-scale-dependent behavior, but also time evolution and location-dependent mechanical properties of viscoelastic materials [153]. This and ICS-μR's large measurable frequency and MSD ranges as well as its original capability to quantify spatial [151] and temporal [153] phenomena make ICS-μR a powerful characterization tool to gain better understanding of soft matter, such as complex fluids and biomaterials.

Chapter 6: Probe-independent Image Correlation Spectroscopy

6.1 Introduction

Conventional FCS and ICS theory assumes point emitters with sizes much smaller than the beam focus. There are many potential applications of FCS and ICS, however, where the size of the probe is comparable to or bigger than the individual observation volumes, thereby making the point source approximation inadequate or even erroneous. Such applications range from studies of interactions between protein and bacteria or viruses, large cellular vesicles, large membrane domains, macromolecules and colloidal particle characterizations, microemulsions, to material characterization through microrheology [175-178]. We show in this chapter that the geometry, size, and fluorophore distribution of the probe particles affect the shape of the spatial as well as temporal correlation functions in ICS. Although analytical derivations on several simple particle configurations have been described for FCS [179,180], a similar analysis has not been done for ICS.

In this chapter, we present a method that can circumvent problems associated with the effects of geometry, size, and fluorophore distribution of the probe particles in ICS. Rather than dealing with different particle sizes and fluorophore distributions separately, we make use of the spatial information inherently obtained in ICS to help understand how to analyze the temporal information. The theory is validated using computer simulations of ICS on fluorescent bodies of various sizes and fluorophore configurations as well as ICS experiments using fluorescence-labeled microspheres of various diameters.

6.2 Theory

Every fluorescence image is a spatial convolution of the microscope point spread function (PSF) with the point-source emission from the fluorophores lying within the field of view. The PSF describes the response of the imaging system to a point source, and this PSF convolution is what causes the signal from a point-emitter to be spread over a number of pixels. The PSF is determined by the quality of the imaging system, such as coherence, laser focus and pinhole size for confocal setup. However, often, the fluorophores exist as clusters or are bound to substrate domains, e.g., in fluorescent microspheres, which move synchronously and act like a rigid body. As such, without loss of generality, the final fluorescence image can be mathematically represented as

$$i(\mathbf{x},t)=\sigma\left(\mathrm{PSF}(\mathbf{x})*P(\mathbf{x},t)*C(\mathbf{x})\right), \tag{6.1}$$

where $i(\mathbf{x},t)$ is the fluorescence intensity at location $\mathbf{x}$ and time t, $P(\mathbf{x},t)$ is the density distribution of the fluorescent bodies (clusters or domains) in the sample under study, $C(\mathbf{x})$ is the spatial distribution of the fluorophores within the fluorescent bodies, and * denotes convolution operation. Note that, generally, the PSF does not change with time and $C(\mathbf{x})$ is also independent of time for rigid fluorescent bodies. The proportionality coefficient σ is a function of fluorescence quantum yield, detection efficiency, laser excitation intensity, and any geometrical or optical filtering losses, which are typically taken to be constant in space and time.

In general, the complete spatiotemporal image correlation function is calculated as $g(\Delta\mathbf{x},\tau)=\langle i(\mathbf{x},t)\bullet i(\mathbf{x}+\Delta\mathbf{x},t+\tau)\rangle$, where $\Delta\mathbf{x}$ and τ are the spatial and temporal lags, respectively. Given enough probe statistics, the spatial correlation of fluorescence images obtained at different times t involves spatial correlation of the individual components making up the images:

$$g(\Delta\mathbf{x},\tau)\propto\zeta(\Delta\mathbf{x})*\phi(\Delta\mathbf{x},\tau)*\varphi(\Delta\mathbf{x}), \tag{6.2}$$

where $\zeta(\Delta\mathbf{x})$, $\phi(\Delta\mathbf{x},\tau)$, and $\varphi(\Delta\mathbf{x})$ are the spatiotemporal correlations of $\mathrm{PSF}(\mathbf{x})$, $P(\mathbf{x},t)$, and $C(\mathbf{x})$, respectively [181]. $\mathrm{PSF}(\mathbf{x})$ is conventionally assumed to be a Gaussian, and thus $\zeta(\Delta\mathbf{x})$ is also a Gaussian. The distribution $P(\mathbf{x},t)$ of the fluorescent bodies (*i.e.*, the probes) within the sample is determined by the dynamic coupling between the bodies and the surrounding medium. Considering the local fluctuation to be governed by Fick's second law of diffusion, one obtains the diffusion propagator [182]

$$\phi(\Delta\mathbf{x},\tau)=\frac{1}{\sqrt{4\pi D\tau}}\exp\left[-\frac{\Delta\mathbf{x}^2}{4D\tau}\right], \tag{6.3}$$

where D is the diffusion coefficient of the fluorescent bodies in the sample. The calculation of $\varphi(\Delta\mathbf{x})$, however, requires knowledge of the spatial configuration of the fluorophores in the fluorescent bodies, $C(\mathbf{x})$, which is rarely known experimentally.

6.2.1 Conventional ICS for point emitters

For a simple case where the fluorescent bodies are much smaller than the pixel size and the PSF size, $C(\mathbf{x})$ can be considered as a point source represented by the Dirac delta function $\delta(\mathbf{x})$. In this case, the analytical form of the spatiotemporal correlation of the image sequence can be easily obtained from Eq. (6.2). In two-dimensional diffusion ($\mathbf{x} \equiv \{x, y\}$), for example, it has been shown to be given by [183]

$$g(\xi,\eta,\tau) = g(0,0,0)\left(\frac{1}{1+\tau/\tau_D}\right)\exp\left[-\frac{\xi^2+\eta^2}{d^2}\left(\frac{1}{1+\tau/\tau_D}\right)\right], \tag{6.4}$$

where ξ and η are the spatial lags in x and y, respectively, d is the so-called e^{-2} radius of the imaging focus, and τ_D is the characteristic diffusion time, which is related to D through

$$\tau_D = d^2/4D. \tag{6.5}$$

The zero-lag correlation $g(0,0,0)$ has been shown to be the inverse of the average number of fluorescent particles in the field of view [184]. In addition, in the limit of vanishing ξ and η, the temporal correlation function becomes

$$g(\tau) = \frac{g(0)}{1+\tau/\tau_D} \tag{6.6}$$

and thus the diffusion coefficient of the fluorescent particles can be calculated from the $g(\tau)$ data.

6.2.2 Probe-independent ICS

When the fluorescent bodies are of comparable size to, or larger than, the pixel size or the PSF, $C(\mathbf{x})$ can no longer be characterized as a point source. In this case, the form of $\varphi(\Delta\mathbf{x})$, the spatial correlation function of $C(\mathbf{x})$, will influence the eventual spatiotemporal correlation of the image sequence, $g(\Delta\mathbf{x},\tau)$. If $C(\mathbf{x})$ is unknown, which is invariably the case in many experiments, it is difficult to estimate the functional form of the overall spatiotemporal correlation $g\left(\Delta\mathbf{x},\tau\right)$ from Eq. (6.2) as we did for point sources in Eq. (6.4). Assuming an inaccurate form, such as Eq. (6.4), may therefore lead to erroneous determination of the diffusion coefficient (or, equivalently, for the mean-squared displacement of the fluorescent probe particles, needed for ICS-μR; *cf.* Chapter 5), as we shall show in Section 6.4. It is, however, possible to obtain temporal information with little knowledge of the spatial configuration $C\left(\mathbf{x}\right)$, as we now show.

Amongst the components making up the fluorescent images, only $P\left(\mathbf{x},t\right)$ depends on time. As a result, the temporal dependence of $g\left(\Delta\mathbf{x},\tau\right)$ is solely governed by $\phi\left(\Delta\mathbf{x},\tau\right)$. Regrouping the terms in Eq. (6.2) based on the temporal dependence therefore yields

$$g\left(\Delta\mathbf{x},\tau\right)=g\left(\Delta\mathbf{x},0\right)*\phi\left(\Delta\mathbf{x},\tau\right). \tag{6.7}$$

The zero-temporal-lag spatial correlation $g\left(\Delta\mathbf{x},0\right)\propto\zeta\left(\Delta\mathbf{x}\right)*\varphi\left(\Delta\mathbf{x}\right)$ is time-independent, and its functional form depends on $\mathrm{PSF}\left(\mathbf{x}\right)$ as well as $C\left(\mathbf{x}\right)$, whereas $\phi\left(\Delta\mathbf{x},\tau\right)$ is probe-independent and depends only on the diffusivity (i.e., dynamics) of the fluorescent bodies. The correlation data obtained from ICS clearly contains $g\left(\Delta\mathbf{x},\tau\right)$ and hence $g\left(\Delta\mathbf{x},0\right)=\lim_{\tau\to 0}g\left(\Delta\mathbf{x},\tau\right)$ as well. Equation (6.7) therefore implies that $\phi\left(\Delta\mathbf{x},\tau\right)$, and thus the diffusion properties of the fluorescent bodies, can be calculated directly from the spatiotemporal correlation function of the image sequence $g\left(\Delta\mathbf{x},\tau\right)$ without any knowledge about the individual components of $g\left(\Delta\mathbf{x},0\right)$, namely, $\mathrm{PSF}\left(\mathbf{x}\right)$ and $C\left(\mathbf{x}\right)$. This means that, unlike in the conventional ICS analysis [*e.g.*, Eq. (6.4)], no assumptions concerning the geometry of the fluorescent bodies, the spatial distribution of the fluorophores as well as the imaging PSF need to be made for the "generalized" ICS analysis based on Eq. (6.7).

Since $g\left(\Delta\mathbf{x},0\right)$ serves as the 'template' spatial correlation based on which the spatial correlations at any other τ can be analyzed, we will hereafter refer to $g\left(\Delta\mathbf{x},0\right)$ simply as 'template'. The method of finding the diffusion properties of the probe particles using this template will henceforth be referred to as 'template analysis', in contrast to the conventional method of using Eq. (6.4), which will be referred to as 'standard analysis'. While template analysis can be done to evaluate ICS data in any dimensional environment, in the next section, we will in particular describe how we apply the template analysis in practice for two-dimensional environment, where $\mathbf{x}\equiv\left\{x,y\right\}$ and $\Delta\mathbf{x}\equiv\left\{\xi,\eta\right\}$, and demonstrate the use of such an analysis.

6.3 Materials and Methods

6.3.1 Computer simulations

As noted earlier, simulation data are used to test the proposed method of analysis prior to further experimental tests. To this end, computer simulations of laser-scanning microscopy of fluorescent bodies in a two-dimensional system were done to test the effect of particle size and fluorophore distribution on ICS analysis. We employed the procedure described below to generate image sequences of diffusing fluorescent bodies of different sizes and shapes.

1. Assignment of $P(\mathbf{x},t)$: First, we randomly assigned the initial coordinates (*i.e.*, the x and y positions) of the centers of mass of the fluorescent bodies within the field of view. For each subsequent time steps, the new coordinates were calculated from the previous step using standard Brownian dynamics by adding random displacements to the positions of the particles, which was drawn from a normal distribution with a mean of zero and a standard deviation of $\sqrt{2D_{in}\Delta\tau}$, where D_{in} is a predetermined diffusion coefficient of the particles and $\Delta\tau$ is the time steps for the Brownian motion.
2. Generation of density map of the fluorescent bodies: The field of view was divided into a set number of pixels in x and y, and the coordinates of the centers of mass were used to generate a density map of the distribution of the fluorescent bodies. This was done for each time step, so that the result of this step was a sequence of such density maps as a function of time.
3. Assignment of $C(\mathbf{x})$: Three possible distributions of fluorophores on the fluorescent bodies were considered: point sources, disks, and rigid rods. For point sources, $C(\mathbf{x})$ is a delta function, so this step was not needed. Disks were simulated as a set of uniformly distributed point sources within a circle of radius a centered at the assigned centers of mass. Rigid rods were simulated as an array of regularly spaced point sources located in a straight line of length l. The initial orientations of these rods were randomly assigned and were not changed throughout the simulation (*i.e.*, only translational diffusion was considered). The output of this step was a sequence of the density map of the fluorophores in the

field of view. In this work, all the fluorophores were assumed to have the same emission intensity; therefore, the sequence of fluorophore density map is essentially also the sequence of intensity map.

4. PSF convolution: To simulate the effect of excitation of fluorophores with a laser beam in fluorescence imaging, these intensity maps were numerically convolved with a two-dimensional Gaussian of beam width d. The resulting sequence of frames becomes the input image time-series for subsequent ICS analysis.

In practice, the intensities in each frame were normalized such that each pixel contained only integer values ranging from 0 to 65535, simulating 16-bit images. All simulations were performed with an image size of 256×256 pixels, a pixel size of 0.1 μm/pixel, a beam radius of 2–4 pixels, a temporal sampling of 2–4 frames per τ_D, and a total simulation time of at least 500 τ_D. These values correspond to typical laser scanning imaging conditions and diffusion times for proteins in biological settings [153]. Changes in the magnitudes of these parameters may be warranted for other applications and can be easily accommodated within the framework described above. All simulations and data analysis were done in MATLAB (The MathWorks, Inc., Natick, MA).

6.3.2 Sample preparation and imaging

Experimental confirmation for our method was done using carboxylate-modified polystyrene fluorescent microspheres (580/605 nm) with diameters of 0.5, 1, and 2 μm (Invitrogen) as the fluorescent probe particles. A stock solution of probe particles was added to an aqueous solution of glycerol to a final bead concentration of 0.2% by weight. Glycerol solutions were prepared by mixing appropriate volumes of glycerol (Sigma Aldrich) and water to a final concentration of 90.5% by weight.

Confocal laser scanning microscopy was performed at 27.5 ± 1.0°C on a Nikon TE2000 inverted microscope. Excitation was provided with continuous diode laser (Olympus) tuned to 561 nm at 5 mW. All fluorescence image time series were collected by a 100× oil-immersion objective (NA = 1.40) at 5× optical zoom with 256×256 pixels (corresponding to a pixel size of 0.0995 μm/pixel) through a 30 μm pinhole using a 605 ± 37.5 emission filter. Gains and offset were adjusted to prevent intensity saturation. Each image sequence was collected with time delays of 590–610 ms for at least 500 frames.

6.3.3 ICS analysis

As we have pointed out in Section 5.2.4, a two-dimensional image at any time t is represented in terms of the intensity distribution function $i(x,y,t)$. The normalized intensity correlation function was calculated in a similar way as in Section 5.2.4 using Eqs. (5.4) and (5.5). As noted earlier, we used two methods to obtain the diffusion coefficients of the fluorescent bodies, namely, the traditionally used "standard" analysis and the proposed "template" analysis: these have been discussed in Section 6.2.2.

"Standard" Analysis: Here, the function $g(\tau)$, which is required in Eq. (6.6), was obtained by fitting the raw correlation function $r(\xi,\eta,\tau)$ with a two-dimensional Gaussian function for each τ using Eq. (5.6). The spatial matching of experimental (or simulated) data to Eq. (5.6) was done only for the central correlation region

($\xi,\eta < 5\omega$) and with zero weight for $r(0,0)$ to minimize any contribution of white noise at zero spatial lag. The data for $g(\tau)$ thus obtained is used to obtain τ_D using a modified functional form [from Eq. (6.6)] given by [162,184]

$$g(\tau) = \frac{g_0}{1+\tau/\tau_D} + g_{t,\infty}, \tag{6.8}$$

where a temporal offset $g_{t,\infty}$ was included to account for non-zero temporal correlation at long times. The diffusion coefficient D then follows from $\tau_D = d_0^2/4D$, where d_0 is the experimentally found Gaussian width.

<u>“Template” Analysis</u>: In the template analysis we propose in this chapter, for each $\tau > 0$, $r(\xi,\eta,\tau)$ was taken to be a convolution of the “template” $r(\xi,\eta,0)$ with a normalized two-dimensional Gaussian, *i.e.*,

$$r(\xi,\eta,\tau) = r(\xi,\eta,0) * \frac{1}{\pi d_f} \exp\left(-\frac{\xi^2+\eta^2}{d_f^2}\right). \tag{6.9}$$

Note that, in the template analysis, the offset is already absorbed in $r(\xi,\eta,\tau)$ and is no longer necessary in Eq. (6.9). This one-parameter fitting procedure represented by Eq. (6.9) was done by finding the Gaussian width d_f that offers the best fit for $r(\xi,\eta,\tau)$ when the template $r(\xi,\eta,0)$ is convoluted with the Gaussian. The diffusion coefficient D of the fluorescent bodies is related to $d_f(\tau)$ by

$$d_f^2 = 4D\tau \tag{6.10}$$

for two-dimensional free diffusion.

In addition to the two methods above, we also analyzed the correlation function in two other ways:

1. *<u>Point-like Template” Analysis</u>*: Rather than using the experimental template

$r(\xi,\eta,0)$ in Eq. (6.9), a theoretical template assuming point-like particles was used. We call this "point-like template" analysis. By comparing the results from template and point-like template analyses, the influence of the spatial correlations in the image on the temporal correlation can be examined.

2. *"No-offset Standard" Analysis*: As we will show below, while using the offset in standard analysis [*i.e.*, Eqs. (5.6) and (6.8)] is important in experiments, it can produce calculation artifacts when the size of the probes is not taken into account. Therefore, a standard analysis [*i.e.*, Eqs. (5.6) and (6.8)] without the use of the offset fitting parameters, called "no-offset standard" analysis, was also done to elucidate this effect.

6.4 Results

To verify the applicability of our template analysis for ICS, we compare the performances of standard and template analyses in evaluating ICS data from images of fluorescent bodies with various fluorophore configurations, both generated by computer and obtained from experimental confocal imaging.

6.4.1 Probe-independent ICS on simulated images

We tested three shapes for the fluorescent body. First, we considered point sources randomly positioned diffusing in the field of view. The use of point source simulates experiments where the fluorescent particles are very small compared to the laser focus. Second, we generated disk-shaped fluorescent bodies of radius a, with the fluorophores uniformly distributed within the disks. Although experiments rarely encounter such perfectly distributed fluorophores in the fluorescent bodies (even in particles of micrometer or sub-micrometer dimensions), the use of disks with uniformly distributed fluorophores can demonstrate the usefulness of template analysis as compared to standard analysis when a becomes large, as we show below. Lastly, we took the extreme case of rigid rods, where the fluorophores are positioned in a straight line of length l in the fluorescent bodies. Note that the orientations of the line in each fluorescent body are randomly assigned, which means that each fluorescent body is virtually different and has distinct fluorescent signal pattern from each other. These configurations are illustrated in Figure 6.1. The images of these different configurations were convoluted with a two-dimensional Gaussian of $d = 2$ pixels to simulate PSF convolution in confocal imaging. The temporal variations in the positions of these fluorescent bodies were generated using the Brownian motion of the bodies with the same input diffusion coefficient of $D_{in} = 0.1$ μm^2/s for all geometries and sizes.

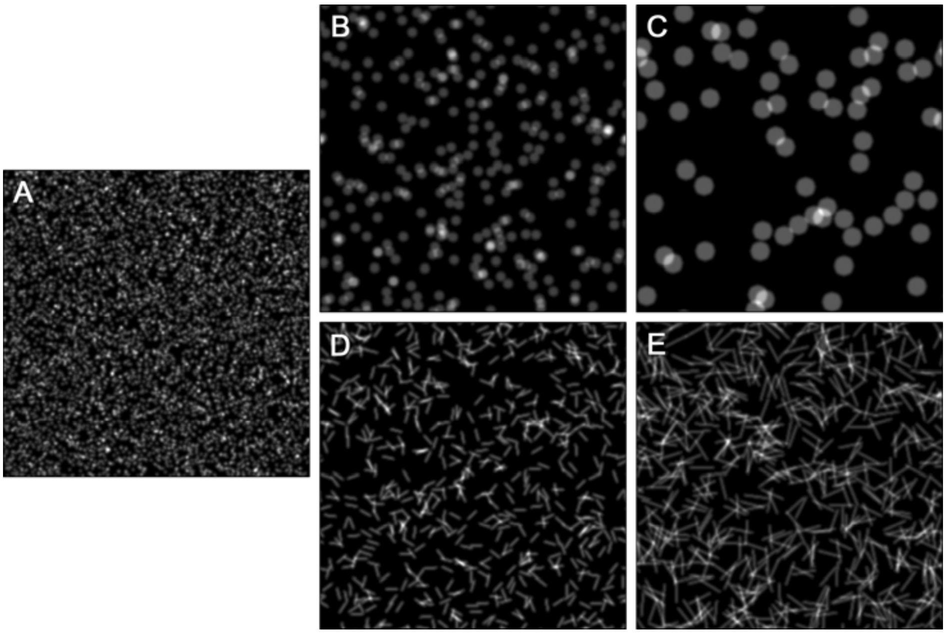

Figure 6.1: Illustration of images generated by computer simulations for ICS with probes of different shapes and uniform fluorophore distribution within the probes. (A) The fluorescent bodies are point-like with zero size. The original fluorophore spatial distribution was convoluted with a Gaussian PSF of d = 2 pixels. (B and C) The fluorescent bodies are disks with diameters of $2d$ (B) and $4d$ (C). (D and E) The fluorescent bodies are randomly oriented fluorescent rigid rods, represented by uniformly distributed fluorophores on a line a long the length of the rods. The lengths of the rods are $l = 5d$ (D) and $l = 10d$ (E). For each sequential frame, the positions of the fluorescent bodies in these images are perturbed according to an input diffusion coefficient D_{in}.

The spatiotemporal correlation function $r(\xi,\eta,\tau)$ was calculated from these image sequences using Eq. (5.4), and we analyzed this raw correlation function using both standard and template analyses. The first step in standard analysis is obtaining the temporal correlation function $g(\tau)$ from $r(\xi,\eta,\tau)$ by fitting to two-dimensional Gaussian as in Eq. (5.6). The resulting $g(\tau)$ data from images of disks and rigid rods for several values of a/d and l/d are shown in Figure 6.2. It can be clearly seen that the form of $g(\tau)$ changes with different values of a/d and l/d . In particular, as a/d and l/d increase, $g(\tau)$ deviates more and more significantly from the theoretical curve (solid line), which assumes point sources and is mathematically represented by Eq. (6.6). The results demonstrate that if the size of the probe particles are not properly accounted for one can mistakenly infer a slower decay in the correlation function for larger values of a/d and l/d, leading to an incorrect measurement of the diffusion of larger particles.

It is worth noting that it takes much larger values of l/d than a/d for $g(\tau)$ to deviate as strongly from the theoretical curve. This is because the rods, with their slender form and random orientations, more closely resemble point sources in the spatial correlation calculations, and, as a result, the spatial correlation functions decay almost as rapidly with spatial lag as for point sources, as shown in Figure 6.3. For purely point sources, $g(\tau)$ follows the theoretical curve as expected. Figure 6.3 provides a closer inspection in the spatial correlation data from the various fluorophore configurations. At small spatial lag, spatial correlation from images of rigid rods decays in a similar manner as that from images of point sources despite the relatively large l/d value. This observation underlines the spatial-temporal interrelation in ICS analysis, which we have mathematically described in Section 6.2.2.

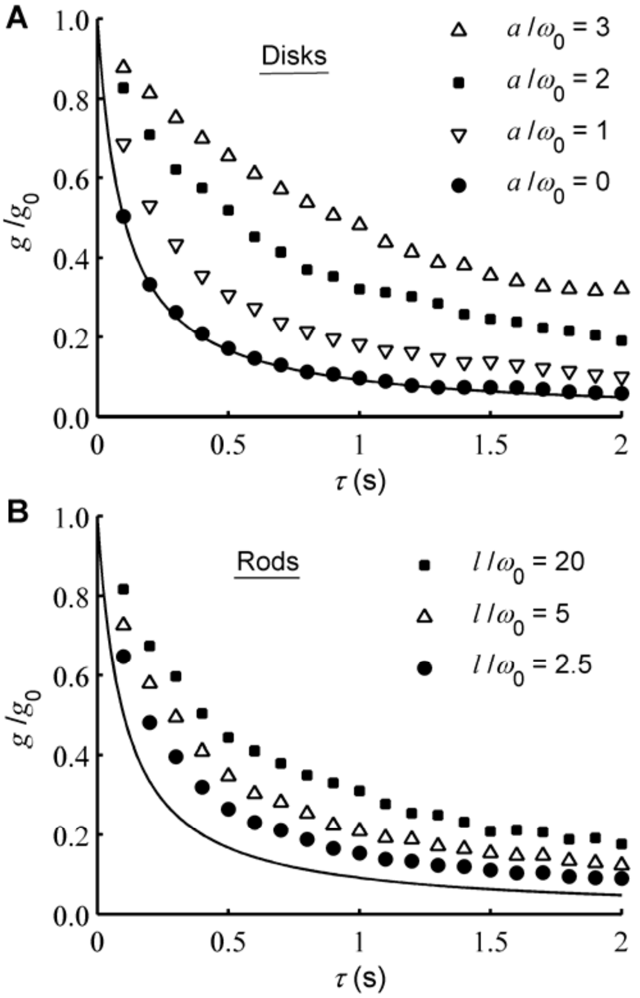

Figure 6.2: The correlation functions $g(\tau)$ of images of different fluorescent bodies. The $g(\tau)$ data were obtained by fitting the spatial correlation function $r(\xi,\eta,\tau)$ for each $\tau > 0$ to two-dimensional Gaussian using Eq. (5.6). The functions have been normalized with respect to the intercept at $\tau = 0$. These $g(\tau)$ functions were obtained for images of disks (A) of $a/d = 0$ (filled circles), $a/d = 1$ (inverted triangles), $a/d = 2$ (filled squares), and $a/d = 3$ (triangles), as well as images of rigid rods (B) of $l/d = 2.5$ (filled circles), $l/d = 5$ (triangles), and $l/d = 20$ (filled squares). Zero value for a/d implies point-like fluorescent bodies. The solid lines indicate the expected decay of the correlation function assuming point sources [Eq. (6.6)]. The figure illustrates the deviation of the correlation function from the expected decay as the fluorescent bodies increase in size.

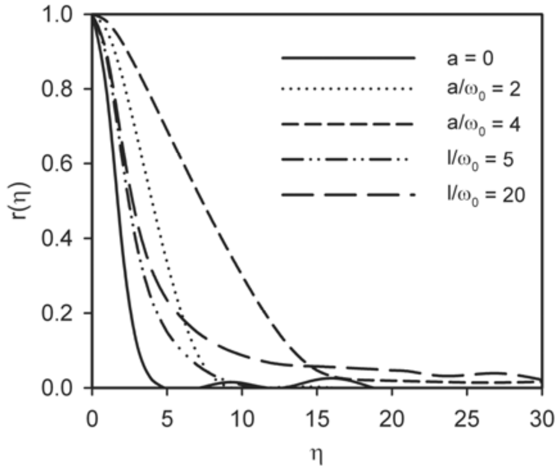

Figure 6.3: Typical normalized one-dimensional spatial correlation function $r(0,\eta,0)$ from simulated images of different geometries and sizes. The case of $a=0$ (solid line) corresponds to images of point sources, which has been convoluted with a Gaussian PSF of d = 2 pixels and η is in the unit of pixel lag.

In contrast, in the template analysis, we use Eq. (6.9) to obtain the Gaussian width $d_f(\tau)$ from the raw $r(\xi,\eta,\tau)$ for $\tau>0$ using the "template", $r(\xi,\eta,0)$, obtained from the data at zero time lag. Theoretically, $d_f(\tau)$ should evolve as $4D\tau$ for two-dimensional free diffusion [Eq. (6.10)]. Template analyses of the $r(\xi,\eta,\tau)$ data from images of various fluorescent body geometries and sizes confirm this supposition, as shown in Figure 6.4. Regardless of fluorophore configuration within the fluorescent bodies and the size of the bodies, the extracted $d_f(\tau)$ closely follows the predicted behavior.

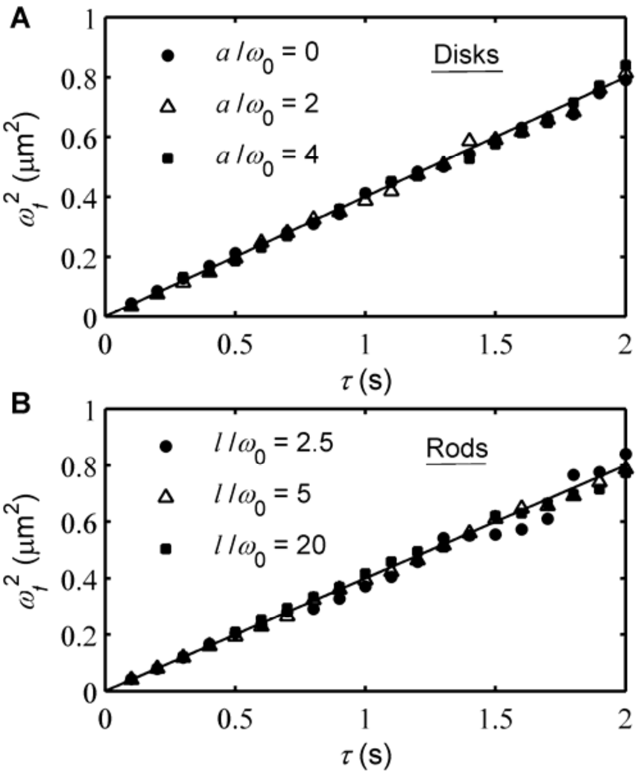

Figure 6.4: Template analysis of images of different fluorescent bodies. The data for $d_f(\tau)$ were obtained by fitting the spatial correlation function $r(\xi,\eta,\tau)$ for each $\tau > 0$ with template of $r(\xi,\eta,0)$ using Eq. (6.9). The results were plotted for images of disks (A) of $a/d = 0$ (filled circles), $a/d = 2$ (triangles), and $a/d = 4$ (filled squares), as well as images of rigid rods (B) of $l/d = 2.5$ (filled circles), $l/d = 5$ (triangles), and $l/d = 20$ (filled squares). Zero value for a/d implies point-like fluorescent bodies. The solid lines indicate a slope of $4D$ expected for pure 2D diffusion. Unlike the correlation function $g(\tau)$ used in the standard analysis, all of the $d_f(\tau)$ values fall on the theoretically expected line regardless of fluorophores configurations.

We now compare how well the standard analysis and the template analysis can predict diffusivity of particles of different geometries and sizes. In Figure 6.5, we plot the result of both types of analyses against the known (“input”) diffusivity D_{in}. It can be observed that the results based on the template analysis are in excellent agreement with the input value of D_{in} for all configurations tested, while standard analysis results deviate strongly from the input value for large values of a/d and l/d. This result supports the robustness of the proposed template analysis. Interestingly, for large values of a/d and l/d, the standard analysis seems to overestimate particle diffusivity. This is in contrast to our previous remark that the $g(\tau)$ data for these cases seem to decay more slowly, which should have led to lower diffusion coefficients. It is useful to consider why this apparent contradiction occurs. Standard analysis uses Eq. (6.8), which includes the temporal offset $g_{t,\infty}$, to obtain τ_D, which is required to calculate D using Eq. (6.5). The presence of $g_{t,\infty}$ in Eq. (6.8) is useful in many cases to eliminate the effect of background signal, and, in the present study, it is helpful in obtaining good result for disk-shaped particles even up to $a/d = 4$. However, it also allows extended variability in τ_D during the fitting process, and this variability causes the overestimation as well as the large standard deviation for the diffusion coefficient for large probes. Indeed, when the offset is taken to be zero, as in the no-offset standard analysis in Figure 6.5, the diffusion coefficient is in fact consistently underestimated, as one would expect because of the slower decay of the temporal correlation function (see Figure 6.2). It is interesting to note that the no-offset standard analysis performs better for larger particles than the standard analysis, in the case of simulated data. This is consistent with the fact that the offset is not needed for the simulated data because of the absence of background and other extraneous noises. The effect of probe size, which manifests in both the spatial and temporal correlation functions (Figure 6.2 and Figure 6.3), on the diffusivity measurement is also evident in Figure 6.5. When point-like template is assumed, the diffusion coefficient is increasingly overestimated with the size of the probes. Overall, the template analysis proposed in this paper provides one the most reliable interpretations of ICS measurements for various probe sizes and shapes.

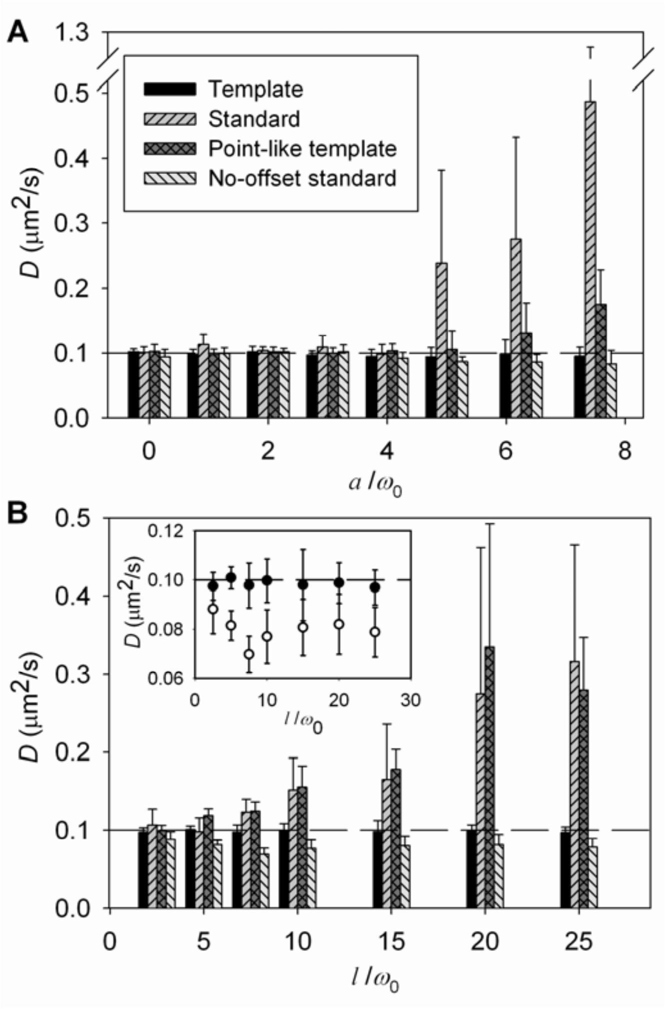

Figure 6.5: Comparison between standard analysis and template analysis analyses for ICS. The diffusion coefficient D for template analysis was obtained from the slope of the d_f vs. τ graph. In the standard analysis, D was obtained by fitting the $g(\tau)$ data to Eq. (6.6) and using the relation $D = d_0^2/4\tau_D$ [Eq. (6.5)]. Point-like template analysis uses theoretical point-like spatial correlation function in place of the experimental template, and no-offset standard analysis takes the offset to be zero. The horizontal dashed lines indicate the input diffusion coefficient D_{in} = 0.1 μm^2/s. ICS analyses of images for both disks of various sizes a (A) and rigid rods of various lengths l (B) using template analysis provide better results than all the other analyses. This effect is especially intensified for large values of a/d and l/d. The inset highlights the consistent underestimation in D obtained using no-offset standard analysis (open circles) as compared to D obtained using template analysis (filled circles). The error bars indicate standard deviations.

6.4.2 Probe-independent ICS on confocal images

To compare our approach with actual ICS experiments, we performed standard confocal imaging on diffusing microspheres in aqueous solutions of glycerol. Aqueous glycerol solutions are simple Newtonian fluids, and the viscosity of the glycerol solutions as a function of concentration and temperature is well-known [159]. These solutions therefore serve as a convenient medium to test how different types of ICS analyses can be used to predict the diffusive properties of microspheres of various sizes. In the present work, we used three different sizes of fluorescent microspheres (diameters $2a$ of 0.5 μm, 1 μm, and 2 μm). These probe sizes are significantly larger than the confocal focus size of our imaging system, which we independently measured to be $d = 0.255 \pm 0.002$ μm. Figure 6.6(A–C) show examples of confocal images of these microspheres taken for ICS analysis. Similar to what we found in our simulations (Figure 6.3), the form and size of the spatial correlation function obtained from these confocal images depend on the size of the probes used. In Figure 6.6(D–F), we show the templates we obtained from the three image sequences, and these templates are used in the subsequent template analysis.

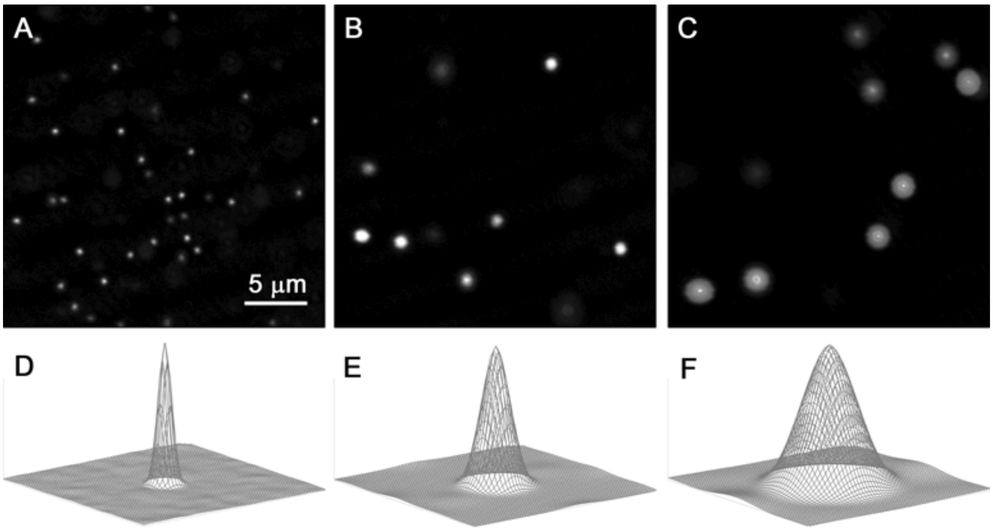

Figure 6.6: Images of fluorescent microspheres of different sizes suspended in glycerol solutions and the corresponding templates used in ICS analysis. The diameters of the microspheres are 0.5 µm (A), 1 µm (B), and 2 µm (C), corresponding to a/d values of approximately 0.98, 1.96, and 3.92, respectively. The templates (D-F) are obtained from the $r(\xi,\eta,0)$ data, averaged over all τ. Not unexpectedly, the width of the templates increases with the size of the fluorescent microspheres. These templates are then used to analyze the raw $r(\xi,\eta,\tau)$ data to obtain the diffusion coefficients.

We performed both standard and template analyses for the image sequences of these three microspheres and calculated the resulting diffusion coefficients. For easy assessment, we plot Da in Figure 6.7, which should be constant for a medium of fixed viscosity [*cf*. Eq. (4.3)]. While both analyses successfully predict the theoretical diffusion coefficient for 0.5 µm and 1 µm microspheres, the result based on the standard analysis significantly differs from the expected value for the 2 µm microspheres ($a/d \sim 4$). It should be noted that the standard analysis here was done assuming two-dimensional diffusion [Eq. (5.6)], which does not completely represent the full three-dimensional diffusion of the microspheres in the medium, as has been previously hinted [152]. The functional form of $g(\tau)$ for three-dimensional diffusion has been formulated previously [185]. Even when this functional form is used, however, the standard analysis still does not result in an accurate determination of the resulting diffusivity (data not shown). We also performed point-like template analysis as well as no offset standard analysis for the experimental data, as shown in Figure 6.7, and these two analyses also do not give as good estimates for D as template analysis does. The experimental data presented here and the results based on the template analysis confirm the usefulness of template analysis, especially for large fluorescent bodies, to investigate dynamic processes using ICS.

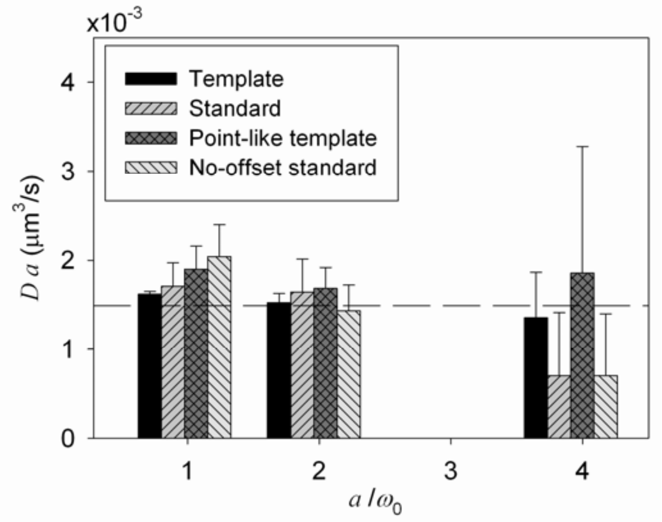

Figure 6.7: Comparison between template and standard analyses for ICS measurements of the fluorescent images of microspheres with different diameters. For easy assessment, the result is plotted as Da, which in theory should be constant for the same medium viscosity ν. The horizontal dashed line indicates the expected value for Da calculated using the Stokes-Einstein relation $Da = k_B T / 6\pi\nu$ [Eq. (4.3)]. Template analysis proves to provide results closer to the expected value compared to standard analysis, especially at the largest tested a/d value. The error bars indicate the standard deviations.

6.5 Discussion

As we have shown in Figure 6.5 and Figure 6.7, beyond a certain threshold value for the probe size, the point-source assumption for the probe particles fails to describe the decay of the correlation function in ICS sufficiently accurately. In cases tested in this study, for two-dimensional disks and three-dimensional microspheres, the threshold value of a/d is around 3 to 4. If one is not aware of the above effect of the size of the probe particles, incorrect conclusions about particle diffusivity could be drawn from the data, both empirically and numerically, as we have shown. In this respect, template analysis has proven to be able to solve the problem. In principle, one can attempt to derive the analytical decay function for any probe geometry, and the experimental correlation data can be fit to the derived function to obtain diffusive properties. This, however, assumes that the fluorophore distribution within each fluorescent body is uniform and known beforehand, a condition that is rather hard to satisfy experimentally. In addition, each particle geometry and fluorophore distribution requires a separate analytical $g(\tau)$. Therefore, it is not easy to obtain a robust, generic functional form for $g(\tau)$. In contrast, the proposed template analysis circumvents this problem by taking any arbitrary spatial correlation of the convolution of geometry of the probes and the fluorophore distribution within the probe as the template against which the full spatiotemporal correlation data can be analyzed to obtain the dynamic properties.

Despite the robustness of template analysis, as demonstrated above, there are still a few aspects that we have not addressed. First, we have only derived and validated the use of template analysis for two-dimensional diffusion. From a biological point of view, two-dimensional systems do cover many important biochemical processes occurring, for example, in the cell membrane. The analysis we present here can nevertheless be extended to enable template analysis for three-dimensional systems. Such a development may gain many potential applications due to the capability of confocal microscopy to perform time-lapsed three-dimensional imaging. In one part of our simulations, we took a rather extreme case of randomly oriented fluorescent bodies, where the fluorophores are situated in a rigid rod configuration. This case is useful for simulating a situation where fluorophores form domains that are distinct from each other. In some experiments, however, these domains are distinct not only from each other in their orientation, but also in their size and spatial distribution of the fluorophores, thus effectively representing multiple populations. One way to address this question is by noting that in the template analysis [Eq. (6.9)], $d_f\left(\tau\right)$ is obtained independently for each τ evaluated. Thus, in principle, D in Eq. (6.10) can be analyzed at different time-scales, allowing diffusional analysis of multiple species. In addition, we only allowed translational diffusion of these fluorescent bodies. While probe rotation will not affect the template, it will influence the manner in which the template decays, which is not well understood yet. Considering its many potential applications, it may be beneficial to understand how rotational diffusion affects ICS results, especially in the presence of multiple populations described above [186].

In summary, we have developed an alternative method for analysis of ICS data that circumvents the need to assume point-like probes or uniform distribution of fluorophores on the probes. We have demonstrated the robustness of this probe-independent method by comparing it to the conventional method for simulated as well as experimental image sequences of fluorescent bodies of various geometries and sizes. We found that probe size begins to influence the extracted information when it is about 3 to 4 times the confocal focus size. In particular, as the probe size becomes larger, the spatial correlation function becomes broader and, correspondingly, the decay of the temporal correlation function becomes slower. For such large particles, the extracted diffusion coefficient can become too small to measure if the size of the large particle is not taken into account, such as in the standard analysis. This spatio-temporal interrelation in the correlation function has not previously been attended to, and we have shown that simply assuming point sources yields inaccurate diffusivity measurements. Template analysis should therefore help in obtaining dynamic properties from ICS data whenever the presence of large domains of fluorophores is suspected. Indeed, since template analysis works just as well in the case of point sources, as we have verified, its use in most ICS experiments can only be beneficial.

Chapter 7: Conclusions and Outlook

7.1 Summary

The classical interdisciplinary boundary between physics, mathematics, chemistry, cell biology, mechanical engineering, chemical engineering, and bioengineering has somewhat blurred when studies of soft matter are concerned. And it is for good reasons. This thesis has shown the importance of looking at this fascinating class of material from multiple perspectives and at multiple length scales and time scales. The unifying theme of the present work is that a combination of different mechanical characterization methods, from experimental rheology, microrheology, and spectroscopy to computational and theoretical modeling, can yield powerful insights into the working mechanisms of soft materials. Specifically, in the first half of this thesis, we studied in detail the mechanical behavior of collagen networks as a popular choice of soft biopolymer matrix in different strain levels as well as length and time scales. Knowing the limitations of current characterization techniques, in the second half of this thesis we went on to develop a new, image-based microrheological technique that can tackle some of these limitations.

In the work on the macroscopic rheology of collagen networks presented in Chapter 2, we have shown how proper interpretations of rheological measurements can be used to explain the mechanical behavior of the networks. We started by carefully analyzing the network response to strain amplitude-dependent oscillatory shear deformation and found rich mechanical behavior, including early strain-stiffening at small strains, which has been hitherto masked by overall intercycle strain-softening behavior. Analysis of the relation between the nonlinear behavior and the polymer concentration revealed the presence of weak cross-link–like interactions within the network, even without additional, external cross-linkers. Consequently, we found that the mechanical behavior of pure collagen networks can be well described by the cross-linked semiflexible polymer network model, rather than another model based only on physical fiber entanglements. By using different measurement protocols, we also examine the reversibility and the temporal properties of these cross-links. Similar lines of analysis can thus be used to better understand the origin of the mechanical behavior of other soft matter systems.

While rheological studies can yield many important insights, we wanted to investigate the role of structure on the resulting network mechanics more closely, which lead us to the computational study presented in Chapter 3. We realized that the phenomenological universality of many biopolymer networks would allow us to generalize the simulations to the semiflexible polymer class of materials, thus making the work relevant to various fields. Through this bottom-up approach, we identify two structural parameters, quantifying network connectivity and entanglement, which are responsible for the resulting network mechanics at multiple length scales of observation and strain levels. Importantly, these two network structural parameters were found to be associated with the predominant network deformation mechanisms that have been proposed in earlier studies. Furthermore, these associations between network structure and length-scale as well as strain-dependent mechanics can explain previous experimental and computational observations regarding the affinity of network deformation and the effect of mechanical heterogeneity within the networks. The simple and adaptable model used also allows further explorations on the role of other structural parameters.

To characterize the microscale mechanical properties of collagen networks experimentally, we performed particle tracking microrheology (PTM) and presented the results in Chapter 4. We introduced the concept of microrheology and discussed the principle of PTM technique. The PTM results on collagen showed dramatic discrepancies with bulk mechanical rheology results. First, the magnitude of the elastic modulus is much smaller than that found in mechanical rheology. Second, there is considerable variation of the elastic modulus (over three orders of magnitude) even within each sample. These observations suggest the presence of local variation of network stiffness, and that a macro-level measurement only provides overall properties without providing information on the small scales, which are likely to be relevant in the contexts of living cells. We also discussed the technical difficulties and current limitations of the technique that lead us to the second half of the thesis.

We dedicate the second half of the thesis to the development and description of a new microrheological technique based on image correlation spectroscopy (ICS). In Chapter 5, we introduced the concept of ICS and its applications in biophysical fields to date. We presented the theoretical framework for extracting the time-dependent diffusivity of the probes and the desired microrheological information. The method was then tested using both ideal (Newtonian) fluids of different viscosities and complex fluids (soft matter) of different viscoelastic behaviors. We obtain excellent agreement between the method, ICS-μR. In addition, we also presented a method to extract both the probe mean-squared displacement (MSD) and its logarithmic derivative, which are required for the subsequent microrheological calculations, from correlation data. The method was validated on several, representative reported data on various soft matter systems. This robust method, which is based on the assumption of smoothly varying local power law of the MSD, can thus be used to improve the quality of the data even for other microrheological techniques. The accessible length- and time-scales in ICS-μR are comparable to, if not better than, current microrheological techniques. However, ICS-μR holds the potential of performing microrheological measurements using indigenous probes with much larger ranges of size and density, thus making it more amenable to many applications.

We realized that in many of the potential applications of ICS, the probe size and shape vary (and are often unknown), especially when indigenous particles are used as the microrheological markers. Without properly accounting for the probe size and shape, erroneous conclusions could be drawn from the correlation data. In Chapter 6, we present a mathematical formulation that can circumvent this problem. In a nutshell, the temporal decay of the entire spatial correlation function, as opposed to just the peak of it as conventionally done in standard ICS measurements, is analyzed to obtain the probe MSD. This spatial correlation function contains useful information on the spatial distribution of both the fluorescent bodies as well as the fluorophores within each body. We validated the method both on simulated images and experimental confocal images of fluorescent particles of different sizes and shapes.

7.2 Future Directions

In this section, we describe potential new directions and avenues of research for the works in this thesis. These encompass both further exploitation of the methods (*e.g.*, imaging, mechanical rheology, microrheology, computer simulations) and the class of materials [soft matter system, *e.g.*, (bio)polymer networks] we have considered.

7.2.1 Characterization of evolving soft matter

In our study on polymer networks, we learned how the microstructure of the networks heavily determines the resulting mechanical properties. In all systems considered in this thesis, however, the materials of interest are under equilibrium condition: they are stationary in time. It would be equally interesting to study the structural and mechanical properties of soft matter far from equilibrium. This situation is in fact very often encountered.

- The self-assembly and gelation processes of polymer networks involves temporal change of structure (and hence mechanical properties) towards equilibrium state.
- Biopolymer networks are remarkably "active". As an example, cells constantly remodel their cytoskeletal organization through modulation of active cross-linkers and molecular motors [125,187].
- Suspension of small particles or bacteria can be an active system, wherein the particles constitute an active fluid microstructure driven out of equilibrium

through active internal forces.

- Soft glassy materials such as nanotube gels can rejuvenate itself under deformation, leading to the classification of "self-healing" materials [188]. In fact, we have shown in Chapter 2 that even collagen networks show indications of temporal restructuring towards equilibrium when sheared.

While the implications of these processes are obviously far-reaching, the detailed structural mechanism is still not well understood. A combination of characterization techniques probing different length and time scales, such as that described in this thesis, would likely be necessary to gain better understanding.

7.2.2 The role of other structural variables on the mechanics of semiflexible polymer networks

In our computational study of the nonlinear mechanics of 3D cross-linked semiflexible polymer networks, we have used a highly simplified simulated network model to isolate the role of network structure. Although this simple model proved to provide many valuable insights on the structural origin of the nonlinear behavior in 3D, further investigations on the other structural variables will help more quantitative comparison to previous experimental and theoretical works. In particular, future studies are expected to encompass:

- Fiber morphology. Previous works have mostly focused on the effect of polymer and cross-linker concentration on the bulk mechanics. However, individual fiber length L, diameter d, and bundling mechanisms (which alter l_p) can also modify local fiber interaction and network connectivity, which have profound influence on the network mechanics, as we show in Chapter 3.

- The relative importance of nonlinear force-extension relation of individual fibers and network rearrangement. This aspect of the network mechanics has been long debated, but is still inconclusive. On the ground of our findings in Chapter 3, we speculate that the relative importance is a function of network structural properties and length scale of observation. This hypothesis can be tested, for example, by varying the functional form of U_s as the network structural features through R_e and R_{cl}.
- The cross-linker properties. *In vivo*, it is known that different cross-linkers have different cross-linking properties and machineries. Some cross-linkers are long while some others have zero effective distance; some are stiff while some others are flexible; some prefer to bundle fibers while some others prefer to form random meshwork junctions. The effect of these variations on the overall network mechanics can be simulated by varying the effective functional form of U_{cl} and the cross-linker properties k_{cl} and δ_0.
- To further imitate experimental networks, a distribution of the fiber dimension can also be introduced in the networks. This distribution can add a new dimension to network heterogeneity and modes of strain transmission.

7.2.3 Probe-material interaction

The quality and interpretation of PTM results depend heavily on the interaction between the material being examined and the probe used to perform the measurements. Physical interaction can alter the local environment, for example through development of depletion zones around the probes [189,190]. The probe mobility, in turn, has been shown to depend sensitively on the local material environment [191]. Chemical interactions also play central role in determining the coupling between the probe and the elastic network. For instance, when adsorption of the probes to the surrounding network is prevented, the probes are found to diffuse freely and do not report the elastic properties of the network [170,192,193]. This effect can further lead to problems with probe slippage, both in translation and rotation, which may or may not reflect material deformation [194,195]. While these problems have been hypothesized and recognized, systematic studies to find the 'ideal' conditions and extents of probe-material interactions (*e.g.*, the presence, type, and amount of additional chemical or physical cross-linking between the probe and the material) or whether the interactions can in fact be utilized to provide useful information are lacking.

Another aspect of microrheology that warrants further exploration is the possibility of conducting more specific and targeted measurements of the local material viscoelasticity. At its current state, PTM measurement acts only as a blind reporter of the surrounding environment. This statement can be better illustrated in the following two sample cases:

- Currently, PTM has no way of distinguishing the source of the measured stiffness: whether it is contributed by the viscoelasticity of the network or the individual fibers immediately surrounding the probes. To examine this effect, a study can be done where the elastic contribution is varied (through variation of fiber and/or cross-linker density) and the resulting probe mobility and microrheological measurements are analyzed correspondingly.

- The probe mobility is also affected by the presence of objects located further away from the immediate surrounding of the probes. These objects, whose stiffness may still be sensed far away and may affect local strain transmission through the material, can take the form of other probes, living cells (when studying the microrheology of extracellular matrices), cellular organelles (when studying intracellular microrheology), and even walls (the experimental boundary to which the network is anchored). This brings up the importance of understanding the depth of sensing of the probes and the extent of material homogeneity, which are very relevant in cell studies, where the length scales of relevance are likely to coincide with the length scales of probe sensing. One way to examine this effect is by studying the effect of the presence of movable objects (*e.g.*, microspheres, microneedles, wall, etc) on the probe motion as a function of distance.

The research directions suggested above would not only improve our understanding of probe-material interaction but also provide new interpretations of local microrheology in, for example, studies on cell behavior as a function of different substrate rigidity, both in 2D and 3D [45,196]. Furthermore, these studies can also help answer an outstanding question in cell biology of how and how deep cells can feel their outside and inside environments [197,198].

7.2.4 Probeless microrheology

As we have mentioned in Section 5.1.1, many of the problems faced by the current microrheological techniques arise from the use of external probes that have to be introduced as the mechanical markers in the materials of interest. One way to circumvent these probe-associated problems is by using indigenous particles, instead of external probes, as the markers. Indeed, researchers have recently explored the idea of using naturally occurring, visible markers such as lipid granules to study the cytoplasmic diffusion properties and microrheological properties of living cells [172,199]. As we have proposed in Chapter 5, ICS also has the potential of performing such probeless microrheological measurements. ICS has been used to quantify the spatial and temporal intracellular proteins localization and dynamics just based on the fluorescent image time series of these proteins [153,200,201], and, through our ICS-μR approach described in Chapter 5, desired microrheological information can be readily obtained.

There are, however, some technical issues that need to be addressed before probeless microrheology can be realized reliably. We have started addressing the problem of dealing with probes of unknown size and shapes by proposing a new method of ICS analysis based on the spatial correlation function in Chapter 6. Although this method can in principle take care of any type of translational diffusion of arbitrarily shaped objects (or populations of objects) in 3D, we have not considered rotational diffusion, which can take place concurrently. Modified theoretical models describing the evolution of the spatiotemporal correlation function $r\left(\xi,\eta,\tau\right)$ would need to be derived, incorporating rotational motion of the fluorescent bodies. The accuracy of the extracted MSD data would need to be improved too, since it is likely that larger fluorescent bodies would move more slowly, leading to small MSD.

As the field emerges in the future, we foresee that these questions and problems will be tackled to cater for the various applications made possible by these techniques.

Bibliography

[1] Gompper, G. and M. Schick, editors. 2006. Soft Matter, Vol. 1: Polymer Melts and Mixtures. Weinheim, Germany: Wiley-VCH.

[2] Jones, R. A. L. 2008. Soft Condensed Matter. Oxford, NY: Oxford University Press.

[3] Hamley, I. W. 2007. Introduction to Soft Matter: Synthetic and Biological Self-Assembling Materials. Chichester, U.K.: John Wiley & Sons, Ltd.

[4] de Gennes, P.-G. 1979. Scaling Concepts in Polymer Physics. Ithaca, NY: Cornell University Press.

[5] Kumar, S. 2007 Pierre-Gilles de Gennes (1932-2007). Chemistry World.

[6] de Gennes, P. G. 1992. Soft matter. *Science* 256:495-497.

[7] Gompper, G. and M. Schick, editors. 2006. Soft Matter, Vol. 2: Complex Colloidal Suspensions. Weinheim, Germany: Wiley-VCH.

[8] Hecht, E. 2002. Optics. Reading, MA: Addison-Wesley.

[9] Mertz, J. 2009. Introduction to Light Microscopy. Greenwood Village, CO: Roberts and Company Publishers.

[10] Schmidt-Mende, L., A. Fechtenkotter, K. Mullen, E. Moons, R. H. Friend, and J. D. MacKenzie. 2001. Self-organized discotic liquid crystals for high-efficiency organic photovoltaics. *Science* 293:1119-1122.

[11] Murphy, D. B. 2001. Differential Interference Contrast (DIC) Microscopy and Modulation Contrast Microscopy. In Fundamentals of Light Microscopy and Electronic Imaging. Wiley-Liss. New York. 153-176.

[12] Herman, B. 1998. Fluorescence Microscopy. Oxford, UK: BIOS Scientific Publishers in association with the Royal Microscopical Society.

[13] Pawley, J. B. 2006. Handbook of Biological Confocal Microscopy. New York: Springer.

[14] Watt, I. M. 1997. The Principles and Practice of Electron Microscopy. New York: Cambridge University Press.

[15] Wiesendanger, R. 1994. Scanning Probe Microscopy and Spectroscopy: Methods and Applications. New York: Cambridge University Press.

[16] Eaton, P. 2010. Atomic Force Microscopy. Oxford: Oxford University Press.

[17] Fischer-Cripps, A. C. 2011. Nanoindentation. New York: Springer.

[18] Morrison, F. A. 2001. Understanding Rheology. New York: Oxford University Press.

[19] Macosko, C. W. 1994. Rheology: Principles, Measurements, and Applications. New York: VCH.

[20] Larson, R. G. 1999. The Structure and Rheology of Complex Fluids. New York: Oxford University Press.

[21] Gardel, M. L., M. T. Valentine, and D. A. Weitz. 2003. Microrheology. In Microscale Diagnostic Techniques. Springer. New York. 1-49.

[22] Kruppa, B., G. Strube, and C. Gerlach. 2001. Light Scattering. In Optical Measurements: Techniques and Applications. F. Mayinger and O. Feldmann,

editors. 2nd ed. Springer. New York. 95-112.

[23] Berne, B. J. and R. Pecora. 1976. Dynamic Light Scattering: With Applications to Chemistry, Biology, and Physics. New York: Wiley.

[24] Roe, R.-J. 2000. Methods of X-ray and Neutron Scattering in Polymer Science. New York: Oxford University Press.

[25] Lovell, R., G. R. Mitchell, and A. H. Windle. 1979. Wide-angle X-ray-scattering study of structural parameters in non-crystalline polymers. *Faraday Discuss.* 68:46-57.

[26] Glatter, O. and O. Kratky. 1992. Small Angle X-Ray Scattering. Waltham, MA: Academic Press.

[27] Furrer, A., J. Mesot, and T. Strassle. 2009. Neutron Scattering in Condensed Matter Physics. Niver Edge, NJ: World Scientific Pub.

[28] Hore, P. J. 1995. Nuclear Magnetic Resonance. New York: Oxford University Press.

[29] Colthup, N. B., L. H. Daly, and S. E. Wiberley. 1990. Introduction to Infrared and Raman Spectroscopy. Boston, MA: Academic Press.

[30] Leach, A. R. 2001. Molecular Modelling: Principles and Applications. Singapore: Pearson Education.

[31] Reddy, J. N. 2006. An Introduction to the Finite Element Method. New York, NY: McGraw-Hill Higher Education.

[32] Shikata, T., S. J. Dahman, and D. S. Pearson. 1994. Rheo-optical behavior of wormlike micelles. *Langmuir* 10:3470-3476.

[33] Schmoller, K. M., P. Fernandez, R. C. Arevalo, D. L. Blair, and A. R. Bausch. 2010. Cyclic hardening in bundled actin networks. *Nat. Commun.* 1:134.

[34] Di Lullo, G. A., S. M. Sweeney, J. Korkko, L. Ala-Kokko, and J. D. San Antonio. 2002. Mapping the ligand-binding sites and disease-associated mutations on the most abundant protein in the human, type I collagen. *J. Biol. Chem.* 277:4223-4231.

[35] Nelson, D. L. and M. M. Cox. 2005. Lehninger Principles of Biochemistry. New York, NY: W. H. Freeman.

[36] Kuivaniemi, H., G. Tromp, and D. J. Prockop. 1991. Mutations in collagen genes: causes of rare and some common diseases in humans. *FASEB J.* 5:2052-2060.

[37] Fratzl, P., editor. 2008. Collagen: Structure and Mechanics. New York, NY: Springer.

[38] Buehler, M. J. 2006. Nature designs tough collagen: explaining the nanostructure of collagen fibrils. *Proc. Natl. Acad. Sci. U.S.A.* 103:12285-12290.

[39] Ott, H. C., T. S. Matthiesen, S. K. Goh, L. D. Black, S. M. Kren, T. I. Netoff, and D. A. Taylor. 2008. Perfusion-decellularized matrix: using nature's platform to engineer a bioartificial heart. *Nat. Med.* 14:213-221.

[40] Gillette, B. M., J. A. Jensen, B. Tang, G. J. Yang, A. Bazargan-Lari, M. Zhong, and S. K. Sia. 2008. In situ collagen assembly for integrating microfabricated three-dimensional cell-seeded matrices. *Nat. Mater.* 7:636-640.

[41] Grinnell, F., L. B. Rocha, C. Iucu, S. Rhee, and H. Jiang. 2006. Nested collagen matrices: a new model to study migration of human fibroblast populations in three dimensions. *Exp. Cell Res.* 312:86-94.

[42] Kaufman, L. J., C. P. Brangwynne, K. E. Kasza, E. Filippidi, V. D. Gordon, T. S. Deisboeck, and D. A. Weitz. 2005. Glioma expansion in collagen I matrices: analyzing collagen concentration-dependent growth and motility patterns. *Biophys. J.* 89:635-650.

[43] Wolf, K., Y. I. Wu, Y. Liu, J. Geiger, E. Tam, C. Overall, M. S. Stack, and P. Friedl. 2007. Multi-step pericellular proteolysis controls the transition from individual to collective cancer cell invasion. *Nat. Cell Biol.* 9:893-904.

[44] Engler, A. J., S. Sen, H. L. Sweeney, and D. E. Discher. 2006. Matrix elasticity directs stem cell lineage specification. *Cell* 126:677-689.

[45] Zaman, M. H., L. M. Trapani, A. L. Sieminski, A. Siemeski, D. Mackellar, H. Gong, R. D. Kamm, A. Wells, D. A. Lauffenburger, and P. Matsudaira. 2006. Migration of tumor cells in 3D matrices is governed by matrix stiffness along with cell-matrix adhesion and proteolysis. *Proc. Natl. Acad. Sci. U.S.A.* 103:10889-10894.

[46] Friedl, P., K. Maaser, C. E. Klein, B. Niggemann, G. Krohne, and K. S. Zänker. 1997. Migration of highly aggressive MV3 melanoma cells in 3-dimensional collagen lattices results in local matrix reorganization and shedding of alpha2 and beta1 integrins and CD44. *Cancer Res.* 57:2061-2070.

[47] Leung, L. Y., D. Tian, C. P. Brangwynne, D. A. Weitz, and D. J. Tschumperlin. 2007. A new microrheometric approach reveals individual and cooperative roles for TGF-beta1 and IL-1beta in fibroblast-mediated stiffening of collagen gels. *FASEB J.* 21:2064-2073.

[48] Donald, A. M. 2007. Why should polymer physicists study biopolymers? *J. Polym. Sci., Part B: Polym. Phys.* 45:3257-3262.

[49] Fung, Y.-C. 1993. Biomechanics: Mechanical Properties of Living Tissues. New York: Springer-Verlag.

[50] Storm, C., J. J. Pastore, F. C. MacKintosh, T. C. Lubensky, and P. A. Janmey. 2005. Nonlinear elasticity in biological gels. *Nature* 435:191-194.

[51] Head, D. A., A. J. Levine, and F. C. MacKintosh. 2003. Distinct regimes of elastic response and deformation modes of cross-linked cytoskeletal and semiflexible polymer networks. *Phys. Rev. E* 68:061907.

[52] Schmidt, C. F., M. Barmann, G. Isenberg, and E. Sackmann. 1989. Chain dynamics, mesh size, and diffusive transport in networks of polymerized actin - a quasielastic light-scattering and microfluorescence study. *Macromolecules* 22:3638-3649.

[53] Bustamante, C., J. F. Marko, E. D. Siggia, and S. Smith. 1994. Entropic elasticity of lambda-phage DNA. *Science* 265:1599-1600.

[54] Wilhelm, J. and E. Frey. 1996. Radial distribution function of semiflexible polymers. *Phys. Rev. Lett.* 77:2581-2584.

[55] Everaers, R., F. Julicher, A. Ajdari, and A. C. Maggs. 1999. Dynamic fluctuations of semiflexible filaments. *Phys. Rev. Lett.* 82:3717-3720.

[56] Gittes, F. and F. C. MacKintosh. 1998. Dynamic shear modulus of a semiflexible polymer network. *Physical Review E* 58:R1241-R1244.

[57] Odijk, T. 1983. On the statistics and dynamics of confined or entangled stiff polymers. *Macromolecules* 16:1340-1344.

[58] Isambert, H. and A. C. Maggs. 1996. Dynamics and rheology of actin solutions. *Macromolecules* 29:1036-1040.

[59] Morse, D. C. 1998. Viscoelasticity of concentrated isotropic solutions of semiflexible polymers. 2. Linear response. *Macromolecules* 31:7044-7067.

[60] Hinner, B., M. Tempel, E. Sackmann, K. Kroy, and E. Frey. 1998. Entanglement, elasticity, and viscous relaxation of actin solutions. *Phys. Rev. Lett.* 81:2614-2617

[61] Morse, D. C. 1998. Viscoelasticity of tightly entangled solutions of semiflexible polymers. *Physical Review E* 58:R1237-R1240.

[62] Forgacs, G., S. A. Newman, B. Hinner, C. W. Maier, and E. Sackmann. 2003. Assembly of collagen matrices as a phase transition revealed by structural and rheologic studies. *Biophys. J.* 84:1272-1280.

[63] Christiansen, D. L., E. K. Huang, and F. H. Silver. 2000. Assembly of type I collagen: fusion of fibril subunits and the influence of fibril diameter on mechanical properties. *Matrix Biol.* 19:409-420.

[64] Parekh, A. and D. Velegol. 2007. Collagen gel anisotropy measured by 2-D laser trap microrheometry. *Ann. Biomed. Eng.* 35:1231-1246.

[65] Yang, Y.-l. and L. J. Kaufman. 2009. Rheology and confocal reflectance microscopy as probes of mechanical properties and structure during collagen and collagen/hyaluronan self-assembly. *Biophys. J.* 96:1566-1585.

[66] Roeder, B. A., K. Kokini, and S. L. Voytik-Harbin. 2009. Fibril microstructure affects strain transmission within collagen extracellular matrices. *J. Biomech. Eng.* 131:031004.

[67] Sander, E. A., T. Stylianopoulos, R. T. Tranquillo, and V. H. Barocas. 2009. Image-based multiscale modeling predicts tissue-level and network-level fiber reorganization in stretched cell-compacted collagen gels. *Proc. Natl. Acad. Sci. U.S.A.* 106:17675-17680.

[68] Vader, D., A. Kabla, D. Weitz, and L. Mahadevan. 2009. Strain-induced alignment in collagen gels. *PLoS ONE* 4:e5902.

[69] Friedl, P. and E. B. Bröcker. 2000. The biology of cell locomotion within three-dimensional extracellular matrix. *Cell. Mol. Life Sci.* 57:41-64.

[70] Friedl, P. 2004. Dynamic imaging of cellular interactions with extracellular matrix. *Histochem. Cell Biol.* 122:183-190.

[71] Wolf, K. and P. Friedl. 2005. Functional imaging of pericellular proteolysis in cancer cell invasion. *Biochimie* 87:315-320.

[72] Stein, A. M., D. A. Vader, L. M. Jawerth, D. A. Weitz, and L. M. Sander. 2008. An algorithm for extracting the network geometry of three-dimensional collagen gels. *J. Microsc.* 232:463-475.

[73] Yang, Y.-l., L. M. Leone, and L. J. Kaufman. 2009. Elastic moduli of collagen gels can be predicted from two dimensional confocal microscopy. *Biophys. J.*

97:2051-2060.

[74] Raub, C. B., V. Suresh, T. Krasieva, J. Lyubovitsky, J. D. Mih, A. J. Putnam, B. J. Tromberg, and S. C. George. 2007. Noninvasive assessment of collagen gel microstructure and mechanics using multiphoton microscopy. *Biophys. J.* 92:2212-2222.

[75] Jawerth, L. M., S. Munster, D. A. Vader, B. Fabry, and D. A. Weitz. 2009. A blind spot in confocal reflection microscopy: the dependence of fiber brightness on fiber orientation in imaging biopolymer networks. *Biophys. J.* 98:L1-3.

[76] Yang, Y.-l., S. Motte, and L. J. Kaufman. 2010. Pore size variable type I collagen gels and their interaction with glioma cells. *Biomaterials* 31:5678-5688.

[77] Raub, C. B., J. Unruh, V. Suresh, T. Krasieva, T. Lindmo, E. Gratton, B. J. Tromberg, and S. C. George. 2008. Image correlation spectroscopy of multiphoton images correlates with collagen mechanical properties. *Biophys. J.* 94:2361-2373.

[78] Raub, C. B., A. J. Putnam, B. J. Tromberg, and S. C. George. 2010. Predicting bulk mechanical properties of cellularized collagen gels using multiphoton microscopy. *Acta Biomater.* 6:4657-4665.

[79] Friedl, P. and E. B. Bröcker. 2001. Biological confocal reflection microscopy: Reconstruction of three-dimensional extracellular matrix, cell migration, and matrix reorganization. In Image Analysis: Methods and Applications. D.-P. Häder, editor. 2nd ed. CRC Press. Boca Raton, FL.

[80] Keller, H. E. 1995. Objective lenses for optical microscopy. In Handbook of Biological Confocal Microscopy. J. B. Pawley, editor. Plenum Press. New York. 111-126.

[81] Anand, S., J. H. Wu, and S. L. Diamond. 1995. Enzyme-mediated proteolysis of fibrous biopolymers: Dissolution front movement in fibrin or collagen under conditions of diffusive or convective transport. *Biotechnol. Bioeng.* 48:89-107.

[82] Arevalo, R. C., J. S. Urbach, and D. L. Blair. 2010. Size-dependent rheology of type-I collagen networks. *Biophys. J.* 99:L65-67.

[83] Knapp, D. M., V. H. Barocas, A. G. Moon, K. Yoo, L. R. Petzold, and R. T. Tranquillo. 1997. Rheology of reconstituted type I collagen gel in confined compression. *J. Rheol.* 41:971-993.

[84] Lin, Y.-C., G. H. Koenderink, F. C. MacKintosh, and D. A. Weitz. 2007. Viscoelastic properties of microtubule networks. *Macromolecules* 40:7714-7720.

[85] Schopferer, M., H. Bar, B. Hochstein, S. Sharma, N. Mucke, H. Herrmann, and N. Willenbacher. 2009. Desmin and vimentin intermediate filament networks: their viscoelastic properties investigated by mechanical rheometry. *J. Mol. Biol.* 388:133-143.

[86] Gardel, M. L., F. Nakamura, J. H. Hartwig, J. C. Crocker, T. P. Stossel, and D. A. Weitz. 2006. Prestressed F-actin networks cross-linked by hinged filamins

replicate mechanical properties of cells. *Proc. Natl. Acad. Sci. U.S.A.* 103:1762-1767.

[87] Wilhelm, M. 2002. Fourier-Transform rheology. *Macromol. Mater. Eng.* 287:83-105.

[88] Ewoldt, R. H., A. E. Hosoi, and G. H. McKinley. 2008. New measures for characterizing nonlinear viscoelasticity in large amplitude oscillatory shear. *J. Rheol.* 52:1427-1458.

[89] Sivakumar, L. and G. Agarwal. 2010. The influence of discoidin domain receptor 2 on the persistence length of collagen type I fibers. *Biomaterials* 31:4802-4808.

[90] Morse, D. C. 1998. Viscoelasticity of concentrated isotropic solutions of semiflexible polymers. 1. Model and stress tensor. *Macromolecules* 31:7030-7043.

[91] Landau, L. D. and E. M. Lifshitz. 1986. Theory of Elasticity. Oxford: Pergamon Press.

[92] Yang, L., K. O. van der Werf, B. F. J. M. Koopman, V. Subramaniam, M. L. Bennink, P. J. Dijkstra, and J. Feijen. 2007. Micromechanical bending of single collagen fibrils using atomic force microscopy. *J. Biomed. Mater. Res. A* 82A:160-168.

[93] Sun, W. 2010. Cancer cell migration in 3D collagen gel matrix system [PhD Thesis]. Singapore: National University of Singapore.

[94] MacKintosh, F. C., J. Käs, and P. A. Janmey. 1995. Elasticity of semiflexible biopolymer networks. *Phys. Rev. Lett.* 75:4425-4428.

[95] Blundell, J. R. and E. M. Terentjev. 2009. Stretching semiflexible filaments and their networks. *Macromolecules* 42:5388-5394.

[96] Colby, R. H., M. Rubinstein, and J. L. Viovy. 1992. Chain entanglement in polymer melts and solutions. *Macromolecules* 25:996-998.

[97] Raeber, G. P., M. P. Lutolf, and J. A. Hubbell. 2005. Molecularly engineered PEG hydrogels: a novel model system for proteolytically mediated cell migration. *Biophys. J.* 89:1374-1388.

[98] Gardel, M. L., J. H. Shin, F. C. MacKintosh, L. Mahadevan, P. Matsudaira, and D. A. Weitz. 2004. Elastic behavior of cross-linked and bundled actin networks. *Science* 304:1301-1305.

[99] Mullins, L. 1969. Softening of rubber by deformation. *Rubber Chem. Technol.* 42:339-362.

[100] Chaudhuri, O., S. H. Parekh, and D. A. Fletcher. 2007. Reversible stress softening of actin networks. *Nature* 445:295-298.

[101] Stein, A. M., D. A. Vader, D. A. Weitz, and L. M. Sander. 2010. The micromechanics of three-dimensional collagen-I gels. *Complexity* 16:22-28.

[102] Grinnell, F. 2003. Fibroblast biology in three-dimensional collagen matrices. *Trends Cell Biol.* 13:264-269.

[103] Grinnell, F., M. Zhu, M. A. Carlson, and J. M. Abrams. 1999. Release of mechanical tension triggers apoptosis of human fibroblasts in a model of regressing granulation tissue. *Exp. Cell Res.* 248:608-619.

[104] Eastwood, M., V. C. Mudera, D. A. McGrouther, and R. A. Brown. 1998. Effect of precise mechanical loading on fibroblast populated collagen lattices: morphological changes. *Cell Motil. Cytoskeleton* 40:13-21.

[105] Sander, E. A., A. M. Stein, M. J. Swickrath, and V. H. Barocas. 2010. Out of many, one: Modeling schemes for biopolymer and biofibril networks. In Trends in Computational Nanomechanics: Transcending Length and Time Scales. T. Dumitrica, editor. Springer. 557-602.

[106] Huisman, E. M., T. van Dillen, P. R. Onck, and E. van der Giessen. 2007. Three-dimensional cross-linked f-actin networks: relation between network architecture and mechanical behavior. *Phys. Rev. Lett.* 99:208103.

[107] Onck, P. R., T. Koeman, T. van Dillen, and E. van der Giessen. 2005. Alternative explanation of stiffening in cross-linked semiflexible networks. *Phys. Rev. Lett.* 95:178102.

[108] Wilhelm, J. and E. Frey. 2003. Elasticity of stiff polymer networks. *Phys. Rev. Lett.* 91:108103.

[109] Head, D. A., A. J. Levine, and F. C. MacKintosh. 2003. Deformation of cross-linked semiflexible polymer networks. *Phys. Rev. Lett.* 91:108102.

[110] Heussinger, C. and E. Frey. 2006. Stiff polymers, foams, and fiber networks. *Phys. Rev. Lett.* 96:017802.

[111] Shin, J. H., M. L. Gardel, L. Mahadevan, P. Matsudaira, and D. A. Weitz. 2004. Relating microstructure to rheology of a bundled and cross-linked F-actin network in vitro. *Proc. Natl. Acad. Sci. U.S.A.* 101:9636-9641.

[112] Wyart, M., H. Liang, A. Kabla, and L. Mahadevan. 2008. Elasticity of floppy and stiff random networks. *Phys. Rev. Lett.* 101:215501.

[113] Lindström, S. B., D. A. Vader, A. Kulachenko, and D. A. Weitz. 2010. Biopolymer network geometries: characterization, regeneration, and elastic properties. *Phys. Rev. E* 82:051905.

[114] Kasza, K. E., G. H. Koenderink, Y. C. Lin, C. P. Broedersz, W. Messner, F. Nakamura, T. P. Stossel, F. C. MacKintosh, and D. A. Weitz. 2009. Nonlinear elasticity of stiff biopolymers connected by flexible linkers. *Phys. Rev. E* 79:041928.

[115] Wheeldon, I., A. Farhadi, A. G. Bick, E. Jabbari, and A. Khademhosseini. 2011. Nanoscale tissue engineering: spatial control over cell-materials interactions. *Nanotechnology* 22:212001.

[116] Doi, M. and S. F. Edwards. 1987. The Theory of Polymer Dynamics. New York: Oxford University Press.

[117] Podtelezhnikov, A. A. 2008. Kuhn length, persistence length, and bending rigidity.

[118] Broedersz, C. P., C. Storm, and F. C. MacKintosh. 2008. Nonlinear elasticity of composite networks of stiff biopolymers with flexible linkers. *Phys. Rev. Lett.* 101:118103.

[119] Wagner, B., R. Tharmann, I. Haase, M. Fischer, and A. R. Bausch. 2006. Cytoskeletal polymer networks: the molecular structure of cross-linkers determines macroscopic properties. *Proc. Natl. Acad. Sci. U.S.A.*

103:13974-13978.

[120] Janmey, P. A., S. Hvidt, J. Lamb, and T. P. Stossel. 1990. Resemblance of actin-binding protein/actin gels to covalently crosslinked networks. *Nature* 345:89-92.

[121] Gardel, M. L., J. H. Shin, F. C. MacKintosh, L. Mahadevan, P. A. Matsudaira, and D. A. Weitz. 2004. Scaling of F-actin network rheology to probe single filament elasticity and dynamics. *Phys. Rev. Lett.* 93:188102.

[122] Lieleg, O., M. M. A. E. Claessens, C. Heussinger, E. Frey, and A. R. Bausch. 2007. Mechanics of bundled semiflexible polymer networks. *Phys. Rev. Lett.* 99:088102.

[123] Gisler, T., R. C. Ball, and D. A. Weitz. 1999. Strain hardening of fractal colloidal gels. *Phys. Rev. Lett.* 82:1064-1067.

[124] Hatami-Marbini, H. and R. C. Picu. 2008. Scaling of nonaffine deformation in random semiflexible fiber networks. *Phys. Rev. E* 77:062103.

[125] Mizuno, D., C. Tardin, C. F. Schmidt, and F. C. Mackintosh. 2007. Nonequilibrium mechanics of active cytoskeletal networks. *Science* 315:370-373.

[126] Broedersz, C. P. and F. C. MacKintosh. 2011. Molecular motors stiffen non-affine semiflexible polymer networks. *Soft Matter* 7:3186-3191.

[127] Bai, M., A. R. Missel, A. J. Levine, and W. S. Klug. 2011. On the role of the filament length distribution in the mechanics of semiflexible networks. *Acta Biomater.* 7:2109-2118.

[128] Kasza, K. E., C. P. Broedersz, G. H. Koenderink, Y. C. Lin, W. Messner, E. A. Millman, F. Nakamura, T. P. Stossel, F. C. Mackintosh, and D. A. Weitz. 2010. Actin filament length tunes elasticity of flexibly cross-linked actin networks. *Biophys. J.* 99:1091-1100.

[129] Ziemann, F., J. Rädler, and E. Sackmann. 1994. Local measurements of viscoelastic moduli of entangled actin networks using an oscillating magnetic bead micro-rheometer. *Biophys. J.* 66:2210-2216.

[130] Bausch, A. R., W. Möller, and E. Sackmann. 1999. Measurement of local viscoelasticity and forces in living cells by magnetic tweezers. *Biophys. J.* 76:573-579.

[131] Pesce, G., A. C. De Luca, G. Rusciano, P. A. Netti, S. Fusco, and A. Sasso. 2009. Microrheology of complex fluids using optical tweezers: a comparison with macrorheological measurements. *J. Opt. A: Pure Appl. Opt.* 11:034016.

[132] Radmacher, M., R. W. Tillmann, and H. E. Gaub. 1993. Imaging viscoelasticity by force modulation with the atomic force microscope. *Biophys. J.* 64:735-742.

[133] Mason, T. G., K. Ganesan, J. H. van Zanten, D. Wirtz, and S. C. Kuo. 1997. Particle tracking microrheology of complex fluids. *Phys. Rev. Lett.* 79:3282-3285.

[134] Gittes, F., B. Schnurr, P. D. Olmsted, F. C. MacKintosh, and C. F. Schmidt. 1997. Microscopic viscoelasticity: Shear moduli of soft materials determined from thermal fluctuations. *Phys. Rev. Lett.* 79:3286-3289.

[135] Schnurr, B., F. Gittes, F. C. MacKintosh, and C. F. Schmidt. 1997. Determining microscopic viscoelasticity in flexible and semiflexible polymer networks from thermal fluctuations. *Macromolecules* 30:7781-7792.

[136] Mason, T. G. and D. A. Weitz. 1995. Optical measurements of frequency-dependent linear viscoelastic moduli of complex fluids. *Phys. Rev. Lett.* 74:1250-1253.

[137] Gisler, T. and D. A. Weitz. 1999. Scaling of the microrheology of semidilute F-actin solutions. *Phys. Rev. Lett.* 82:1606-1609.

[138] Mason, T. G., H. Gang, and D. A. Weitz. 1997. Diffusing-wave-spectroscopy measurements of viscoelasticity of complex fluids. *J. Opt. Soc. Am. A* 14:139-149.

[139] MacKintosh, F. C. 1999. Microrheology. *Curr. Opin. Colloid Interface Sci.* 4:300-307.

[140] Squires, T. M. and T. G. Mason. 2010. Fluid Mechanics of Microrheology. *Annual Review of Fluid Mechanics* 42:413-438.

[141] Mason, T. G. 2000. Estimating the viscoelastic moduli of complex fluids using the generalized Stokes-Einstein equation. *Rheol. Acta* 39:371-378.

[142] Crocker, J. C., M. T. Valentine, E. R. Weeks, T. Gisler, P. D. Kaplan, A. G. Yodh, and D. A. Weitz. 2000. Two-point microrheology of inhomogeneous soft materials. *Phys. Rev. Lett.* 85:888-891.

[143] Dasgupta, B. R., S.-Y. Tee, J. C. Crocker, B. J. Frisken, and D. A. Weitz. 2002. Microrheology of polyethylene oxide using diffusing wave spectroscopy and single scattering. *Phys. Rev. E* 65:051505.

[144] Dasgupta, B. R. and D. A. Weitz. 2005. Microrheology of cross-linked polyacrylamide networks. *Phys. Rev. E* 71:021504.

[145] Crocker, J. C. and D. G. Grier. 1996. Methods of digital video microscopy for colloidal studies. *J. Colloid Interface Sci.* 179:298-310.

[146] Crocker, J. C. and B. D. Hoffman. 2007. Multiple-particle tracking and two-point microrheology in cells. *Methods Cell Biol.* 83:141-178.

[147] Anthony, S. M. and S. Granick. 2009. Image analysis with rapid and accurate two-dimensional Gaussian fitting. *Langmuir* 25:8152-8160.

[148] Velegol, D. and F. Lanni. 2001. Cell traction forces on soft biomaterials. I. Microrheology of type I collagen gels. *Biophys. J.* 81:1786-1792.

[149] Valentine, M. T., P. D. Kaplan, D. Thota, J. C. Crocker, T. Gisler, R. K. Prud'homme, M. Beck, and D. A. Weitz. 2001. Investigating the microenvironments of inhomogeneous soft materials with multiple particle tracking. *Phys. Rev. E* 64:061506.

[150] Fu, H. C., V. B. Shenoy, and T. R. Powers. 2008. Role of slip between a probe particle and a gel in microrheology. *Phys. Rev. E* 78:061503.

[151] Petersen, N. O., P. L. Höddelius, P. W. Wiseman, O. Seger, and K. E. Magnusson. 1993. Quantitation of membrane receptor distributions by image correlation spectroscopy: concept and application. *Biophys. J.* 65:1135-1146.

[152] Wiseman, P. W., J. A. Squier, M. H. Ellisman, and K. R. Wilson. 2000. Two-photon image correlation spectroscopy and image cross-correlation

spectroscopy. *J. Microsc.* 200:14-25.

[153] Wiseman, P. W., C. M. Brown, D. J. Webb, B. Hebert, N. L. Johnson, J. A. Squier, M. H. Ellisman, and A. F. Horwitz. 2004. Spatial mapping of integrin interactions and dynamics during cell migration by image correlation microscopy. *J. Cell Sci.* 117:5521-5534.

[154] Hebert, B., S. Costantino, and P. W. Wiseman. 2005. Spatiotemporal image correlation spectroscopy (STICS) theory, verification, and application to protein velocity mapping in living CHO cells. *Biophys. J.* 88:3601-3614.

[155] Gielen, E., N. Smisdom, M. vandeVen, B. De Clercq, E. Gratton, M. Digman, J. M. Rigo, J. Hofkens, Y. Engelborghs, and M. Ameloot. 2009. Measuring diffusion of lipid-like probes in artificial and natural membranes by raster image correlation spectroscopy (RICS): use of a commercial laser-scanning microscope with analog detection. *Langmuir* 25:5209-5218.

[156] Kolin, D. L. and P. W. Wiseman. 2007. Advances in image correlation spectroscopy: measuring number densities, aggregation states, and dynamics of fluorescently labeled macromolecules in cells. *Cell Biochem. Biophys.* 49:141-164.

[157] Elson, E. L. and D. Magde. 1974. Fluorescence correlation spectroscopy. I. Conceptual basis and theory. *Biopolymers* 13:1-27.

[158] Wiseman, P. W. and N. O. Petersen. 1999. Image correlation spectroscopy. II. Optimization for ultrasensitive detection of preexisting platelet-derived growth factor-beta receptor oligomers on intact cells. *Biophys. J.* 76:963-977.

[159] Sheely, M. L. 1932. Glycerol viscosity tables. *Ind. Eng. Chem.* 24:1060-1064.

[160] Cooper, E. C., P. Johnson, and A. M. Donald. 1991. Probe diffusion in polymer solutions in the dilute/semi-dilute crossover regime: 1. Poly(ethylene oxide). *Polymer* 32:2815-2822.

[161] Devanand, K. and J. C. Selser. 1991. Asymptotic behavior and long-range interactions in aqueous solutions of poly(ethylene oxide). *Macromolecules* 24:5943-5947.

[162] Srivastava, M. and N. O. Petersen. 1996. Image cross-correlation spectroscopy: A new experimental biophysical approach to measurement of slow diffusion of fluorescent molecules. *Methods Cell Sci.* 14:47-54.

[163] Cicuta, P. and A. M. Donald. 2007. Microrheology: a review of the method and applications. *Soft Matter* 3:1449-1455.

[164] Tseng, Y., J. S. H. Lee, T. P. Kole, I. Jiang, and D. Wirtz. 2004. Micro-organization and visco-elasticity of the interphase nucleus revealed by particle nanotracking. *J. Cell Sci.* 117:2159-2167.

[165] Sohn, I. S. and R. Rajagopalan. 2004. Microrheology of model quasi-hard-sphere dispersions. *J. Rheol.* 48:117-142.

[166] Solomon, M. J. and Q. Lu. 2001. Rheology and dynamics of particles in viscoelastic media. *Curr. Opin. Colloid Interface Sci.* 6:430-437.

[167] Sprakel, J., J. van der Gucht, M. A. Cohen Stuart, and N. A. M. Besseling. 2008. Brownian particles in transient polymer networks. *Phys. Rev. E* 77:061502.

[168] Sohn, I. S., R. Rajagopalan, and A. C. Dogariu. 2004. Spatially resolved microrheology through a liquid/liquid interface. *J. Colloid Interface Sci.* 269:503-513.

[169] Waigh, T. A. 2005. Microrheology of complex fluids. *Rep. Prog. Phys.* 68:685-742.

[170] Valentine, M. T., Z. E. Perlman, M. L. Gardel, J. H. Shin, P. Matsudaira, T. J. Mitchison, and D. A. Weitz. 2004. Colloid surface chemistry critically affects multiple particle tracking measurements of biomaterials. *Biophys. J.* 86:4004-4014.

[171] Lu, Q. and M. J. Solomon. 2002. Probe size effects on the microrheology of associating polymer solutions. *Phys. Rev. E* 66:061504.

[172] Yamada, S., D. Wirtz, and S. C. Kuo. 2000. Mechanics of living cells measured by laser tracking microrheology. *Biophys. J.* 78:1736-1747.

[173] Jonas, M., H. Huang, R. D. Kamm, and P. T. C. So. 2008. Fast fluorescence laser tracking microrheometry. I: instrument development. *Biophys. J.* 94:1459-1469.

[174] Lieleg, O., M. M. A. E. Claessens, and A. R. Bausch. 2010. Structure and dynamics of cross-linked actin networks. *Soft Matter* 6:218-225.

[175] Bahns, J. T., C.-M. Liu, and L. Chen. 2004. Characterizing specific phage-protein interactions by fluorescence correlation spectroscopy. *Protein Sci.* 13:2578-2587.

[176] Dietrich, C., B. Yang, T. Fujiwara, A. Kusumi, and K. Jacobson. 2002. Relationship of lipid rafts to transient confinement zones detected by single particle tracking. *Biophys. J.* 82:274-284.

[177] Rathgeber, S., H.-J. Beauvisage, H. Chevreau, N. Willenbacher, and C. Oelschlaeger. 2009. Microrheology with fluorescence correlation spectroscopy. *Langmuir* 25:6368-6376.

[178] Rusu, L., A. Gambhir, S. McLaughlin, and J. Radler. 2004. Fluorescence correlation spectroscopy studies of Peptide and protein binding to phospholipid vesicles. *Biophys. J.* 87:1044-1053.

[179] Starchev, K., J. Zhang, and J. Buffle. 1998. Applications of Fluorescence Correlation Spectroscopy — Particle Size Effect. *J. Colloid Interface Sci.* 203:189-196.

[180] Wu, B., Y. Chen, and J. D. Müller. 2008. Fluorescence correlation spectroscopy of finite-sized particles. *Biophys. J.* 94:2800-2808.

[181] Press, W. H., S. A. Teukolsky, W. T. Vetterling, and B. P. Flannery. 2007. Numerical Recipes: The Art of Scientific Computing. New York: Cambridge University Press.

[182] Wachsmuth, M., W. Waldeck, and J. Langowski. 2000. Anomalous diffusion of fluorescent probes inside living cell nuclei investigated by spatially-resolved fluorescence correlation spectroscopy. *J. Mol. Biol.* 298:677-689.

[183] Koppel, D. E., F. Morgan, A. E. Cowan, and J. H. Carson. 1994. Scanning concentration correlation spectroscopy using the confocal laser microscope.

Biophys. J. 66:502-507.

[184] Petersen, N. O. 1986. Scanning fluorescence correlation spectroscopy. I. Theory and simulation of aggregation measurements. *Biophys. J.* 49:809-815.

[185] Aragón, S. R. and R. Pecora. 1976. Fluorescence correlation spectroscopy as a probe of molecular dynamics. *J. Chem. Phys.* 64:1791-1803.

[186] Fakhri, N., F. C. MacKintosh, B. Lounis, L. Cognet, and M. Pasquali. 2010. Brownian motion of stiff filaments in a crowded environment. *Science* 330:1804-1807.

[187] Koenderink, G. H., Z. Dogic, F. Nakamura, P. M. Bendix, F. C. MacKintosh, J. H. Hartwig, T. P. Stossel, and D. A. Weitz. 2009. An active biopolymer network controlled by molecular motors. *Proc. Natl. Acad. Sci. U.S.A.* 106:15192-15197.

[188] Chen, D. T. N., K. Chen, L. A. Hough, M. F. Islam, and A. G. Yodh. 2010. Rheology of carbon nanotube networks during gelation. *Macromolecules* 43:2048-2053.

[189] Verma, R., J. C. Crocker, T. C. Lubensky, and A. G. Yodh. 1998. Entropic colloidal interactions in concentrated DNA solutions. *Phys. Rev. Lett.* 81:4004-4007.

[190] Chen, D. T., E. R. Weeks, J. C. Crocker, M. F. Islam, R. Verma, J. Gruber, A. J. Levine, T. C. Lubensky, and A. G. Yodh. 2003. Rheological microscopy: local mechanical properties from microrheology. *Phys. Rev. Lett.* 90:108301.

[191] Levine, A. J. and T. C. Lubensky. 2000. One- and two-particle microrheology. *Phys. Rev. Lett.* 85:1774-1777.

[192] Chae, B. S. and E. M. Furst. 2005. Probe surface chemistry dependence and local polymer network structure in F-actin microrheology. *Langmuir* 21:3084-3089.

[193] McGrath, J. L., J. H. Hartwig, and S. C. Kuo. 2000. The mechanics of F-actin microenvironments depend on the chemistry of probing surfaces. *Biophys. J.* 79:3258-3266.

[194] Fu, H. C., V. B. Shenoy, and T. R. Powers. 2008. Role of slip between a probe particle and a gel in microrheology. *Phys. Rev. E* 78:061503.

[195] Schmiedeberg, M. and H. Stark. 2005. One-bead microrheology with rotating particles. *Europhys. Lett.* 69:629-635.

[196] Leong, W. S., C. Y. Tay, H. Yu, A. Li, S. C. Wu, D. H. Duc, C. T. Lim, and L. P. Tan. 2010. Thickness sensing of hMSCs on collagen gel directs stem cell fate. *Biochem. Biophys. Res. Commun.* 401:287-292.

[197] Buxboim, A., K. Rajagopal, A. E. X. Brown, and D. E. Discher. 2010. How deeply cells feel: methods for thin gels. *J. Phys.: Condens. Matter* 22:194116.

[198] Buxboim, A., I. L. Ivanovska, and D. E. Discher. 2010. Matrix elasticity, cytoskeletal forces and physics of the nucleus: how deeply do cells 'feel' outside and in? *J. Cell Sci.* 123:297-308.

[199] Yanai, M., J. P. Butler, T. Suzuki, H. Sasaki, and H. Higuchi. 2004. Regional rheological differences in locomoting neutrophils. *Am. J. Physiol. Cell Physiol.* 287:C603-611.

[200] Bonor, J. and A. Nohe. 2010. Image correlation spectroscopy to define membrane dynamics. *Methods Mol. Biol.* 591:353-364.

[201] Digman, M. A. and E. Gratton. 2009. Analysis of diffusion and binding in cells using the RICS approach. *Microsc. Res. Tech.* 72:323-332.

Appendix A: Steps in ICS-μR

Here, we present the details of the practical aspects and implementations in the ICS-μR analysis.[5] To help the reader with the various quantities involved in the analysis, Figure A 1 illustrates the calculation stages that will be subsequently discussed.

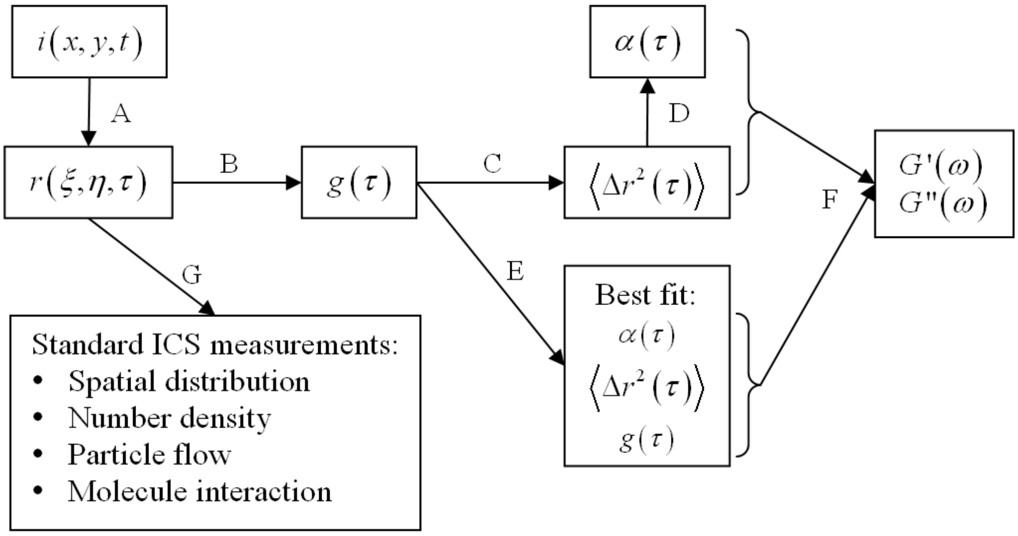

Figure A 1: A schematic overview of data analysis steps involved in ICS-μR. The steps A through F are explained in the text below. Steps A, B, and G are routinely followed in standard ICS measurements, whereas Steps D and F are routinely used in standard microrheology measurements. In the present work, we introduce Step C, which allows microrheological analysis from ICS data, as well as Step E, which improves the quality of the microrheological results extracted from the data.

---

[5] All symbols and their meanings in this Appendix are the same as those used in the main body of the thesis, and explanations of the notations are, therefore, not repeated unless necessary.

Step A

The raw data obtained in ICS is a sequence of images which represent the image intensity $i(x,y,t)$ in space (*i.e.*, x and y) and time t. The normalized intensity correlation function is calculated as a function of the spatial lag, ξ and η, as well as lag time, τ, using Eqs. (5.4) and (5.5). To minimize computation time, $r(\xi,\eta,\tau)$ is calculated using the Fourier method [162].

Step B

For each time lag τ, the spatial correlation function is taken to be a 2D Gaussian [Eq. (5.6)], as described in Section 5.2.4. This spatial fitting is typically done in the least square manner and only for the central correlation area (small ξ and η) with zero weighting for the central point (*i.e.*, $\xi=\eta=0$), where there is white noise contribution. We found that the optimum fit is obtained by including data points where ξ and η are smaller than 5–6 times the Gaussian width d_0. The output of this step is $g(\tau)$.

Step C

For 3D Gaussian intensity profile of the excitation volume, the functional form of the temporal correlation function for a system with 3D diffusion is [185]

$$g(\tau)=g_0\left(1+\frac{\tau}{\tau_{D,xy}}\right)^{-1}\left(1+\frac{d_z^2}{d_{xy}^2}\frac{\tau}{\tau_{D,z}}\right)^{-1/2}, \tag{A.1}$$

where the translational diffusion relaxation times, τ_D, in the lateral and axial directions are related to the diffusion coefficient , D , respectively, by

$\tau_{D,xy} = \omega_{xy}^2 / 4D$ and $\tau_{D,z} = \omega_z^2 / 4D$. Equation (A.1) can thus be rewritten as

$$g(\tau) = g_0 \left(1 + \frac{4D\tau}{d_{xy}^2}\right)^{-1} \left(1 + \frac{4D\tau}{d_z^2}\right)^{-1/2}. \tag{A.2}$$

If one assumes that the local effective D can be related to the MSD of the probe particles, $\left\langle \Delta r^2(\tau) \right\rangle$, by $\left\langle \Delta r^2(\tau) \right\rangle = 6D\tau$, then Eq. (A.2) becomes

$$g(\tau) = g_0 \left(1 + \frac{2\left\langle \Delta r^2(\tau) \right\rangle}{3d_{xy}^2}\right)^{-1} \left(1 + \frac{2\left\langle \Delta r^2(\tau) \right\rangle}{3d_z^2}\right)^{-1/2}. \tag{A.3}$$

Therefore, by solving (A.3), one can obtain the MSD data from the temporal correlation function.

Step D

The logarithmic derivative of $\left\langle \Delta r^2(\tau) \right\rangle$ with respect to time is calculated as in Eq. (4.5). Numerical derivation in this process typically uses Gaussian sliding window approach [143], which inherently involve smoothing of the $\left\langle \Delta r^2(\tau) \right\rangle$ data to reduce high-frequency noise in the data. This step is not needed for the method we propose (which requires only Steps E, which improves the quality of the extracted results).

Step E

One can, in principle, directly calculate $G'(\omega)$ and $G"(\omega)$ from the $\left\langle \Delta r^2(\tau) \right\rangle$ and $\alpha(\tau)$ data obtained in Steps C and D. However, the use of such an approach could lead to propagation of experimental and data processing errors arising from Step B and the Eqs. (A.3) and (4.5). In Step E here, we propose an alternative method that minimizes these errors.

Since $g(\tau)$, $\langle \Delta r^2(\tau) \rangle$, and $\alpha(\tau)$ are dependent on each other [as mathematically described in Eqs. (A.3) and (4.5)], we use an approach that eliminates the need for Eq. (4.5) and determines $\alpha(\tau)$ directly from $g(\tau)$ by choosing a robust functional form for $\alpha(\tau)$, writing $\langle \Delta r^2(\tau) \rangle$ in terms of $\alpha(\tau)$, and substituting in Eq. (A.3). We choose Eq. (5.8) to do this and determine the parameters in Eq. (5.8) by a statistical analysis of the raw $g(\tau)$ data (from Step B). The functional form in Eq. (5.8) has the advantage of being able to describe asymptotic power laws and the transitions, which are prevalent in many viscoelastic materials, as stated in Section 5.3.1.

Step F

The $\langle \Delta r^2(\tau) \rangle$ and $\alpha(\tau)$ data obtained from Step E can then be used to calculate the frequency-dependent storage modulus, $G'(\omega)$, and loss modulus, $G''(\omega)$, using Eqs. (4.6) and (4.7).

Step G

In addition to the microrheological information obtained in the previous steps, a number of 'standard' ICS measurements can also be obtained from the spatiotemporal correlation function $r(\xi,\eta,\tau)$. The methods to obtain this information can be found in the ICS literature, which has been extensively reviewed by Kolin and Wiseman [156].

Illustrations

To illustrate the usefulness of Step E, we show one typical extracted result based on this procedure and compare it to the result obtained from a combination of Steps C and D, for the raw $g(\tau)$ data (Fig. S2), the $\langle \Delta r^2(\tau) \rangle$ data (Fig. S3), as well as the $G'(\omega)$ and $G''(\omega)$ data (Fig. S4).

Finally, we compare the ICS-μR results for complex, viscoelastic materials (PEO solutions of different concentrations) with results obtained using mechanical rheology in Fig. S5. Note that as the material becomes increasingly liquid-like at low frequency, both the magnitude and quality of the G' data decrease rapidly. For that reason and because of the logarithmic scale used in the *y*-axis, the error bar grows in size and the deviation between the results from the two methods may mistakenly seem to grow.

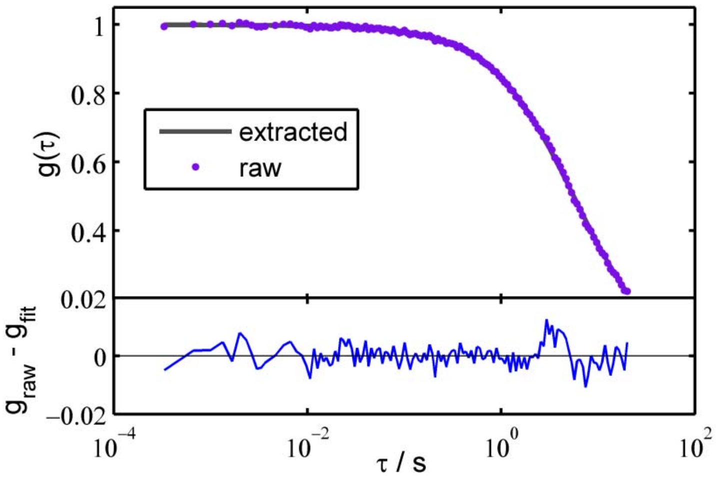

Figure A 2: Comparison between the raw, unsmoothed $g(\tau)$ data obtained from Step B and the extracted $g(\tau)$ data obtained from Step E. The bottom panel shows the difference between the two data sets.

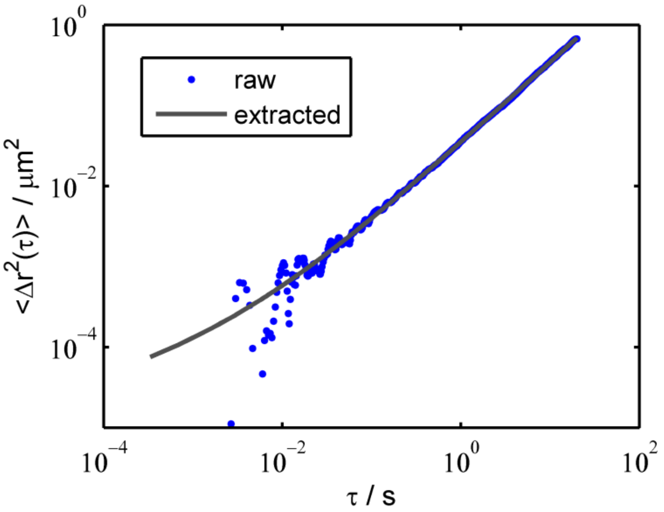

Figure A 3: Comparison between the $\langle \Delta r^2(\tau) \rangle$ data obtained from Step C and the extracted $\langle \Delta r^2(\tau) \rangle$ data obtained from Step E. Note the data truncation in the raw data at small τ due to amplified carry-over noise from the raw $g(\tau)$ data in Step B.

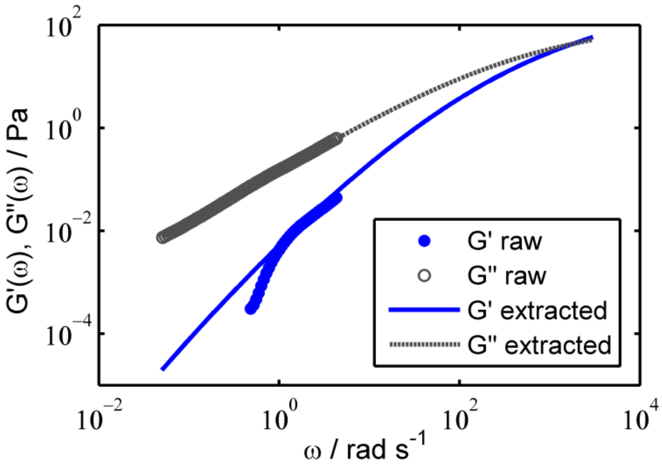

Figure A 4: Comparison between the ‘raw’ $G'(\omega)$ and $G''(\omega)$ data obtained from Steps C, D, and F and the extracted $G'(\omega)$ and $G''(\omega)$ data obtained from Steps E and F. The noise in the raw $g(\tau)$ data (Figure A 2) is doubly amplified through calculation of $\langle \Delta r^2(\tau) \rangle$ in Step C (Figure A 3) and $\alpha(\tau)$ in Step D, forcing severe data truncations in the ‘raw’ $G'(\omega)$ and $G''(\omega)$ data.

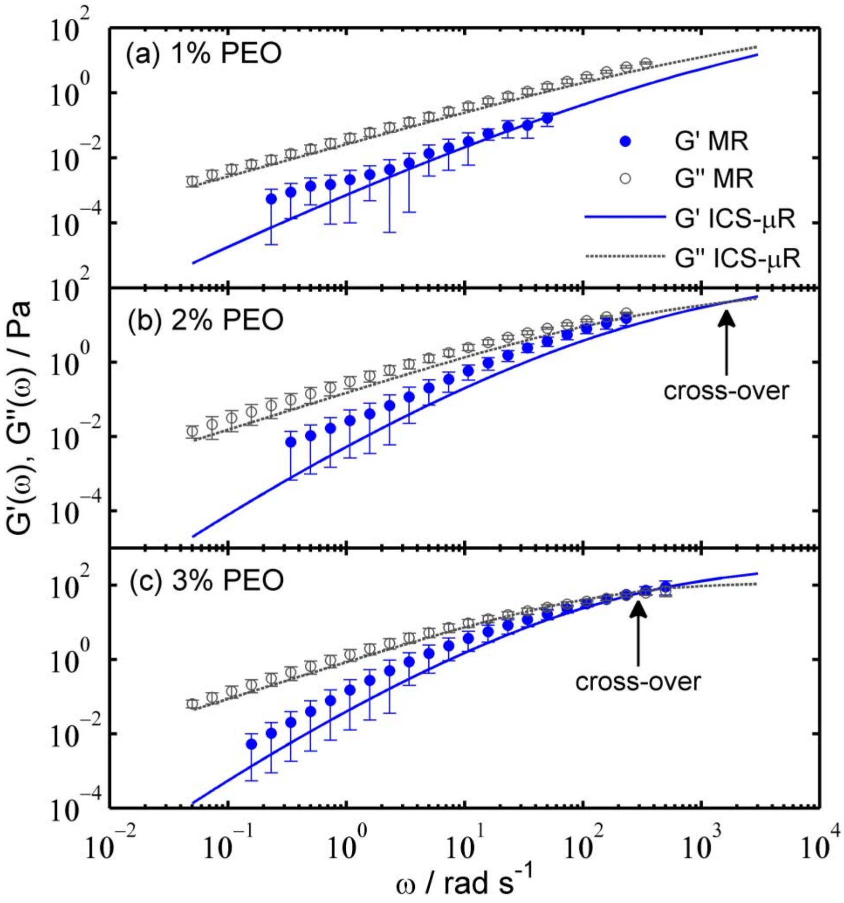

Figure A 5: Comparison between frequency-dependent linear viscoelastic moduli for PEO aqueous solutions of various concentrations as measured with ICS-μR and mechanical rheometer (MR). ICS-μR results were obtained from $\left\langle \Delta r^2\left(\tau\right)\right\rangle$ of 0.5 μm beads in the solutions. The error bars signify the extent of experimental error in the mechanical rheology measurement.